August 1994 • NREL/TP-413-7061

The Role of Point Defects and Defect Complexes in Silicon Device Processing

Summary Report and Papers

Workshop Chairman: B.L. Sopori
Third Workshop
Vail, Colorado
August 16–18, 1993

Prepared by: B. Sopori and T.Y. Tan
with contributions from Session Chairmen

National Renewable Energy Laboratory
1617 Cole Boulevard
Golden, Colorado 80401-3393
A national laboratory of the U.S. Department of Energy
Managed by Midwest Research Institute
for the U.S. Department of Energy
under contract No. DE-AC36-83CH10093

NREL/TP-413-7061 • UC Category: 1263 • DE94011873

The Role of Point Defects and Defect Complexes in Silicon Device Processing

Summary Report and Papers

Workshop Chairman: B.L. Sopori
Third Workshop
Vail, Colorado
August 16–18, 1993

Prepared by: B. Sopori and T.Y. Tan
with contributions from Session Chairmen

National Renewable Energy Laboratory
1617 Cole Boulevard
Golden, Colorado 80401-3393
A national laboratory of the U.S. Department of Energy
Managed by Midwest Research Institute
for the U.S. Department of Energy
under contract No. DE-AC36-83CH10093

Prepared under Task No. PV421101

August 1994

NOTICE

This report was prepared as an account of work sponsored by an agency of the United States government. Neither the United States government nor any agency thereof, nor any of their employees, makes any warranty, express or implied, or assumes any legal liability or responsibility for the accuracy, completeness, or usefulness of any information, apparatus, product, or process disclosed, or represents that its use would not infringe privately owned rights. Reference herein to any specific commercial product, process, or service by trade name, trademark, manufacturer, or otherwise does not necessarily constitute or imply its endorsement, recommendation, or favoring by the United States government or any agency thereof. The views and opinions of authors expressed herein do not necessarily state or reflect those of the United States government or any agency thereof.

Third Workshop
Role of Point Defects/Defect Complexes
in Silicon Device Processing

Contents

Page

WORKSHOP OVERVIEW 1-7

Papers Received:

RECENT RESULTS ON EFFECTS OF TRANSITION METALS AND HYDROGEN IN EFG POLYCRYSTALLINE SILICON
Juris Kalejs 9

IMPURITY/DEFECT ANALYSIS OF HEM SILICON
Chandra Khattak, F. Schmid, M. Cudzinovic and B. L. Sopori 13

ELECTRICAL BEHAVIOR OF DISLOCATIONS AND IMPURITIES IN SILICON
George Rozgonyi, A. Agarwal, N. Braga, H. Kikuchi, S. Koveshnikov 19

CHARACTERIZATION OF CARBON IN EFG USING THE G-CENTER
Bill Sawyer, Gordon Davies, Seung-Chul Park and Victor Higgs 33

DIFFUSION - SEGREGATION EQUATION FOR SIMULATION IN HETEROSTRUCTURES
Teh Tan, R. Gafiteanu, H. M. You, and U. Gosele 35

MODIFICATIONS TO THE SOLAREX CASTING PROCESS: EFFECTS ON DEFECT IMPURITIES, AND SOLAR CELL PERFORMANCE
Mohan Narayanan, and T. Tomlinson 51

THE EFFECT OF RESISTIVITY ON THE MINORITY CARRIER LIFETIME OF CHROMIUM DOPED P-TYPE SILICON
Kamal Mishra 57

THE STRUCTURAL, CHEMICAL, AND ELECTRICAL PROPERTIES OF HE-IMPLANTATION-INDUCED NANOCAVITIES IN SILICON
Carl Seager, S. M. Myers, D. M. Follstaedt, H. J. Stein and W. R. Wampler 65

EFFECTS OF ALUMINUM GETTERING AND FORMING GAS ANNEAL ON MULTICRYSTALLINE SILICON SOLAR CELLS
Ajeet Rohatgi, P. Sana, M. S. Ramanachalam, W. B. Carter, J. P. Kalejs and R. O. Bell 85

HYDROGEN DIFFUSION AND PASSIVATION MECHANISMS
Stefan Estreicher 99

STATUS AND FABRICATION OF HIGH-EFFICIENCY SINGLE-CRYSTAL SI SOLAR CELLS
R. A. Sinton 107

WORKSHOP OVERVIEW

During the previous two workshops, we addressed many issues related to defects and impurities in commercial solar cell substrates. One of the recommendations from the discussion groups was that cell fabrication by processes involving gettering and defect passivation would help improve material quality. Indeed, these predictions have proven to be correct. It is now well established that gettering by phosphorus diffusions, TCA, and HCl treatments can be successfully applied to improve minority carrier lifetime and cell performance. Likewise, hydrogen passivation is expected to play an important role in the fabrication of high efficiency (16%-18%) commercial solar cells. As these advanced techniques are being incorporated into cell fabrication steps, we are uncovering new issues that remain to be resolved. At the National Renewable Energy Laboratory (NREL), and several other laboratories working under the DOE/NREL subcontract program, research on the loss mechanisms in polycrystalline solar cells has led to the finding that nonuniformities can severly limit the performance of commercial solar cells. In view of these findings, we have selected nonuniformities as the theme of this workshop.

Material inhomogeneities arise from defects, impurity segregation, and residual stresses. The nonuniformities arising from these sources are further altered by solar cell processing steps. Research performed during the past year has established that certain regions of a substrate improve significantly more than others by processes such as gettering and H passivation. It is apparent that such regions are heavily dominated by defects.

This workshop is organized (1) to discuss recent progress in the material quality produced by photovoltaic Si manufacturers, (2) to foster the understanding of point defect issues in Si device processing, (3) to review the effects of inhomogeneities on large-area solar cell performance, (4) to discuss how to improve Si solar cell processing, and (5) to develop a new understanding of gettering, defect passivation, and defect annihilation. Sessions and panel discussions are organized to provide a forum for a convenient exchange of information related to these issues.

PANEL DISCUSSION 1

IMPURITIES AND DEFECTS IN PHOTOVOLTAIC SILICON

Panelists: Lubek Jastrzebski, Fritz Wald, Ted Ciszek

This session addressed the definition of PV silicon from the point of view of impurities and defects in this material. However, it was clear that there are large variations in the concentrations of impurities and defects in the materials from various vendors that do not allow a clear identification of "solar cell silicon." The research results presented at this workshop showed that Fe and Cr were dominant impurities. These impurities were typically present in the range of 10^{11} - 10^{12} cm^{-3}. Other impurities such as Ti and V were also identified in EFG Si. Defect analyses showed dislocations to be the dominant intragrain defect in polycrystalline substrates. Similarly, in the single crystal CZ solar cell substrates used by Siemens Solar, the "lost structure" consisted of slip dislocations. Panelists also noted that polycrystalline Si substrates also exhibit a high degree of twinning, typically covering about 20% of the total substrate area. Of major significance are the regions containing high dislocation densities, $>10^6$ cm^{-2}. It was established that gettering efficiency in these regions is quite low; concomitantly, these regions do not show a significant increase in the minority carrier lifetime upon gettering. Likewise, the photo response of a highly defective region does not exhibit any improvement due to gettering.

The results of two models (the NREL model developed by Sopori and the Holland model used by Mobil Solar) for non-uniform cells were presented. Both models predict a severe degradation in the cell performance due to the presence of low-efficiency regions.

The issues of concern were:

- Do regions of high dislocation density contain precipitated impurities that cannot be detected in an SPV-type of measurement for detection of Fe and Cr? An opinion was expressed that degradation arises from dangling bonds.

- The modeling results, showing that low efficiency regions can have disproportionately large effects on cell degradation, implies a need to identify the mechanisms responsible for these "bad" regions of the substrates. Clearly, it is important to determine how such regions can be improved.

- The need for a quick, effective way to evaluate an ingot before wafering.

- A need for systematic studies to establish mechanisms of cell degradation due to defects and impurities. Although some information pertaining to the effects of dislocations and grain boundaries on the dark and illuminated cell characteristics is already available from previous work, it may be beneficial to perform analyses in controlled materials. Such materials may be grown by FZ technique with controlled defects and impurities as variables.

- Each of the industry participants expressed a need to perform characterization of as-grown substrates as well as identify the nature of improvements due to various advanced cell fabrication processes. A commercially compatible technique/equipment for such characterization is being sought.

- The panelists felt that there were some merits for organizing the workshop along growth methods rather than discussing all of them together.

PANEL DISCUSSION 2

IMPURITY GETTERING IN SILICON

Panelists: Teh Tan, Eicke Weber, George Rozgonyi

In a similar panel discussion session held in 1992 at the Second Workshop on the Role of Point Defects, it was pointed out that gettering for Si solar cells must meet many demands that are not required in IC processing. These include:

1. The entire wafer thickness must be gettered.

2. The process must be suitable for substrates of different qualities.

3. The process must be compatible with solar cell fabrication facilities that are not "clean."

In this meeting a consensus was reached that:

1. It is preferable to perform gettering during solar cell processing rather than just after wafer fabrication.

2. Extrinsic gettering schemes are preferred, e.g., P, Al, and Cl gettering.

3. Further studies of gettering mechanisms are needed.

4. The effectiveness of gettering can be enhanced if thermal stresses and metallic impurity incorporation could be minimized during the crystal growth.

Work performed at the University of South Florida (Jastrzebski) and at NREL (Sopori) showed that the minority carrier lifetime in polycrystalline solar Si can be improved by Cl and P gettering in those grains (or regions) that possess relatively long as-grown lifetimes. The regions with very short as-grown lifetimes do not improve, and in some cases, even exhibit a degradation in lifetime. These latter phenomena are not understood. Work performed at the Georgia Institute of Technology (Rohatgi) showed that the efficiency of solar cells, fabricated on polysilicon substrates can be improved by a backside Al drive-in process at 1000°C. Forming gas annealing used after Al gettering improves the solar cell efficiency further.

Within the general consensus, the panel members believe that the time is right to begin addressing impurity gettering mechanisms, including quantitative modeling and measurement.

For quantitative modeling purposes, the gettering efficiency is suggested (Tan) to be defined as:
$h(\text{method, species}, T, t, x) = C_b/C_a$,

where "method" refers to the gettering method, e.g. Al, P, Cl, etc.; "species" is the impurity species to be gettered; "T" is gettering temperature; "t" is gettering time; "x" is the thickness of the gettered region; "C_b" is the impurity concentration before gettering; and "C_a" is the impurity concentration after gettering.

For dispersed impurity atoms, the gettering process involves the diffusion of the species to the gettering site where it is captured. However, when existing in precipitated form, impurity atoms must be first dissolved before diffusion to the gettering site can occur. The impurity diffusion-capturing process can be calculated using the diffusion-segregation equation (Tan) upon knowing the diffusing species and the nature of the gettering sites (e.g., molten Al, solid Al, HCl, etc.). For precipitated impurity species, the gettered region impurity concentration is determined by the dissolution process, which may or may not be limited by the existence of an actual or effective kinetic barrier. The latter could be due to point defect under- or super-saturation induced by the precipitate dissolution process itself. Gettering experiments and measurements should go hand-in-hand with quantitative modeling, e.g., the work on Fe conducted at Berkeley (Weber).

Further issues that arose in this discussion include

1. The possibility of producing Al pipe diffusion by a high-temperature Al drive-in to produce p+ regions surrounding the dislocation core.

2. The use of porous Si and/or deposited polycrystalline Si-Ge alloy as gettering sites.

3. The possibility of performing internal gettering followed by passivation of the gettering sites. This possibility has been brought up previously but suffered a cold reception.

4. The possibility of using other "exotic" gettering schemes such as backside damage due to He implantation.

PANEL DISCUSSION 3

DEFECT ANNIHILATION AND PASSIVATION

Panelists: Dieter Ast and Stefan Estreicher

The lead-in presentations by the panelists and the subsequent discussions addressed the following two subjects:

1. Interaction of intrinsic point defects with extended defects (Ast).

2. Hydrogen diffusion and passivation mechanisms (Estreicher).

There exist two convenient techniques for injecting Si self-interstitials into Si: oxidation and P diffusion. The point defect supersaturation due to the injection process can be determined by monitoring the interaction of point defects with extended defects. These monitoring techniques include measuring the pitch and diameter of helical dislocations and growth/shrinkage rate of the stacking faults. High temperature oxidation (1050°C or higher) produces fairly low Si self-interstitial supersaturations, typically about 2. The use of HCl, TCE, or TCA in the oxidizing ambients leads to a vacancy injection in addition to Si self-interstitial injection. Low temperature P indiffusion (900°C or lower) produces high Si self-interstitial supersaturations, typically about 100.

Muonium measurements suggest that the most stable H/m state at low temperatures is the neutral, paramagnetic one. This contradicts the negative-U model of van de Walle and Chadi. It is believed that the temperature dependence of various H configurations is as follows: at low temperatures, all H species are neutral and the H^T (tetragonal site) fraction is mobile, with an activation energy E_a=0.5eV. The H^* (the bond-center) fraction is not mobile. At high temperature, H^* converts to H^T in p-type and intrinsic Si. In n-type Si, H^* converts to H^-. More is beginning to be understood about multiple H defects, such as H_2^*, which is mobile. In p-type Si, H^T attaches to B^- and hinders the formation of H_2^*. Other possibilities include $(H\text{-}V)^o$ and $(H\text{-}V)^+$, which are also mobile. The formation and mobility of (H-I) is not known. The passivation effect of a defect by H results from forming (H+x), which moves the x gap levels to either the conduction or valance band, or changes the (complex) charge state so that there is no more electrical activity. Usually the H passivation effect goes away above 150°C because the (H+x) binding energy is not large. An example is that B is not passivated at 350°C. H-passivated dangling bonds of dislocations cannot be seen by EBIC at room temperature but can be seen at low temperatures, e.g., 80K, because of incomplete passivation.

The possibility of F and O passivation was also brought up.

PANEL DISCUSSION 4

WHAT'S NEW FOR SOLAR CELL PROCESSING

Panelists: Ron Sinton, Mohan Narayanan, Doug Ruby, Xuanzhi Wu, Henry Yoo

As lead-in presentations, the panelists discussed the following subjects:

1. The status of very high efficiency solar cells and their fabrication processes (Sinton).

2. Polysilicon cells in commercial production (Narayanan).

3. Simplified process for concentrator 23% cells (Ruby).

4. Al process (Wu).

5. Industry concerns (Yoo).

One-sun solar cells fabricated on FZ Si reached an efficiency (h) of ~23%. Twenty to twenty-one percent efficient 1-sun cells are now commercially available. This kind of h was attained in 1988 for concentrator cells. Since that time the efforts have been focused on developing 1-sun cells. The concentrator cells fabricated on FZ material have reached 29% efficiency and appear to be limited by Auger recombination.

Processing techniques vary from vendor to vendor. The doping processes used for cell fabrication include the use of CVD P-doped oxide, B-doped oxide, $POCl_3$, BBr_3, solid-source P, Al, and/or p-type wafers. Other methods include ion implantation, spin-on dopants, P gaseous diffusion, and diborane diffusion, etc. Dry O_2 thermal oxidation up to 1120°C in TCA-cleaned furnace is used. Metallization schemes include the use of evaporated Ti-Pd-Ag/plated-Ag, sputtered Al, evaporated Al, plated Ni-Cu, Ni-Ag, Ni-Au alloys, etc. Texturing is achieved using etchants NaOH, KOH, HNO_3: HF, HNO_3: NH_4F, etc. Forming gas anneals are used to passivate surface states. Other techniques include laser grooving, laser texturing, saw grooving, and rapid thermal processing (RTP). Twenty percent concentrator cells are commercially available at about $1,000/W (module).

Fourteen percent cells built on polysilicon are commercially available from Solarex. A typical fabrication sequence consists of saw damage removal/texturing, P diffusion, edge junction isolation, and AR coating and formation of the front and the back contacts. The efficiency improvement steps used include both better cell design and processing aspects. For device design, the emitter decoupling scheme is used. For processing, surface passivation (thermal and/or CVD SiO_2) and H_2 passivation are used. The contact is plated Ni-Cu. The challenge lies in volume production. The laboratory efficiencies are in the 15%-17% range and the commercial goal is to reach an efficiency >15% with a cost goal of 7.5¢/cm^2 for module and <3¢/cm^2 for cells.

Sandia has simplified the University of New South Wells PERL cell design/process to fabricate 23% concentrator cells using CZ Si. It was thought that the PERL cell is a best design. To make it more cost effective, high temperature heat treatment steps involving temperatures above 850°C are reduced to only 1. The key factor is a single emitter diffusion (the cell has no n^{++} region). Wafer texturing is accomplished in the same mask step as the emitter diffusion, and the emitter is passivated by SiO_2. Such a process requires a total of three masks.

An industrial concern is expressed in terms of normalized relative costs between terrestrial process (1-sun) and space process (concentrator). The terrestrial cell h is 13%-14% while that of the space cell is 17-1%, a difference of dh = 4%. Comparing terrestrial cells to space cells, the wafer cost ratio is 2:2, the cell fabrication cost ratio is 2:50, while the module cost ratio is 2:2. Thus, new fabrication processes are needed for space or concentrator cells. In general, fewer and simpler fabrication steps are preferably for automation.

Full wafer backside Al-Si diffusion leads to the loss of back surface reflectance and hence a decrease in h. A more recent process for Al-Si alloying developed by NREL (Sopori) produces high back-surface reflectance with an extremely low contact resistivity.

It has been found at Clemson (Singh) that rapid thermal processing (RTP) allows the temperature for drive-in diffusions to be increased and time to be decreased, resulting in no deterioration of the Si bulk lifetime of 1 ms; this experiment was being carried out in a non-cleanroom environment. This is due to photonic effects that have been fairly well revealed in studies associated with IC fabrications. Thus, the use of RTP seems to be a new processing direction. However, RTP is a single-wafer scheme, in contrast to conventional furnace annealing; which is a multiwafer batch processing scheme. This means that RTP lacks throughput, leading to increased cell fabrication cost. While increased wafer size can compensate for the low RTP throughput, large-sized processing equipment with acceptable wafer temperature uniformity may be costly to develop and manufacture. This cost may, however, be offset due to efforts in computer industry for developing flat panel displays.

NREL's von Roedern brought the Japanese success in fabricating 18%-19% a-Si/C-Si cells to the attention of the group. These cells are fabricated on n-type CZ substrate by depositing a p-type a-Si emitter, with or without an intrinsic a-Si intervening layer. Because a-Si is highly "defective" with very low lifetimes, von Roedern challenged the group to think about the validity of applying SRH recombination lifetime (bulk) concept in this case.

PANEL DISCUSSION 5

WRAP-UP/FUTURE DIRECTIONS

Panelist: Bhushan Sopori

The wrap-up discussion focused on the main solar cell efficiency limiting wafer regions and possible ways of remedying them. These regions appear to suffer from the existence of high stress and high defect densities, e.g., dislocation networks and possible metal and other impurity precipitates. P and Cl gettering appeared to be unable to improve the material lifetimes in these regions. Application of RTP/optical processing prior to gettering may be helpful in dissolving point defect clusters and precipitates, causing dislocations and point defects to annihilate and reconstruct, and relieving grown-in stresses. It may also be possible to use dislocations and grain boundaries as internal gettering sites, which may subsequently be passivated by H, O, or Al, for example. The role of O is to form insulating SiO_2 around the dislocation core, that of Al is to form a p+ region around the dislocation core, and that of H is the conventional (H+x) bound passivation type. It appears that the limit of H passivation needs to be examined and the possibility of using F and O for passivating needs to be seriously considered.

The group discussed the time and organization of the next workshop. It appears that June 1994, prior to the Gordon Conference (June 22), might be the best time. It was suggested that perhaps the workshop session should begin on Sunday, as the majority of attendees will arrive on Saturday. Objections to this arrangement exist because of company/government overtime and travel on working time considerations. However, consensus has been reached on the presentation/discussion session arrangements as well as the session times. The following suggestions have been made:

1. Add poster sessions.

2. That the presentation and panel discussion on the same subjects should be one session containing two parts with the first being the presentation and the second being the panel discussion.

3. Replace part or a whole afternoon with evening sessions from 8:00-10:00 pm session.

There was also an additional suggestion to organize the sessions in accordance with the different solar cell substrates, which is probably not a workable idea.

RECENT RESULTS ON EFFECTS OF TRANSITION METALS AND HYDROGEN IN EFG POLYCRYSTALLINE SILICON

J. P. KALEJS
Mobil Solar Energy Corporation
4 Suburban Park Drive, Billerica, MA 01821

ABSTRACT

The limits placed by transition metals on EFG polycrystalline silicon bulk lifetime are reviewed. While primary recombination activity from Ti, V and Mo arises from isolated sites, there is evidence that Fe and Cr form pairs with boron to produce additional lifetime limiting recombination centers. Concentrations of the transition metals obtained from DLTS measurements are related to diffusion length for EFG silicon. The available evidence suggests that hydrogen passivation does not restore the bulk lifetime in the presence of transition metal recombination centers.

INTRODUCTION

A number of transition metals have been found to produce recombination centers in polycrystalline silicon grown by the Edge-defined Film-fed Growth (EFG) technique that place similar limits on recombination activity to those formed in single crystal silicon [1-4]. Ti, V, and Mo, because they diffuse slowly in the host silicon, are not gettered during the usual solar cell processing steps. Faster diffusing species Fe and Cr may be gettered under appropriate processing conditions. However, gettering in polycrystalline silicon is not uniform because it is influenced by the presence of extended defects and by trapping by boron to form FeB and CrB pairs. We discuss here the results of studies of the relationship between these transition metal concentrations and bulk lifetime which establish concentration limits to recombination expected for these impurities in polycrystalline silicon.

EXPERIMENTAL RESULTS

Solar cell data on EFG silicon obtained on material grown from the melt deliberately contaminated with a number of transition metals is given in Table 1. Limits on bulk minority carrier diffusion length deduced from this data [3] are summarized in Fig. 1 as dashed lines. The data points and solid lines indicate measured limits provided from a study of FeB and Fe recombination in single crystal silicon [5].

DISCUSSION

The solar cells reported in Table 1 were processed using standard lifetime upgrading techniques, including hydrogen passivation, that we have reported previously [6]. It is evident that the upgrading has failed and that the bulk lifetime is limited by the transition metal impurity that has been deliberately added to the melt during growth. This assumption allows determination of the relation of the concentration [X] measured by DLTS in each case to the lifetime from the measured bulk diffusion length measured in the solar cell, as given in the last column in Table 1. The dashed lines labeled V, Ti and Mo in Fig. 1 are derived from this correspondence and the DLTS and solar cell data in Ref. [3]. Ti an V produce more degradation than Mo. If diffusion lengths of over 200 microns are desired after processing, then Ti and V concentrations must be reduced to below about $5x10^{11}/cm^3$, while Mo concentrations can be an order of magnitude higher.

Diffusion length limitations from Fe and Cr are more difficult to establish for several reasons. They are faster diffusers than Ti, V, or Mo, and so may be gettered to surfaces or internal defects. In addition, CrB and FeB are the favored species to be in solution at equilibrium near room temperature. Cr and Fe have been detected in EFG silicon, both in as-grown material and after phosphorus diffusion, in concentrations up to the mid-$10^{12}/cm^3$ range by DLTS [4,7]. To obtain the FeB concentration at which diffusion length limitations from FeB are comparable to those from the above slow diffusers, Fig. 1 displays the data on FeB (L_o) and on interstitial iron (L_1) recombination from Ref. [5]. If diffusion lengths of 200 microns are desired, FeB concentration must be kept below about $5x10^{12}/cm^3$.

I wish to acknowledge the contributions of my colleagues R. Bell, B. Bathey, J. Borenstein and R. Stromont to this work.

REFERENCES

[1] J. Borenstein, B.R. Bathey, J.P. Kalejs, J.I. Hanoka and N.O. Pierce, 22nd IEEE Photovolt. Spec. Conf., Las Vegas, NE (New York, 1991) p. 1006.

[2] J. Borenstein, J.I. Hanoka, B.R. Bathey, J.P. Kalejs and S. Mil'shtein, Appl. Phys. Lett. 62, 1615(1993).

[3] J.P. Kalejs, B.R. Bathey, J.T. Borenstein and R.W. Stormont, 23rd IEEE Photovolt. Spec. Conf., Louisville, KY (IEEE, New York) in press.

[4] J.P. Kalejs, L. Jastrzebski, J. Lagowski, W. Henley, D. Schielein, S. Balster and D.K. Schroder, manuscript in preparation.

[5] G. Zoth and W. Bergholtz, J. Appl. Phys. 67, 1152(1990).

[6] B.R. Bathey, R.O. Bell, J.P. Kalejs, M. Prince, M.D. Rosenblum and F.V. Wald, Proc. 11th E. C. Photovolt. Solar Energy Conf., Montreux (Harwood, Chur, 1993) p. 462.

[7] S.H. Park, D.K. Schroder and J.P. Kalejs. 22nd IEEE Photovolt. Spec. Conf., Las Vegas, NE (IEEE, New York, 1991) p. 864.

TABLE 1: SOLAR CELL PARAMETERS OF OCTAGONS DELIBERATELY DOPED WITH IMPURITIES

IMPURITY	INT.OXYGEN (atoms/cc)	RES. (ohm.cm)	VOC (volt)	ISC (ma/cm^2)	FF	PP (mW/cm^2)	NORMALIZED EFFICIENCY	MEAN IRPC L (μm)
Titanium	< 1 E16	3.0	.534	19.86	.748	7.94	0.65	12
Vanadium	< 1 E16	3.0	.530	21.95	.745	8.68	0.65	10
	5 E16	3.0	.534	22.80	.740	9.00		
	< 1 E16	0.8	.552	19.20	.715	7.58		
	5 E16	0.8	.554	20.35	.716	8.07		
Molybdenum	< 1 E16	3.0	.554	27.05	.759	11.40	0.85	80
Chromium	< 1 E16	3.0	.570	26.85	.741	11.34	0.90	95
	5 E16	3.0	.575	27.91	.744	11.91		
	< 1 E16	0.7	.584	24.38	.728	10.37		
	5 E16	0.7	.590	25.18	.718	10.67		

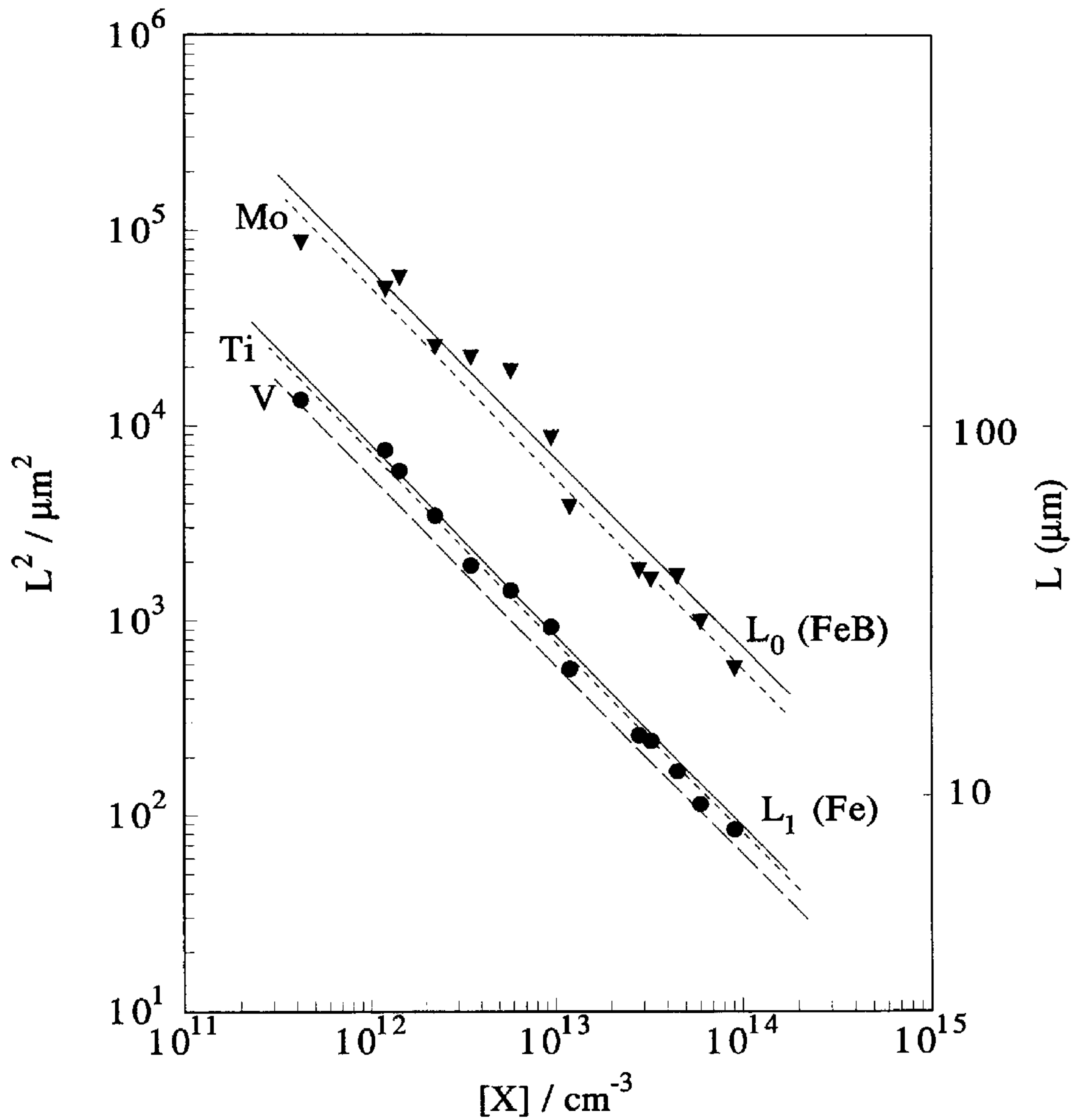

Figure 1. Relationships between the concentration [X] and the minority carrier diffusion length [L] for various transition metal impurities. Solid lines and data points are from Ref. [5] and dashed lines are from Ref. [3].

Impurity/Defect Analysis of HEM Silicon

C. P. Khattak and F. Schmid
Crystal Systems, Inc.
27 Congress Street
Salem, MA 01970 USA

M. Cudzinovic and B. L. Sopori
National Renewable Energy Laboratory
1617 Cole Boulevard
Golden, CO 80401-3393 USA

ABSTRACT

Multicrystalline silicon ingots up to 44 cm square cross-section 100 kg have been directionally solidified by the Heat Exchanger Method (HEM). Impurity/defect analysis of HEM silicon has been carried out to optimize different processing parameters, e.g., type of crucible, *in situ* annealing, etc. Results have shown that high performance solar cells can be fabricated from HEM silicon. However, the uniformity can be improved by minimizing defects in localized areas of the wafers.

Introduction

The Heat Exchanger Method (HEM) has been specifically adapted for the production of large square cross-section silicon ingots for photovoltaic applications.[1-3] Silicon ingots of 44 cm square cross-section up to 100 kg have been produced.[4,5] The emphasis during scale up to larger size ingots has been to produce high quality silicon with uniform properties throughout the ingot. The HEM is a single-crystal growth process[6,7]; the transition to multicrystalline ingot growth was made to achieve higher growth rates while retaining the directional solidification control features of single-crystal growth. This transition was made after it was established that the solar cell performance of HEM single crystal and multicrystalline silicon was similar.[8] Production of large grain size and vertical orientation of grain boundaries was emphasized during the adaptation of HEM for multicrystalline silicon ingot growth. It is recognized in the industry that high performance solar cells can be fabricated from multicrystalline HEM silicon.[9,10]

So far high purity silica crucibles were utilized for directional solidification of silicon ingots by HEM. Characterization of silicon for photovoltaic applications has shown that the central region of the ingot showed higher performance compared to the silicon near the top and the bottom of the ingot.[10,11] It is also recognized that the effect of residual impurities/defects in HEM silicon must be minimized to produce higher efficiency solar cells. This paper discusses the solar cell properties of HEM silicon produced using conventional silica crucibles as well as reusable crucibles.

Ingot Growth

In the standard HEM ingot growth, directional solidification from molten silicon in a high-purity silica crucible is carried out from the bottom of the crucible to the top surface with a slightly convex solid-liquid interface. Heat is extracted uniformly from the entire bottom of the crucible with the heat exchanger system so that nearly vertical orientation of grain boundaries is achieved.[4,5] With a square crucible and controlled directional solidification, the last material to solidify is in the top corners.

In the conventional HEM cycle a high-purity silica crucible was used. This crucible was heat treated so that it delaminated during cooldown after directional solidification. The pressure in the furnace chamber during directional solidification was approximately 0.1 torr. During HEM processing it is possible to carry out *in situ* annealing of the silicon ingot after directional solidification. This is achieved by reducing the furnace temperature below the melting point of silicon and reducing the temperature gradient with the heat exchanger system. Two 33 cm square cross-section ingots weighing 45 kg were directionally solidified by HEM. Ingot #217K was processed by the standard HEM cycle whereas ingot #222K was *in situ* annealed prior to cooldown. The effect of *in situ* annealing on the characteristics of HEM silicon was evaluated by comparing the material from these two ingots.

A reusable crucible has been developed for directional solidification of HEM silicon[12]. Detailed characterization was carried out on two ingots solidified in ceramic, non-oxide, reusable crucibles obtained from two different sources. These ingots, #239K and #251K, were 22 cm square cross-section, 11kg. Solar cells fabricated from these ingots have shown[12] solar cell efficiencies of up to 15%. Different areas of these ingots were characterized for non-metallic impurities and defects to determine if uniform defect concentration was achieved throughout the ingot.

Characterization
Silicon from Silica Crucibles

Approximately 10 cm x 10 cm wafers from ingot #217K and #222K corresponding to the bottom, middle and top positions in the ingots were characterized by Fourier Transform Infrared (FTIR) spectroscopy for carbon and oxygen concentration and the data is shown in Table I, along with diffusion length measurements using SPV. No significant difference is shown between the carbon and oxygen concentrations from these two ingots or for different positions within the ingot. The diffusion length data shows that there is essentially no difference for ingot #217K for the three positions within this ingot. By comparison, for ingot #222K the diffusion length for the top section of the ingot is lower. After $POCl_3$ diffusion and oxidation at 900°C PCD illuminated lifetime showed that highest values were obtained from the middle sections of these two ingots.[11]

Since the top and bottom sections of silicon from ingot #222K showed lower PCD lifetimes, these samples were mapped for defect density using the Rapid Scanning Defect Mapping System at NREL. This data is shown in Figure 1. Defect maps show a low "background" defect density ($\sim 10^4 cm^{-2}$) corresponding essentially to dislocation-free material. The defect density increased; however only slightly in localized areas.

Silica from Reusable Crucible

Samples from ingot #239K and #251K were also characterized for carbon and oxygen concentrations and for diffusion length measurements. The data is shown in Table II. It can be seen that there is no systematic variation in carbon and oxygen concentrations within each ingot or between the two ingots. The oxygen concentration for silicon produced in a reusable crucible is considerably lower compared to HEM silicon produced in a silica crucible. This is consistent because silica is a source of oxygen, and for the non-oxide reusable crucible this source of oxygen is not present.

Diffusion length data for the two ingots also shows no systematic pattern relating to the position of the ingot. For ingot #251K the middle position showed highest diffusion length, whereas the highest value was for the top position for ingot #239K. The defect map for a wafer near the middle of ingot #251K is shown in Figure 2. The background defect density is still quite low, however, in localized areas the defect density is high. The defect density area is larger for this wafer than that shown in Figure 1.

Summary

Silicon ingots produced by HEM have been characterized for grain size, orientation of grain boundaries, carbon and oxygen concentration, defect density and diffusion lengths. Large grains with vertical orientation grain boundaries are produced; however, detailed characterization of wafers from different positions in the ingot have shown some variation of properties. In some cases, top and bottom sections of the ingots have shown decrease in diffusion lengths as measured by SPV. Defect mapping of these wafers has shown low background defect density for all the wafers with slight increase in defect density in localized areas. The variation in solar cell performance may be due to slightly higher defect density in localized areas because the background density for different positions in the ingot is low. HEM silicon produced in reusable crucibles has also shown similar characteristics. If the defect density of localized areas can be reduced, HEM silicon has the potential for producing higher efficiency solar cells with good uniformity.

References

1. C.P. Khattak and F. Schmid, *Proc. 13th IEEE Photovoltaic Specialists Conf.* (IEEE, New York, 1978)p.137.
2. F. Schmid and C.P. Khattak, *Opt. Spectra* 15(5)65(1981).
3. C.P. Khattak and F. Schmid, in *Silicon Processing for Photovoltaics II*, C.P. Khattak and K.V. Ravi, eds., (North Holland, New York, 1987)p.153.
4. C.P. Khattak, F. Schmid, D.W. Cunningham and J.G. Summers, *Proc. 22nd IEEE Photovoltaic Specialists Conf.*, (IEEE, New York, 1991)p.976.
5. C.P. Khattak and F. Schmid, *Proc. 6th International Photovoltaic Science and Engineering Conf.*, (Oxford & IBH Publ., New Delhi, India, 1992)p.117.
6. F. Schmid and C.P. Khattak, *Laser Focus/Electro-Optics* 19(9)147(1983).
7. C.P. Khattak, A.N. Scoville and F. Schmid, in: *Infrared and Optical Transmitting Materials*, ed. R.W. Schwartz, SPIE Vol.683(1986)32.
8. K.A. Dumas, C.P. Khattak and F. Schmid, *15th IEEE Photovoltaic Specialists Conf.*, Orlando, FL (IEEE, NY, 1981)p.954.
9. W. Schmidt, W. Ebner, K.-D. Rasch and G. Wahl, *10th E. C. Photovoltaic Solar*

Energy Conf. Lisbon, Portugal (Kluwer Acad. Pub. Dordrecht, 1991)p.507.
10. T.M. Bruton, J.G. Summers, B.E. Lord, A.M. Mitchell, D.W. Cunningham, A.E. Hughes, K.C. Heasman, B.M. Neville and M. Lesniak, *Proc. 22nd IEEE Photovoltaic Specialists Conf.* (IEEE, New York)p.1010.
11. C.P. Khattak, F. Schmid, B. L. Sopori and W. K. Schubert, *Proc. 2nd Workshop on the Role of Point Defects/Defect Complexes in Silicon Device Fabrication*, Breckenridge, CO, 1992 (in press).
12. C. P. Khattak, F. Schmid, W. K. Schubert, M. Cudzinovic and B. L. Sopori, *23rd IEEE Photovoltaic Specialists Conf.*, Louisville, KY (IEEE, NY,1993).

(a)

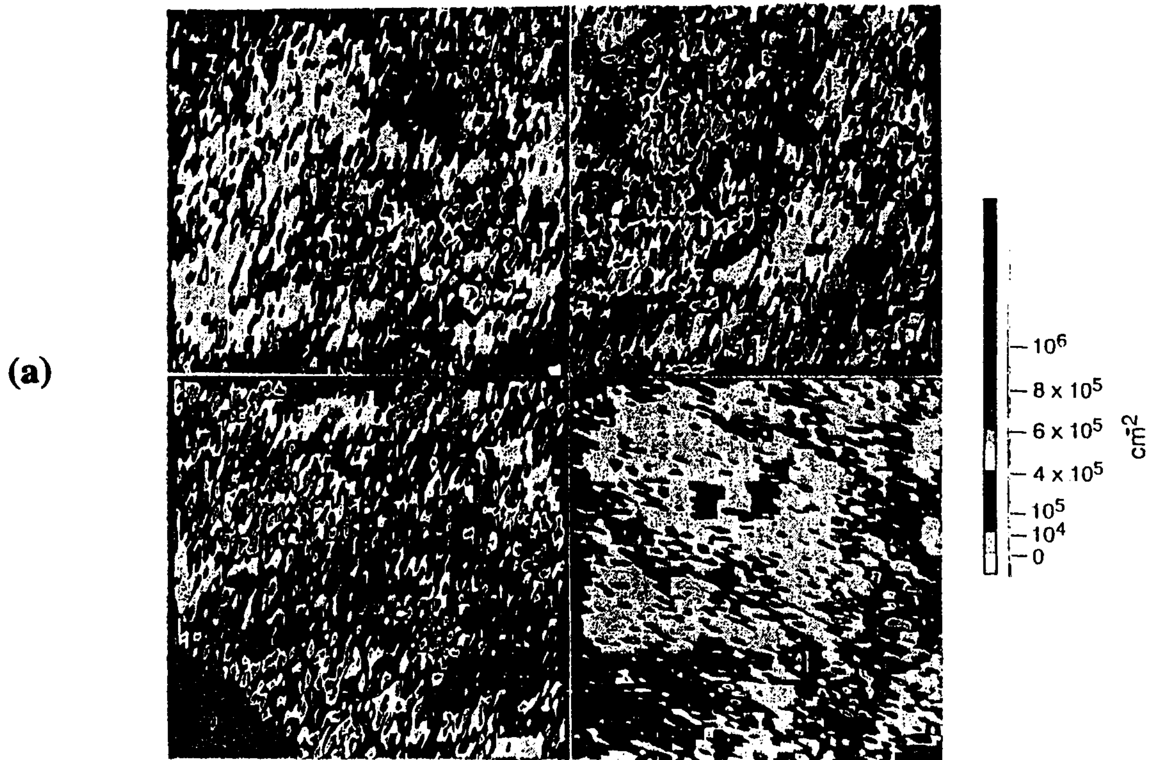

(b)

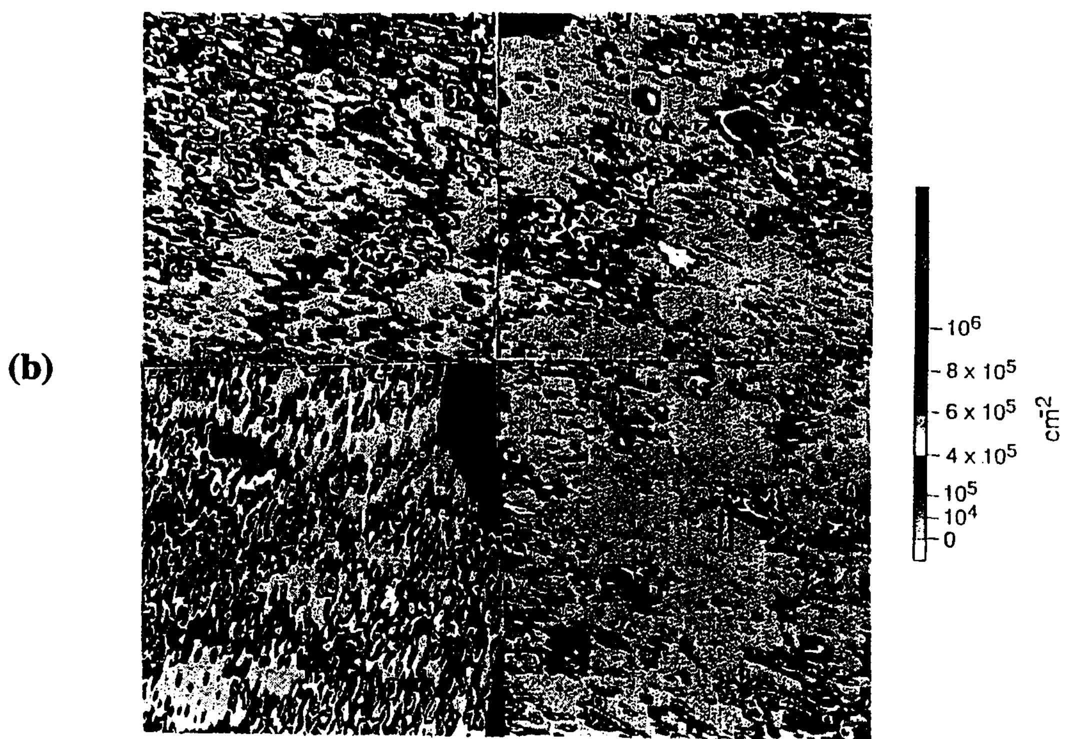

Figure 1: Defect density maps of sections from ingot #222K: (a) top of ingot; (b) bottom of ingot.

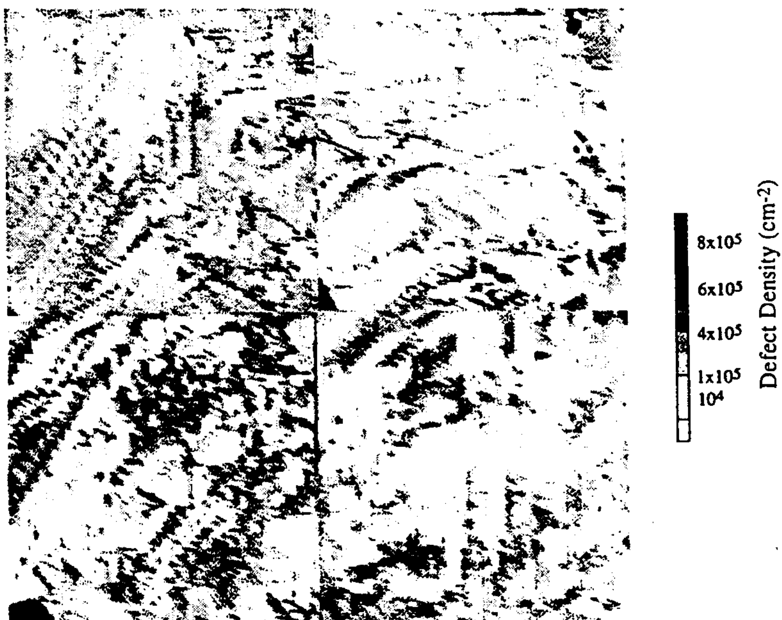

Figure 2: Defect density map of a section from the middle of ingot #251K

Table I. Carbon and oxygen concentration, diffusion length and resistivity for 33 cm square-cross section multicrystalline HEM silicon ingots produced in silica crucibles.

Ingot #	Position in Ingot	Carbon (ppma)	Oxygen (ppma)	Diffusion Length (μm)	Resistivity (Ω-cm)
217K	bottom	9.7	5.3	166	3.62
	middle	10.6	4.9	181	3.18
	top	9.5	2.3	215	3.16
222K	bottom	5.8	6.9	97	3.05
	middle	6.8	6.2	654	2.51
	top	13.0	2.9	209	2.21

Table II. Carbon and oxygen concentration, diffusion length and resistivity for 22 cm square-cross section multicrystalline HEM silicon ingots produced in reusable crucibles.

Ingot #	Position in Ingot	Carbon (ppma)	Oxygen (ppma)	Diffusion Length (μm)	Resistivity (Ω-cm)
239K	bottom	6.1	2.4	50	0.62
	middle	11.8	0.7	38	0.59
	top	16.3	0.0	188	0.77
251K	bottom	6.4	1.4	28	0.78
	middle	11.4	1.0	272	0.89
	top	14.4	1.5	23	0.65

ELECTRICAL BEHAVIOR OF DISLOCATIONS AND IMPURITIES IN SILICON

G.A. Rozgonyi, A. Agarwal, N. Braga, H. Kikuchi, S. Koveshnikov

Department of Materials Science and Engineering
North Carolina State University
Raleigh, NC 27695-7916

I. INTRODUCTION

The control of dopants, impurities, and defects during integrated circuit and solar cell processing processing requires a complex set of crystal and fabrication conditions to be satisfied simultaneously [1]. In order to achieve the maximum yield and the highest level of electrical performance for a given device design, absolute control of the introduction, activation, and redistribution of charge carriers must be maintained. However, complications arise due to interactions with metal contamination which degrades the minority carrier lifetime, compromises the gate oxide integrity, and enhances a variety of junction leakage mechanisms. The first line of attack against these problems has always been sustaining rigorous standards and environments for reducing particles and contamination. A second approach has been to incorporate gettering steps before, during, and after particularly vulnerable processes; or as a type of insurance against disaster. Since the specific technological need for gettering generally tracks the sensitivity of a particular device's performance (or yield) to structural or chemical defects it is necessary to distinguish between defects which are inherent in the as-grown crystal and those which are introduced during device processing. Defects are defined here in their most general form and can manifest themselves either structurally (dislocations, stacking faults, impurity precipitates), chemically (Na, O_2, Fe), or electrically (divacancy, vacancy/phosphorus pair, Fe-B pair). As might be expected, the device function, diode, transistor, MOS or bipolar interface, etc., will establish an interactive volume with a defect's extended strain field, chemical potential, recombination activity, etc. Device yield engineers are most interested in defects which are in an electrically active state, or become so when localized in the active region of a particular device where they can modify the concentration, mobility and lifetime of charge carriers. These issues will be discussed in this report in the context of several recent observations on the electrical behavior of dislocations and impurities.

A. Gettering Components

Nature allows such a wide variety of defect-assisted interactions that a global definition of gettering [2] has been stated as: "any procedure, intentional or otherwise (intrinsic or extrinsic), which alters the character or the density of defects in a single crystal". This definition, however, may be adapted to the device processing community in a more focused form as "the beneficial localization of impurities at sinks which are beyond the device's active region". Before impurities are captured by a defect, they must diffuse to the capture site and, in certain cases, an initial release of the impurity must be effected. Thus, we must evaluate three major components to the gettering process:

i) dissolution, or release from the source of impurities,

ii) diffusion towards the gettering zone, and

iii) capture at the gettering site.

In general, the processes of release and diffusion of impurities are time and temperature dependent and specific to each impurity. The balance of point defects in the host crystal lattice plays an important role. For example, an increase in the self-interstitial or vacancy concentration can result in either dissolution or further growth of precipitates and is usually determined by the sign of the precipitate-induced strain. The efficiency of diffusion towards the capture sites is also controlled by the dominant point defect and may be influenced by the presence of alternate sinks. The resulting effectiveness of the gettering process will depend on the specific reactivity of the capture site as it relates to solubility enhancement, coulombic pairing, capturing by extended defects, and the occurrence of co-precipitation. Finally, the thermal stability of the impurity/defect complex thus formed must be evaluated in the context of subsequent thermal processing. Achieving dimensional control in light of ever-decreasing circuit geometries [1], will necessarily limit the allowable thermal budget once dopants are introduced to form the source-drain region. Thus, a successful gettering strategy requires one to identify the limiting factor and the dominant driving force for each component of gettering, while simultaneously taking into account the specific features of the contaminants to be gettered, and the fabrication process being used.

The contaminants which are the most threatening are the 3d-elements, particularly Fe in Si, which are known to significantly alter carrier lifetime and device performance. Iron in silicon is characterized by a high diffusion coefficient and relatively low solubility. The solubility decreases strongly with decreasing temperature and increases with increasing doping level. The temperature dependence of solubility is much stronger than that of diffusivity for transition metals. In many practical cases, this factor plays a key role for

effective gettering thus Fe gettering strategies vary the temperature and duration of the gettering process to activate the impurity source and drive the diffusion process. The basic goal is to cause the iron to move in the desired direction and to efficiently and permanently localize the impurity in a neutral region of the wafer. To accomplish this goal and understand the microscopic nature of the gettering mechanisms one must consider the capture processes for metallic impurities in more detail.

B. Capture Processes

The nomenclature of capture mechanisms which govern gettering has evolved to the point where three mechanisms have been defined by Schröter et al [3]. These are:

i) Relaxation-induced gettering occurs at heterogeneous nucleation sites (e.g. SiO_2 precipitates in internal gettering) where supersaturated impurities precipitate or 'relax', usually during cooling from high processing temperatures. Trapping of the impurities in the gettering zone sets up a concentration gradient which facilitates further impurity diffusion away from the device's active regions. This mechanism can be used to explain the observation of Aoki et al. [4] who experimentally determined the temperature dependence for intrinsic gettering of Fe. They showed that the gettering process would stop or equilibriate when the Fe concentration in the denuded zone reached the solid solubility level for the specific gettering temperature. Thus, a serious limitation is projected for continuing to use internal gettering in future low temperature processing, since the supersaturation of metallic impurities required to initiate the gettering process may not provide a reduction of the metallic impurity concentration to below 10^{10} cm^{-3} [4].

ii) Segregation-induced gettering may occur without the presence of either heterogeneous nucleation sites or a supersaturated concentration of impurity. In this case gettering activity occurs due to the formation of a second phase, e.g. SiP, which locally increases the Si interstitial concentration, thereby enabling a reaction with metallic impurities [3]. This internal silicidation occurs at high temperatures, and has been shown to effect a redistribution of Fe ranging from 10^{17} cm^{-3} in the phosphorus-doped region to well below solubility elsewhere. Gilles et al. [5] demonstrated that such solubility enhancement exists for many 3d-transition elements in extrinsic n-type Si. Thus, a redistribution of impurities due to different solubilities in the bulk and a backside gettered layer can be achieved.

iii) Injection-induced gettering is a non-equilibrium mode of gettering triggered by the 'injection' of Si interstitials during high temperature processing such as oxidation.

Substitutionally dissolved metal impurities can couple with the Si self-interstitial current, as described by Schröter and Kuhnapfel for Co [6], but is only found to occur in extrinsic n-type material such as substitutional phosphorus dopant. This mode of gettering is of particular importance in n-type source/drain regions since interstitials are injected during subsequent processing.

From the point of view of gettering efficiency, thermal stability of gettered product, and flexibility of the process technology, the methods of intrinsic gettering at moderate temperatures (800-1000°C) and phosphorus diffusion gettering at high temperatures (900-1100°C) are currently the prime gettering choices. Unfortunately, backside phosphorus gettering places the capture zone too far from the device. In fact, bulk intrinsic gettering sites across several microns of denuded zone may also be too far removed for low temperature integrated circuit processing. The solution, in our opinion, is to develop methods of low temperature extrinsic gettering which offer three-dimensional placement and control of the density of defect capture sites such that they can be integrated into the top surface of a device wafer.

II. ELECTRIC FIELD EFFECT ON FeB/Fe_i PAIR DISSOCIATION/ REASSOCIATION

Iron is known to easily become incorporated in a silicon crystal during various stages of device processing involving thermal treatment and can cause the degradation of silicon device parameters (leakage current, recombination/generation lifetime, etc.). In p-type silicon iron combines easily with the acceptor dopant boron, resulting in the formation of an Fe-B defect complex. Dissociation of the Fe-B pairs can be achieved by heat treatment, irradiation with white light [7], or by minority carrier injection [8]. In n-type silicon, however, Fe-B pair formation does not occur, even when a significant background acceptor (boron) concentration is present [9]. This indicates that the Fe-B pair formation process is determined to a great extent by the charge state of isolated iron atoms. Kimerling et al. have shown that changing the charge state of interstitial iron, Fe_i, by applying a reverse bias to Schottky diodes can suppress the pairing reaction [8]. Further evidence for the charge state dependence of Fe was provided by Mesli et al. in their study of Fe precipitation in p-type silicon under a reverse bias [10]. Since many silicon devices (p/n junctions, Schottky junctions or MOS structures) are used under reverse bias and sometimes operate at temperatures near 100°C, it is useful to examine the annealing behavior of Fe in the depletion region of reverse biased devices. The results of a recent study [11] of the annealing behavior of the Fe-B pairs and their dissociation kinetics in an

electric field are briefly summarized here. Experimental evidence has been obtained which shows that, while the Fe-B pair dissociation reaction is thermally enhanced, the process is electronically controlled. Significant degradation of device parameters due to released Fe under actual device operation conditions has been found. Boron-doped 10 to 20 Ω-cm (100) Czochralski (CZ) silicon wafers were used in Ref. [11]. Fe was introduced onto the wafer surface by spin coating. The wafers were then annealed at 950°C for 30 min in a dry oxygen ambient to drive the surface Fe into the silicon bulk. After annealing, 15 to 20 μm of Si was removed from both surfaces by etching the wafers in a KOH solution. Schottky contacts, 1 mm in diameter, were made by evaporation of Al, while ohmic contacts were made by application of a Ga/In alloy on the back surface. The samples were then heat treated from room temperature to 100°C, with and without a reverse bias to dissociate Fe-B pairs, and then immediately quenched in liquid nitrogen to minimize the re-association. The concentration and depth profiles of the interstitial iron were measured by detecting iron related $H(E_V + 0.43$ eV$)$ deep level centers using DLTS.

The upper two curves in Fig. 1 are the DLTS spectra for samples annealed for 30 min at 100°C under conditions of a 5V reverse bias and a zero bias. These results show that the concentration of Fe_i ($E_v + 0.43$ eV) increases when a reverse bias is applied during the anneal. The depth profiles of the Fe_i related center as a function of different reverse bias conditions during annealing at 100°C for 20 min are presented in Fig. 2. Note that the increase in Fe_i concentration is limited to the region depleted during the anneal. Beyond the depletion region, indicated by the arrows at the top of the figure, the concentration of the released Fe is the same as in the unbiased sample. It is clear that enhanced Fe-B pair dissociation took place only inside the depletion region. The lower two curves in Fig. 1 also compare the DLTS spectra for room temperature samples with and without a reverse bias of 5V for 20 hours. The fact that dissociation of Fe-B pairs can be initiated even at room temperature in the presence of a reverse bias, leading to the formation of interstitial Fe, is expected to impact the time dependent performance of electronic devices. These results clearly reaffirm that the dissociation reaction $FeB \rightarrow Fe_i + B$ can be initiated by an electrical field. In addition, opportunitie for field induced localization of Fe impurities, i.e. gettering can be explored since the re-association of thermally separated Fe and B atoms is suppressed by the electric field, presumably because the isolated Fe is in the neutral state, as in n-type Si.

III TEMPERATURE DEPENDENCE OF EBIC DISLOCATION CONTRAST

It is by now generally accepted that the electrical activity of structural defects can not easily be separated from that of the impurities which may "decorate" them [12]. Chemical impurities are readily attracted by the strain field of structural defects resulting in the formation of a structural/chemical defect complex. The defect comlexes can then act as a nucleation site for precipitate formation. The collection of impurities onto extended structural defects results in local field enhancement and possibly failure of devices containing the defects. This effect is dramatically demonstrated during temperature dependent EBIC experiments. Figure 3 compares EBIC micrographs of Ni decorated misfit dislocations at room temperature and 120K [13]. Note that while precipitates are in strong contrast at room temperature the dislocation lines only become visible at low temperatures. The results have been explained by considering the dependence of recombination lifetime on temperature, as described by Shockley-Read-Hall (SRH) theory. The SRH theory predicts that the recombination activity of shallow level defects is lower at room temperature and increases as the temperature is reduced; whereas that of deep level defects is high at room temperature and essentially independent of room temperature. Thus, the EBIC image of an undecorated "clean" MD which only becomes visible at low temperatures, is consistent with a defect associated with a shallow energy level.

Recently, quantitative analyses of the temperature dependence of EBIC contrast have been carried out [14,15] on our MD in as-grown and contaminated material. Figure 4 compares the temperature dependent experimental EBIC contrast with that predicted by SRH theory. A positive ($T^{1/2}$) SRH dependence of contrast on temperature for non-interacting deep-level point defects associated with MD has been matched with experimental findings for MD decorated with Cu, see curve 1 in Fig 4. The predicted negative temperature dependence for very shallow levels is also in agreement with the experimental data on weakly contaminated MD, see curve 2 in Fig. 4. The above results are from separate MD in the same intentionally contaminated wafer. In as-grown material, however, when the MD are presumably not decorated, the contrast is below 0.5% [15]. It has been proposed, although not proven, that the very low contrast is due to passivation of the MD by hydrogen [15]. Supporting evidence for clean and passivated MD has been presented using radiative recombination, studied by photoluminescence of the well known D-band lines [16], which are only detectable for MD contaminated with Cu [15]. Since the D-bands are not seen for the undecorated MD in the contaminated material, or for the MD in the as-grown material, a direct correlation exists with the room temperature EBIC.

IV PIPE DIFFUSION AND CYLINDERICAL p/n JUNCTION FORMATION

The formation of cylindrical doped regions surrounding dislocations in Si/Si(Ge) heterostructures can be of great interest for understanding the electronic behavior of defects. Internal electric fields around plastically formed dislocations, giving rise to a diode behavior, have been detected previously for very lightly doped material at low temperatures [17,18]. Prospects for the utilization of such buried junctions in novel device structures was discussed. More recently [19,20], dislocations have been decorated with metal impurities, e. g. closely spaced (< 50 nm) colonies of Au clusters precipitated along dislocations during diffusion from a back side evaporated gold layer. In this way a continuous layer of internal electric field forms due to overlapping depletion regions of neighboring precipitates. However, the formation of a continuous junction by pipe diffusion of a dopant seems to be more effective and controllable for that purpose. Experimental evidence for the formation of n/p junction diodes by arsenic diffusion along individual interfacial misfit dislocations in *p*-type epitaxial Si/Si(Ge)/Si has recently been presented in Ref [21]. Multiple boron doped ($N_A \approx 1 \times 10^{16}$ cm^{-3}) epitaxial layers have been grown on heavily doped p-type substrates starting with a 5 mm thick pure Si buffer layer, which isolates the p^+ substrate from the misfit dislocations (MD) subsequently formed during Si(Ge) growth. The MD location and density have been controlled by adding GeH_4 to a $SiCl_3H$ CVD reactor at approximately 1080°C, and then burying the 2 mm thick Si(Ge) layer with a 1.5 mm thick pure Si capping layer. The Ge concentration in the alloy is ≈3.5%. Two interfacial planes of predominantly 60° dislocations are present between the capping (upper interface) and buffer (lower interface) layers. The multi layer Si/Si(Ge)/Si structures were then fabricated into trenches and mesas, as shown schematically in Fig. 1(a), using a 5000 Å masking oxide deposited at 450°C, photolithographically patterning into stripes, and then anisotropically etching with a 10% solution of KOH at 80 °C to expose (111) faceted side walls. The depth of the trenches was adjusted such that dislocations in the upper interfacial plane emerged from the mesa side walls, whereas dislocations in the lower plane were located just below the bottom of the trenches. An *n/p* junction, shaded light gray in Fig. 5(a), was selectively formed in the trenches and along the side walls of the mesa via a 180 keV As^+ implantation to a dose of 1 x 10^{16} cm^{-2}. The initial oxide, which prevented implantation of the top mesa surface, was then removed and a second blanket oxide was deposited to avoid dopant out diffusion during the As drive-in diffusion. The drive-in was performed in N_2 at 1000°C for 24 h. Samples without an arsenic implant were processed along as reference wafers.

Following diffusion, the samples were characterized using chemical etching, SEM and EBIC/SEM. The existence of a space charge region can be seen in an EBIC/SEM image since its built-in electrical field separates the electron-hole pairs generated by the electron beam, giving rise to a generation current, i. e., a white contrast in an EBIC micrograph. Conversely, the presence of the decorated dislocations gives a local increase in electron-hole recombination yielding a dark contrast in EBIC micrographs. Furthermore, low temperatures improve the built-in voltage in *pn* junctions and increase the recombination rate by activating shallower energy levels in the forbidden gap [19], further increasing the EBIC contrast capabilities. Figure 5 compares an EBIC/SEM image obtained at $\approx$ 83 K with a schematic of the trench/mesa geometry containing misfit dislocations. The white areas correspond to space charge regions emanating from the *n/p* junctions formed in the trenches and along the buried dislocations; whereas the unimplanted mesas appear dark. Going from the bottom of the trench to the mesa surface, a narrow dark band occurs due to a decrease in electron-hole pair generation resulting from the incidence angle between the scanning beam and the sloping (111) side wall. The contrast becomes brighter again near the mesa edge where the *n/p* junction under the mesa is defined.

Note that arsenic diffuses faster along the misfit dislocations, forming cylindrical or conical diodes, which in the case of trenches separated by 10 mm actually traverse across two adjacent mesa side walls, as shown in the right hand side of Fig. 5(b). Figure 6 shows a magnified EBIC/SEM image, taken at room T, where dark recombination contrast is present at the center of the dislocation diode due to a local increase in electron-hole pair recombination at the dislocation itself. This dark recombination line surrounded by bright bands also verifies that the interfacial misfit dislocations provide a path for diffusion enhancement. The arsenic then proceeds to diffuse radially away from the dislocation core to yield the observed cylindrical *n/p* diodes. The presence of a dark recombination contrast in the vicinity of dislocations in room temperature EBIC micrographs suggests that dislocations are decorated with process-induced impurities, an As/MD complex, or As precipitation capable of introducing deep levels in the energy bandgap.

Although the above EBIC images illustrate the role of misfit dislocations in enhancing arsenic diffusion, the spatial resolution is limited by the EBIC carrier diffusion length. Therefore, a conventional SEM examination following bevel polishing and concentration dependent etching was used to reveal doped dislocations more precisely. Figure 7 gives a side by side comparison of the isoconcentration profiles along individual dislocation and that caused by bulk diffusion in from the trench side wall. Both doped and undoped reference trench/mesa structures are given in Figs. 7(a) and 7(b), respectively. These samples were low angle ($\approx$8') bevel polished with Syton to expose the upper plane

of MD's, and then given a 10 sec concentration dependent etching with $HF:HNO_3:CH_3COOH$ (1:40:20). The isoconcentration contour delineated by the etching procedure is estimated to correspond to 10^{18} As cm^{-3} [22]. It is apparent that arsenic diffuses more rapidly down the dislocation core and then radially outward with a bulk diffusivity as defined by the contour parallel to the trench side wall. Dislocations in the undoped reference are also delineated by the etching procedure, as illustrated in Fig. 3(b) and have a constant width. It is also apparent that the diffusion process does not occur uniformly along each misfit dislocation since each of the four dislocations in Fig. 7(a) induced different arsenic effective diffusivities.

The electrical behavior of doped dislocations and the mechanism through which a dislocation influences the diffusion process is also the object of intensive work in progress. It is hoped that the continuing development of doped dislocation pipes and improved understanding of their electrical properties will lead to new options for fabricating novel structures with dislocations as active elements, as well as providing opportunities for more detailed analysis of defect/dopant interactions.

V HYDROGEN PASSIVATION OF DISLOCATION RELATED DEFECTS/ D-band LUMINESCENCE

Dislocations in Si crystals generally exhibit a characteristic photoluminescence (PL) spectrum, with four distinct peaks labeled D1 through D4 [16]. Experimental evidence has been found showing that D1, D2 and D3, D4 form pairs which behave similarly [16]. Annealing of Si crystals containing dislocations which exhibit the D-band PL in an atomic hydrogen environment has been found to lead to passivation of the PL activity of the defects. An example from recent work of the type of passivation which can be obtained by hydrogen annealing at different temperatures is shown i n Fig. 9 [24]. Photoluminescence spectra of n- and p-type Si containing dislocations after annealing in a hydrogen environment at various temperatures from 100°C to 600°C are shown. Also presented, for comparison, are the spectra for unannealed reference samples as well as for samples annealed in an Ar atmosphere at 300°C. Two points should be made about the hydrogen passivation in general: firstly, that the passivation is preferential, i.e, the four defect signals are not passivated in the same ratio at any given temperature; and secondly, while a defect may be passivated by hydrogen at a given temperature, at a higher temperature the hydrogen may be released allowing the defect to be activated again. An example of the latter point is the D1 peak in Fig. 8, compare spectrum after 400°C with spectrum after 600°C.

REFERENCES

1. H.R. Huff, "Silicon Materials For The Mega-IC Era", presented at ULSI Science and Technology Symp. ECS, May 1993, Honolulu, Hawaii
2. K.E. Bean, K. Lindberg, and G. Rozgonyi, ECS Proc., **88-19**, 3 (1988)
3. W. Schröter, M.Seibt, and D.Gilles, Mater.Sci. and Techn., **4**, 541 (199)
4. M. Aoki, A. Hara, and A. Ohsawa, J.Appl.Phys. **72**, 895 (1992).
5. D. Gilles, E.R. Weber, and S. Hahn, Phys. Rev. Lett . **64**, 196 (1990).
6. W. Schröter and R. Kuhnapfel, Appl. Phys. Lett. **56**, 2207 (1989).
7. K. Graff and H. Pieper, J. Electrochem. Soc. **128**, 669 (1981)
8. L. C. Kimerling and J. L. Benton, Physica **B116**, 297 (1983)
9. E. R. Weber, Appl. Phys. **A30**, 1 (1983)
10. A. Mesli, T. Heiser, N. Amroun and P. Siffert, Appl. Phys. Lett. **57**, 1898 (1990)
11. H. Kikuchi, A. Agarwal, S. Koveshnikov and G.A. Rozgonyi, ECS Proceedings Vol., New Orleans Meeting, Oct 1993.
12. Z.J. Radzimski, T.Q. Zhou, A. Buczkowski, G. A. Rozgonyi, Appl. Phys. A **53**, 189 (1991).
13. Z.J. Radzimski, T.Q. Zhou, A. Buczkowski, G. A. Rozgonyi, D. Finn, L.G. Hellwig, and J.A. Ross, Appl. Phys. Lett. **60**, 1096 (1992).
14. M. Kittler, W. Seifert and Z.J.Radzimski, Appl. Phys. A **52** (20), 2513 (1993).
15. M. Kittler, C. Ulhaq-Boulliet and V. Higgs, in press, Proceedings of BIADS'93 Meeting, Bologna, Italy, Aug.1993.
16. M. Suezawa, K. Sumino and Y. Nishna, Jap. J. Appl. Phys. **21**, L518 (1982)
17. S. Mil'shtein, *J. De. Physique*, **40**, 6, 207 (1979).
18. S. Mil'shtein and A. Senderichin, *Phys. Stat. Sol. B*, **109**, 429 (1982).
19. G. A. Rozgonyi and R. R. Kola, in *Defect Control in Semiconductors*, K. Sumino, Ed.,North-Holland, pg. 579 (1990).
20. Z. J. Radzimski, T. Q. Zhou, A. Buczkowski, and G. A. Rozgonyi, *Appl. Phys. A*, **53**, 189 (1991).
21. N. Braga, A. Buczkowski, and G. A. Rozgonyi, submitted to Appl. Phys. Lett.
22. B. Zhang, D. M. Maher, M. S. Denker, and M. A. Ray, in press, *MRS Proc.*, **303**, (1993)
23. Z. J. Radzimski, T. Q. Zhou, A. Buczkowski, and G. A. Rozgonyi, Appl. Phys. Lett. **60**, 1096 (1992).
24. K. Weronek, J. Weber and H.J. Queisser, Phys. Stat. Sol. (a) **137**, 543 (1993).

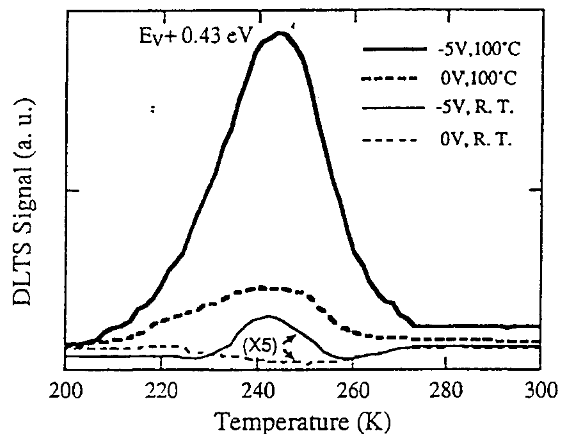

Fig. 1. DLTS spectra for samples annealed at different temperatures (100°C for 30 min, RT for 20 hrs) with or without a -5V bias.

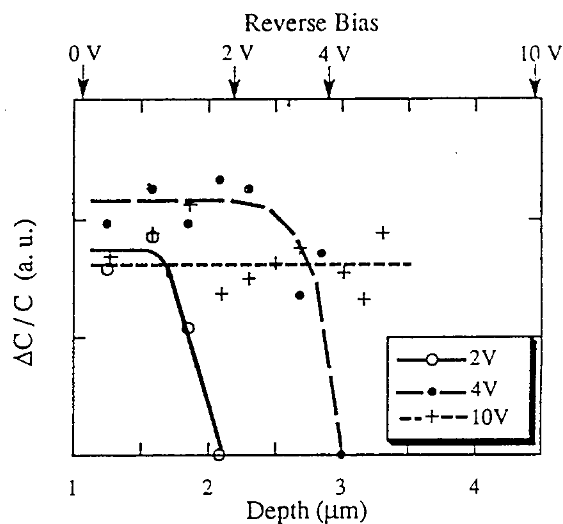

Fig. 2 Depth profiles of Fe_i for samples under different biasing conditions (2V, 4V and 10V) during annealing at 100°C for 20 min.

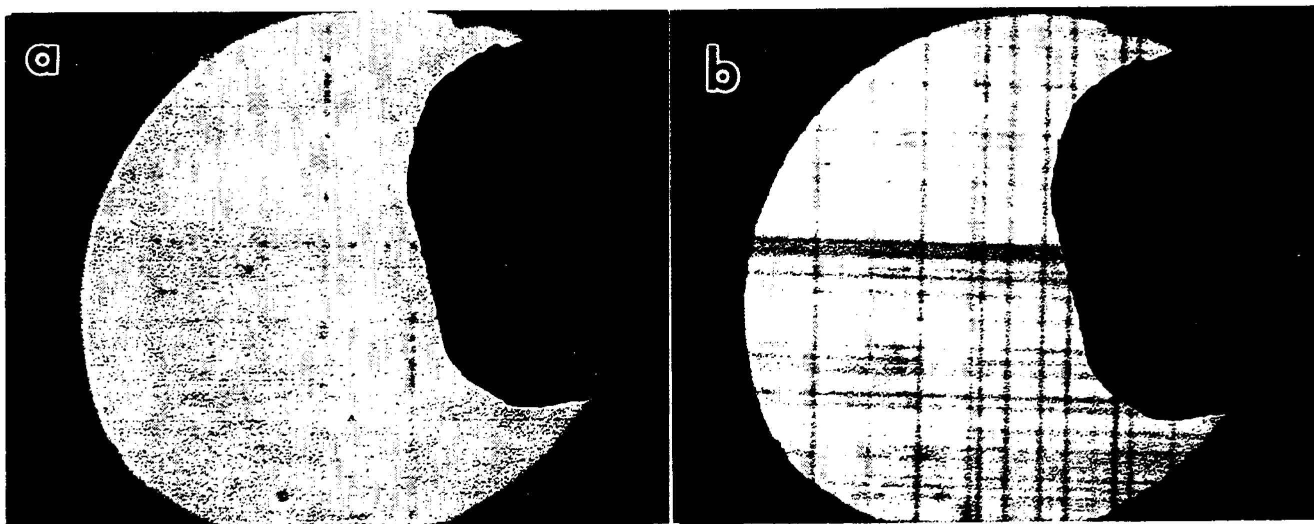

Fig. 3 - EBIC/SEM image of heterostructure with MD decorated with Ni at 1000°C obtained at (a) room temerature and (b) at 120K.

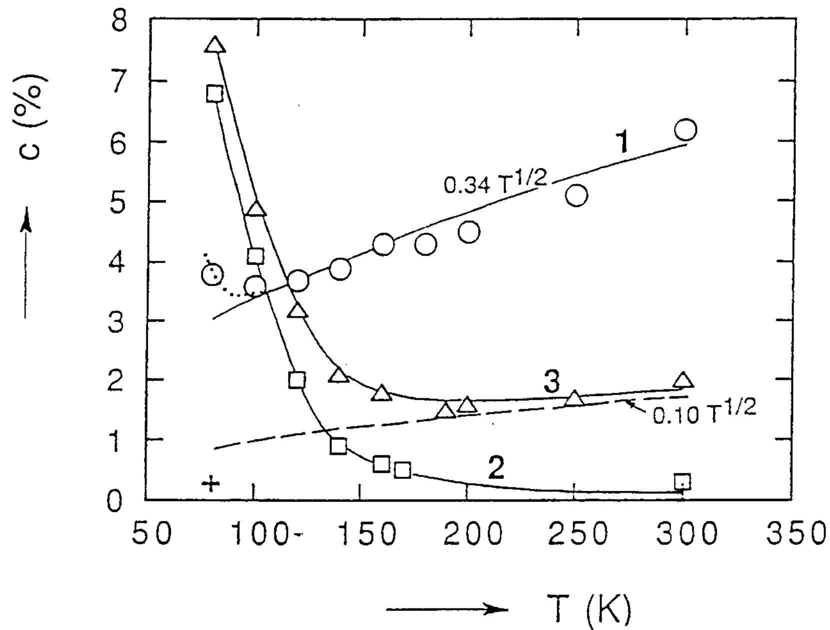

Fig. 4 - EBIC contrast plotted as a function of temperature for three different dislocations: 1 - contaminated with Cu, 2- not contaminated and 3 - weakly contaminated. Measurement conditions: beam energy -30 keV, beam current 50 pA [16]

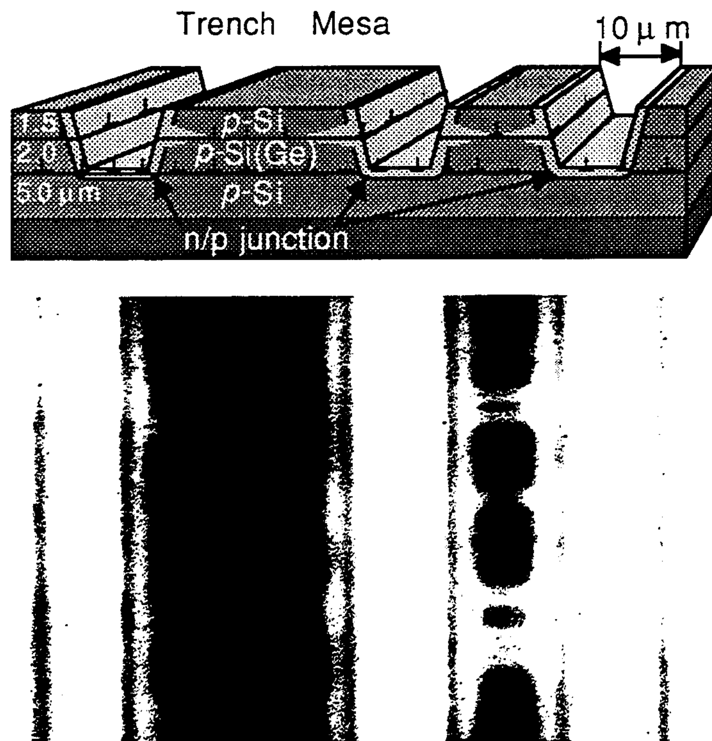

Fig. 5 - (a) Schematic perspective of a trench/mesa Si/Si(Ge) structure used for enhanced diffusion analysis and (b) Matching plan view EBIC/SEM image, taken at 83 K.

Fig. 6 - Plan view EBIC/SEM image, taken at room temperature, showing an individual dislocation diode with a dark recombination line in the center.

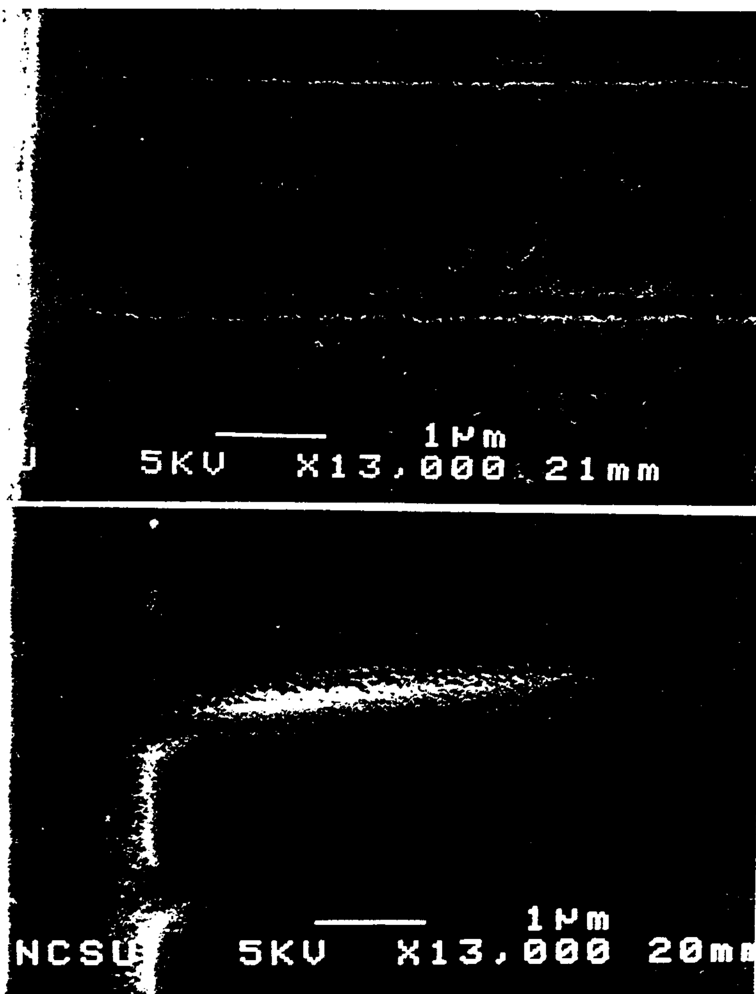

Fig. 7 - SE/SEM micrographs of polished and concentration dependent etched trench structures: (a) arsenic implanted and (b) reference samples.

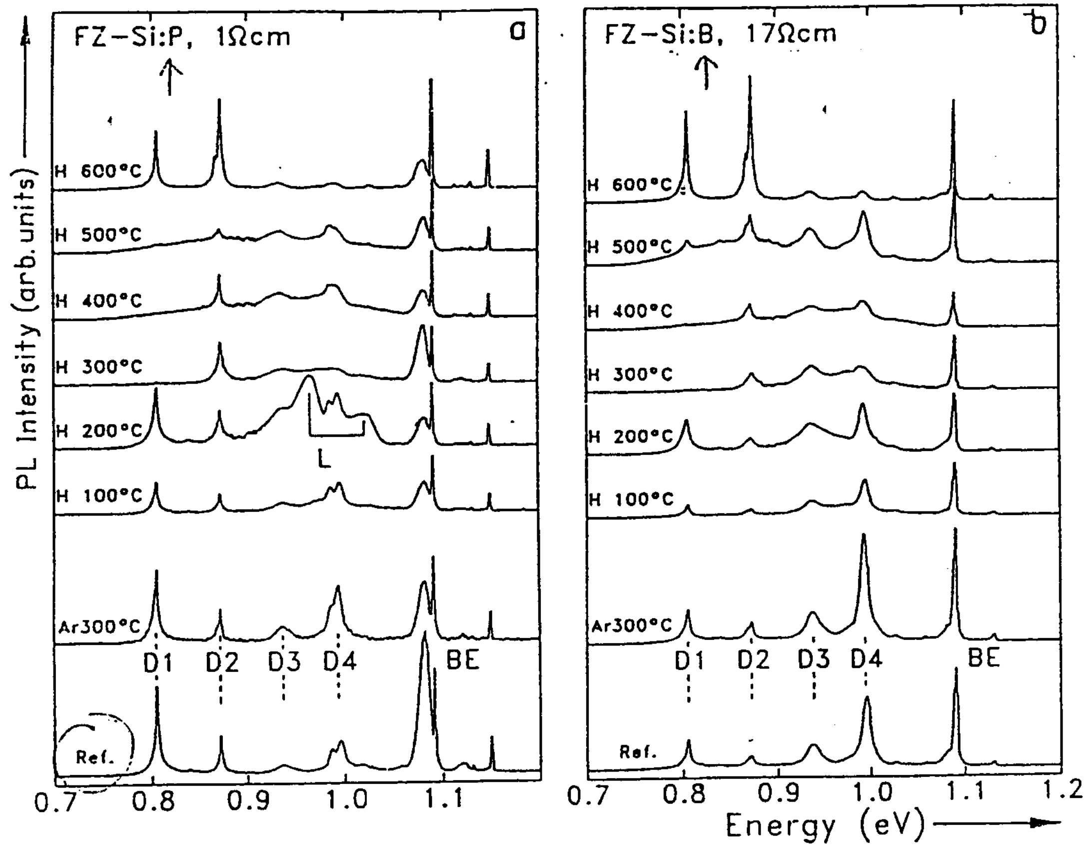

Fig. 8 - Photoluminescence spectra of differently treated silicon doped with (a) phosphorus (1 Ω cm) and (b) boron (17 Ω cm). The samples are excited with 150 mW of the 514.5 nm line of an Ar ion laser at 1.7 K. The sample of the Ref. spectrum is not treated. The samples of the other spectra are treated for 4 h at the indicated temperatures and atmospheres.

Characterization of Carbon in EFG Silicon using the G-Center

William D. Sawyer, Gordon Davies*, Seung-Chul Park*, and Victor Higgs*

Mobil Solar Energy Corporation, 4 Suburban Park Drive, Billerica, MA 01821
* Physics Department, King's College London, Strand, London WC2R 2LS, UK

Abstract

Edge-defined film-fed growth silicon (EFG) silicon contains a high carbon concentration. We characterize the carbon concentration by irradiating EFG silicon samples with 2 MeV electrons which creates the well known G-Center defect. Previous studies of the G-Center in CZ and FZ silicon provide detailed knowledge of the kinetics of its formation during electron irradiation as well as its destruction by annealing. In addition, it is possible to calculate the absorption strength of the G-center as a function of radiation dose and of carbon, oxygen and boron concentration. We show that the G-Center kinetics of formation and destruction in EFG silicon are the same as those measured in CZ and FZ silicon. We also demonstrate that the absorption strength of the G-Center in EFG silicon agrees with similar measurements made on CZ and FZ silicon. From these quantitative measurements we conclude that the carbon concentration in EFG silicon behaves exactly as similar carbon concentrations contained in CZ and FZ silicon and that there are no interstitial silicon traps specific to EFG silicon.

References

The work described above will be published in two papers;

1. "Traps for excitons and interstitial atoms in edge-defined film-fed growth silicon", Gordon Davies, Seung-Chul Park, V. Higgs and William D. Sawyer, Appl. Phys. Lett. 63, #13, Sept. 27 (1993).
2. "Carbon as a probe of edge-defined film-fed growth silicon", Seung-Chul Park, Gordon Davies, Victor Higgs and William D. Sawyer, in *Proceedings of the 17th International Conference on Defects in Semiconductors*, edited by B. Jäntsch and H. Neinrich, (Trans Tech, Zürich, 1994).

DIFFUSION-SEGREGATION EQUATION FOR SIMULATION IN HETEROSTRUCTURES

T. Y. Tan, R. Gafiteanu, H.-M. You, and U. Gösele

Department of Mechanical Engineering and Materials Science
Duke University
Durham, NC 27708-0300

ABSTRACT

The diffusion-segregation equation, which treats the diffusion and segregation processes simultaneously, has been derived recently. This equation is applicable to all cases for which the segregation phenomenon occurs. We first review the derivation of this equation and then show some examples of using it to simulate the diffusion-segregation processes in heterostructures, including real and hypothetical cases. The diffusion-segregation species can be either impurity atoms or point defects, and the host crystal can be either a single phase containing inhomogeneities or consisting of heterostructures.

I. INTRODUCTION

Real crystals contain either inhomogeneities or are consisting of heterostructures, including many nominally single crystals. Diffusion of impurity atoms or point defect species in these materials therefore occurs simultaneously with the segregation process, because the impurity and point defect solubilities are not the same in the different material regions. Due to processing needs in electronic device fabrications, simulation of the diffusion processes has already become a substantial field of studies. In general, in these studies the segregation phenomena have not been included, for two reasons. First, for many cases, the effect of segregation can be small and therefore ignorable. Second, there lacks a correct and general equation describing simultaneously the diffusion and segregation processes. This means that the segregation phenomena can not be simulated with confidence. In association with a study of charged Ga vacancy diffusion-segregation processes in GaAs and AlAs/GaAs superlattice (SL) crystals consisting of alternating n-doped and intrinsic regions, we have recently derived the diffusion-segregation equation.[1] This equation is applicable to all cases involving the diffusion-segregation processes, just as Fick's second law is applicable to all cases involving the diffusion process. In this paper, we first review the derivation of the diffusion-segregation equation, and then apply it to simulate the diffusion-segregation phenomena, including the fitting of some experimental results as well as some hypothetical cases. The possibility of simulating impurity gettering processes in Si is especially emphasized, since we can now define some of the needed parameters on a much better confidence level.

II. THE DIFFUSION-SEGREGATION EQUATION

The diffusion-segregation equation is derived on a thermodynamic basis. Segregation phenomenon occurs because the Gibbs free energy of formation of a (point defect or impurity) species is different in the different material regions, i.e., it is a function of the spatial coordinate x, $g^f(x)$. Now, the Gibbs free energy *density* of the material is given by

$$G(x) = C(x)\, g^f(x) - k_B T \ln \frac{C_o!}{[C_o - C(x)]!\, C(x)!}, \tag{1}$$

where C(x) is the concentration of the species at x, k_B is Boltzmann's constant, T is the absolute temperature, and C_0 is the crystal lattice site density. In Eq. (1) the second term on the right-hand side results from the entropy of mixing. The chemical potential at x, $\mu(x)$, is

$$\mu(x) = \frac{\partial G(x)}{\partial C(x)} = g^f(x) + k_B T \ln\left[\frac{C(x)}{C_o - C(x)}\right] \approx g^f(x) + k_B T \ln \frac{C(x)}{C_o}. \tag{2}$$

The rightmost term in Eq. (2) obtains for $C_0 >> C(x)$ holding. In thermal equilibrium $\mu(x)=0$ holds, and hence

$$k_B T \ln \frac{C^{eq}(x)}{C_o} = - g^f(x), \tag{3}$$

where $C^{eq}(x)$ is the thermal equilibrium concentration of the species at x, also holds. Therefore, we have

$$\mu(x) = k_B T \ln \frac{C(x)}{C^{eq}(x)}. \tag{4}$$

The force exerted on a point defect or an impurity atom by the chemical potential is

$$f(x) = -\frac{\partial \mu(x)}{\partial x} = -k_B T\left[\frac{1}{C(x)}\frac{\partial C(x)}{\partial x} - \frac{1}{C^{eq}(x)}\frac{\partial C^{eq}(x)}{\partial x}\right]. \tag{5}$$

This force accelerates the point defect or impurity atom at x to the velocity

$$v(x) = M\, f(x), \tag{6}$$

where M is the species' mobility. The flux equation is

$$J(x) = C(x)v(x) = C(x)\, M\, f(x) = -k_B T M\left[\frac{\partial C(x)}{\partial x} - \frac{C(x)}{C^{eq}(x)}\frac{\partial C^{eq}(x)}{\partial x}\right]. \tag{7}$$

Using the Einstein relationship that $M = D/k_B T$, where D is the species' diffusivity, and dropping the notation (x), the flux equation becomes

$$J = -D\left(\frac{\partial C}{\partial x} - \frac{C}{C^{eq}}\frac{\partial C^{eq}}{\partial x}\right). \tag{8}$$

Incorporated into the continuity equation, Eq. (8) yields the *diffusion-segregation equation* (DSE)

$$\frac{\partial C}{\partial t} = \frac{\partial}{\partial x}\left[D\left(\frac{\partial C}{\partial x} - \frac{C}{C^{eq}}\frac{\partial C^{eq}}{\partial x}\right)\right]. \tag{9}$$

Equation (9), the DSE, accounts for both the diffusion and the segregation processes of a point defect or impurity species in a crystal. Equation (9) has two terms on the right-hand side (RHS), the first is the usual diffusion term and the second is the segregation term. If an expression of C^{eq} is available, Eq. (9) can be used to simulate the diffusion-segregation processes, or else measured segregation coefficient can be used instead. To illustrate the latter point, we define the (thermal equilibrium) segregation coefficient of the species k as

$$k(x) = \frac{C^{eq}(x)}{C^{eq}(x_1)}, \tag{10}$$

where $C^{eq}(x_1)$ is the species' solubility at an arbitrarily chosen reference point 1 or reference crystal region 1. Using Eq. (10), the segregation term on the RHS of Eq. (9) is normalized to yield the more general form of the DSE

$$\frac{\partial C}{\partial t} = \frac{\partial}{\partial x}\left[D\left(\frac{\partial C}{\partial x} - \frac{C}{k}\frac{\partial k}{\partial x}\right)\right]. \tag{11}$$

The parameters used in the DSE, D and k or C^{eq}, are thermodynamic quantities instead of dynamic or kinetic quantities. The kinetic aspects, such as the time and position dependent fluxes etc. are accounted for by the DSE itself. Equation (11) is of a rather convenient form in that, aside from D, it uses only the dimensionless segregation coefficient k. The quantities D, k, and C^{eq} are experimentally measurable. Upon examining the DSE, Eqs. (9) and (11), two physical aspects about the segregation process become readily apparent. First, the segregation process is not independent from the diffusion process since atom and/or point defect migrations are involved. This is seen from the segregation term in Eq. (9) or (11), which is associated with the diffusivity D of the species. Second, the segregation process is driven by the gradient of the segregation coefficient, which balances the species concentration gradient in steady state.

III. SIMULATION RESULTS

A. Triply-Negatively-Charged Vacancies in GaAs

Our first application of the DSE is the study of the indiffusion-segregation behavior of the triply-negatively-charged Ga vacancies V_{Ga}^{3-} in GaAs and in AlAs/GaAs superlattice (SL) crystals.[1] Under intrinsic and n-doping conditions, V_{Ga}^{3-} governs the Ga

self-diffusion, Al-Ga interdiffusion, and the diffusion of the donor species Si in these materials. For heavily n-doped crystals, there are a number of outstanding experimental results requiring the interpretation that V_{Ga}^{3-} has reached its thermal equilibrium concentration $C_{V_{Ga}^{3-}}^{eq}(n)$ at the onset of each high temperature experiment for which the crystal was grown or first heat-treated at a lower temperature. This could be due to one of two reasons. First, it could be because of the fact that in heavily n-doped GaAs and AlAs/GaAs SL the $C_{V_{Ga}^{3-}}^{eq}(n)$ values are quite temperature independent. This has been shown to be the case by a thermodynamic calculation.[2] Second, it could be due to the fact that the indiffusion process of V_{Ga}^{3-} from the crystal surface to populate the appropriate interior n-type regions of the materials is extremely rapid so that the transient time needed for populating V_{Ga}^{3-} to the appropriate $C_{V_{Ga}^{3-}}^{eq}(n)$ values in crystal regions of experimental interests constitutes only a negligibly small portion of the total diffusion time. This has been shown to be not the case by simulating the V_{Ga}^{3-} indiffusion process using the DSE.[1] Figure 1 shows one such simulation result, relevant to the experimental results of Mei et al.[3]

This result demonstrated that, when it is assumed V_{Ga}^{3-} is undersaturated at the onset of the experiment, then V_{Ga}^{3-} is still understated by many orders of magnitude in the appropriate n-type regions of experimental interest even at the end of the experiment. While the simulation and experimental details were given elsewhere,[2,3] we mention here that, in order to use the DSE, Eq. (9) or (11), $C_{V_{Ga}^{3-}}^{eq}(n)$ is given by

$$C_{V_{Ga}^{3-}}^{eq}(n) = C_{V_{Ga}^{3-}}^{eq}(n_i)\left(\frac{n}{n_i}\right)^3 , \qquad (12)$$

where n is the electron concentration, n_i is the intrinsic carrier concentration and $C_{V_{Ga}^{3-}}^{eq}(n_i)$ is the V_{Ga}^{3-} thermal equilibrium concentration under intrinsic conditions. Using Eq. (12), Eq. (9) yields

$$\frac{\partial C_{V_{Ga}^{3-}}}{\partial t} = D\frac{\partial}{\partial x}\left[\frac{\partial C_{V_{Ga}^{3-}}}{\partial x} - 3C_{V_{Ga}^{3-}}\frac{\partial}{\partial x}\ln n\right], \qquad (13)$$

which is the actual expression used in the simulation calculations. Equation (13) may also be written by amending the standard diffusion equation with the appropriate electric field term. This procedure is actually more tedious and works only for a few cases with known expressions describing the involved forces, but it is a standard text book procedure.

B. Segregation of As and P at An Interface of Si

In Si devices processing such as the fabrication of n^+ emitter regions of bipolar transistors, a solid dopant containing material may be used on the Si surface as the diffusion source, or else a dopant may be ion implanted into Si with a solid masking material on its surface to prevent contamination. Segregation of As has been ob-

served to occur at the source-Si interface region.[4] and P diffusion-segregation has been observed between Si and the masking SiO_2 layer, after implanting P and a subsequent annealing.[5] We have satisfactorily fitted these experimental data using the DSE, Figs. 2 and 3. That shown in Fig. 2 is the As result of Schaber et al.[4] of diffusing implanted As from polySi source materials into crystalline Si at 950^oC for 30 min. Afterward As in the polySi region is at a uniform concentration of $\sim 10^{21}$ cm^{-3}, while that in the Si crystal starts at the same value from the polySi-Si interface and decreases with increasing depth. At a narrow interface region, the Si concentration is higher by a factor of a few. Our simulated results fits their results quite satisfactorily, see Fig. 2. The simulation parameters used are: (i) D in polySi is $2.5x10^{-13}$ cm^2/s, D in crystalline Si is $6x10^{-15}+6.42x10^{-16}(n/n_i)$ cm^2/s with $n_i=5.35x10^{18}$ cm^{-3}; (ii) the As solubility in both Si materials is 10^{21} cm^{-3}, while that in a narrow interface region is $4.5x10^{21}cm^{-3}$; (iii) the interface region width δx is 10 nm; (iv) a SIMS profile broadening factor with a full width of 20 nm is further assumed. The parameters used in obtaining this fit are very reasonable. That shown in Fig. 3 is the P diffusion-segregation result of Orlowski and Mader,[5] as cited by Orlowski,[6] after implanting P into Si with an SiO_2 mask and subsequently annealed at 1100^oC for 30 min in an inert ambient. The fitting parameters used include (i) the P diffusivity is $9x10^{-16}$ cm^2/s in SiO_2 and $4.25x10^{-13}$ cm^2/s in Si; and (ii) the P thermal equilibrium concentration is $1.27x10^{21}$ cm^{-3} in Si and $3.1x10^{20}$ in SiO_2; (iii) an assumed 14 nm thick interface region, 8 nm on the Si side and 6 nm on the SiO_2 side; and (iv) the P solubility in the interface region is 1.8 times of that in Si and 7.14 times of that in SiO_2. The parameters used in obtaining this fit are very reasonable, except that the interface region thickness seems to be large, which is probably partly due to the SIMS profile broadening effect which we have not incorporated independently.

C. Hypothetical Cases

The DSE is applicable to all cases involving the segregation phenomena. To demonstrate the capability of the DSE, we have also simulated a number of hypothetical cases. Generally, the problems may be divided into two groups, that possessing stationary (segregation) boundaries and that possessing moving (segregation) boundaries.

1. Stationary boundary problems

Figure 4 shows the simulation results of diffusing a species into a crystal consisting of heterostructure regions wherein the species' solubilities are different. Figure 5 shows that from an initially uniform distribution of the diffusing-segregating species. In these figures, the small oscillations of the profiles do not constitute a reflection of any intrinsic weakness of the DSE, but are due to numerical integration instabilities incurred by the use of a simple computer program written for purpose of demonstrating the solution trend of the DSE. This program uses the explicit method of integration with the advantage of being fast and can be implemented using a desk top computer. We have also obtained solutions using a main frame computer and the general purpose partial differential equation solver package ZOMBIE.[7] These solutions can be free from the presence of the small profile oscillations. We have

presently chosen to present instead the desk top computer simulation results for the purpose of illustrating a mathematical problem risen by the DSE: the diffusion term of the equation imposes one numerical integration stability criterion while the segregation term imposes another. In general, there is only a small integration parameter window allowing to obtain a stable solution for a given problem. This is so even if one uses a main frame computer and some sophisticated partial differential equation solver packages.

2. Moving boundary problems

Generally speaking, diffusion-segregation problems involving moving boundaries are those during crystal growth. To name a few: Si crystal growth from the melt, growth of thermal SiO_2 on Si, recrystallization of amorphous Si, silicide formation on Si, etc. Problems associated with the Si crystal growth from the melt involves also the role of the convection current in the melt, and problems associated with the growth of SiO_2 on Si involves a volume expansion. These problems are too complicated to be simulated presently. In this section we focus on the simulation of the hypothetical cases of impurity diffusion-segregation during amorphous Si recrystallization and during silicidation. The results are shown in Figs. 6 and 7, respectively. To obtain these results, we have assumed that the materials' interface is moving at a constant rate. We have simulated both the 'snowplow' and 'anti-snowplow' cases. Only the snowplow cases are shown. The numerical integration stability problem is more severe for the moving boundary problems and therefore the results shown are those obtained using a main frame computer.

D. Gettering in Si

To improve device fabrication yield, impurity gettering in Si has already become an integral part of the IC processing technology. It is anticipated that this will be true also for the solar cell processing technology in the near future. The gettering technology includes mainly two aspects: (i) the creation of suitable gettering sites or centers; and (ii) the impurity gettering process. In IC processing the useful gettering sites are those of the intrinsic or internal gettering scheme,[8] which are SiO_2 precipitates and their associated defects inside the Si wafer bulk but not at the surface regions where the devices are fabricated. For solar cells, it is envisaged that the *external* gettering schemes should be more useful, although it may also be possible to utilize some internal gettering schemes. The impurity gettering processes themselves are complicated. Generally, it may be divided into the dissolved and precipitated impurity categories. For dissolved impurity atoms, the processes involves the diffusion of the species to the gettering sites and the process of its being stabilized or effectively removed at the gettering sites. For the precipitated impurity cases, the additional process of impurity dissolution from the precipitates into the Si matrix needs to precede its diffusion to the gettering sites.

Up to now there is no simulation effort on the impurity gettering processes. One reason is that only impurity diffusion can be treated quantitatively with confidence. The impurity stabilization or removal process at the gettering sites involves segregation phenomena of one form or another. Now, with the DSE available, we can begin to examine this aspect quantitatively, which is previously not attainable. For this purpose, let us consider the Si wafer backside gettering scheme of using liquid Al as the getterer. An Al-Si liquid alloy forms at a temperature above the system eutectic temperature of $577^{o}C$. Figure 8 presents the simulation result of gettering by a 4 μm thick

liquid Al layer of a fast moving impurity dissolved initially in a 400 μm thick Si wafer. It is seen that, with the simulation parameters used, the impurity concentration (normalized) in Si throughout the wafer thickness dropped by 2 orders of magnitude after a 60 s gettering annealing. For this simulation, the impurity diffusivities in both Si and the Al liquid are set to be 10^{-4} cm^2/s. This is a typical diffusivity value of a species in a liquid, and is also very close to the diffusivity values of the most prominent interstitially dissolved metal contaminant species Cu, Ni, and Fe in Si at high temperatures, e.g., 1000^oC. The solubility of the impurity in the Al liquid is assumed to be 10^4 of that in Si. This is arrived at by considering the fact that the high temperature solubilities of the aforementioned metals are in the order of 10^{16} to 10^{17} cm^{-3}, while the solubilities of these metals in Al is from a few to exceeding 10%, i.e., in the order of 10^{20} to $10^{21}cm^{-3}$. At the Al-Si interface, the ratio of the impurity concentration in Al and in Si is ~10^4, which is the value of the segregation coefficient used in the simulation. We shall say that this stabilization process is due to the *solution-stabilization mechanism.*

There are some salient features associated with this simulation study. First, for the solution-stabilization mechanism the gettering effect is *independent* of the actual impurity concentration in the Si bulk. This is due to the fact that the gettering process is determined by the solubilities of the impurity in the gettered and gettering regions. In steady state, Eq. (11) yields

$$\frac{C_g}{C_{Si}} = \frac{C_g^{eq}}{C_{Si}^{eq}} = k_g , \qquad (14)$$

where the subscripts g and Si refer respectively to the gettering and the gettered (Si) regions. Equation (14) demonstrates that the ratio of actual steady state concentrations C_g and C_{Si} is equal to the segregation coefficient of the two regions but are otherwise independent of the respective thermal equilibrium concentration values. Therefore, C_g and C_{Si} can be any values satisfying Eq. (14). Before reaching the steady state, our simulation results have shown that Eqs. (14) is always approximately satisfied near the region interface shortly after the onset of the annealing. This means that, insofar as a steady state distribution of impurities between the gettering and gettered regions has not yet been reached, the impurities will be gettered irrespective of whether its concentration is at, above, or below its thermal equilibrium values in the gettered regions. This is different from the case for which the impurity must precipitate out at the gettering sites, which shall be said to be due to the *precipitation-stabilization mechanism.* The precipitation-stabilization scheme is effective only if the Si bulk impurity concentration is above its thermal equilibrium concentration.

Second, we can now use this example to define the *ultimate gettering efficiency* for the solution-stabilization mechanism, with the term ultimate meaning that the steady state has been reached in the gettering process:

$$\eta_{ult} = \frac{C_b}{C_a} . \qquad (15)$$

where C_b and C_a are respectively the Si bulk impurity concentrations before and after the gettering run. In this definition, the higher the η_{ult} value, the higher is the gettering efficiency. Let the thicknesses of the gettering region and the Si be respectively x_g and x_{Si}, we have, after gettering,

$$C_g = k_g C_a, \tag{16a}$$

$$x_{Si} C_a + x_g C_g = x_{Si} C_b, \tag{16b}$$

where C_g is the impurity concentration in the gettering region after gettering. C in the gettering region is assumed to be zero or very small before the gettering run. Using Eqs. (15) and (16), we obtain

$$\eta_{ult} = \frac{C_b}{C_a} = \frac{x_{Si} + k_g x_g}{x_{Si}} \approx \frac{k_g x_g}{x_{Si}}, \tag{17}$$

where the last term holds for $k_g x_g >> x_{Si}$. For the case shown in Fig. 8, x_g=4 µm, x_{Si}=400 µm, and $k_g = 10^4$, resulting in η_{ult}=100, just as the simulated result has shown.

The above discussion also points out a difficulty encountered in modeling or simulating the gettering process: not all cases may be treated similarly. To illustrate this point, we mentioned that the definition of η_{ult} is obviously very useful in studying the solution-stabilization mechanism cases. It is unfortunate that this definition may not be useful in other cases. For the precipitation-stabilization mechanism cases, the minimum impurity concentration can be reached in the Si bulk is its thermal equilibrium concentration value at a given temperature, which is itself a very useful quantity. The quantity η_{ult} ceases to be useful because variable values will be obtained, dependent upon the impurity initial concentration in the Si bulk.

As a final comment of this section, we mention that, for a given gettering volume at a given temperature, the solution-stabilized gettering process can be superior than the precipitation-stabilized gettering process, because in the former case gettering will occur even if the impurity concentration is below its thermal equilibrium concentration, while for the latter case the impurity thermal equilibrium value is the limit. However, in technological applications, this does not necessarily mean that the precipitation-stabilized gettering process is inferior, since the gettering volume may be very large, and the gettering process can occur continuously from a high to some very low temperatures, e.g., as for Fe gettering in the intrinsic gettering process.[9]

IV. DISCUSSIONS

A. The Work of Law

In section III.A it has been shown that for charged point defects with thermal equilibrium concentrations given by expressions such as Eq. (12), the DSE, Eq. (9), adopts the form of Eq. (13) which can be written down using a text book procedure. Clearly, one can use Eqs. (12) and (13) to obtain the DSE and the corresponding diffusion-segregation flux equation, Eqs. (9) and (8), respectively, in a *backward* deriva-

tion. Shortly after the derivation of the DSE, we have realized that this may have been accomplished in the past. Indeed, we have subsequently found that, in his Ph. D thesis, Law[10] has used this procedure to obtain

$$J = - DC^{eq} \frac{\partial}{\partial x} \left(\frac{C}{C^{eq}} \right) \quad (18)$$

for a charged point defect species in semiconductors for which C^{eq} takes the form of that given by Eq. (12). Equation (18) is the same as our Eq. (8). Thus, it is clear that Law has already obtained the DSE flux expression sometime ago. However, it seems to be also clear that (i) it was not realized that the equation is the same as the general DSE flux expression; and (ii) its general use as the DSE flux expression will not be warranted, since the derivation is only for a special case, namely that of charged point defects in semiconductors. Comparing Law's work to our own, there is a time honored lesson: a general physical Law can be obtained from that of a special case, if that is the purpose. Or else it might not even be recognized that a general Law has been obtained. A few words about using the *backward* derivation procedure: one needs to be very certain that the thermodynamic quantities used, e.g., for the present case, Eq. (12), are truly proper. Moreover: the general Law so obtained must be justified independently.

B. Other Previous Efforts

Other previous efforts in treating the diffusion-segregation phenomena include that of Ho et al.,[11] Shone et al.,[12] Taylor et al.,[13] and Orlowski.[6] The Ho et al., Shone et al., and Taylor treatment are essentially chemical transport and reaction type first-order kinetic models. These models are successful in describing the experimental data on a case to case basis. However, the models lack generality or predictive capability in general. We will examine the relationship between the present DSE and these models in the near future. Orlowski[6] treated the impurity diffusion-segregation problems *dynamically* using a set of coupled rate equations which contain *absorption* and *emission* coefficients (of the impurity) locally on a microscopic scale. In the absence of the segregation phenomenon, all absorption and emission coefficients are equal and his expressions reduce to the standard diffusion equation. In the presence of the segregation phenomenon, these coefficients are used as adjustable parameters. This model has yielded fits to the As and P diffusion-segregation profiles of Schaber et al.,[4] and Orlowski and Mader,[5] respectively. Our fittings of the same sets of data are shown respectively in Figs. 2 and 3. The relationship between the present DSE and the model of Orlowski[6] will also be examined in the near future. Presently, it suffices to point out again that our formulation of the problem is independent of the kinetics or dynamics involved. These aspects are accounted for by the DSE itself.

C. Outlook of the Diffusion-Segregation Equation

We anticipate that the DSE will be widely used for studies involving the segregation phenomena, in all materials and for all problems. In particular, there is already an enthusiasm of incorporating the DSE in Si processing simulation programs.[13,14] The DSE will also serve to focus experimental efforts and to help unravel, on a quantitative basis, the nature of certain phenomena which may be otherwise difficult to handle. For instance, we can now study the dopant segregation phenomena during silicidation with the objectives of finding out on the one hand the appropriate k val-

ues under the highly dynamic situation involving snowplowing, and on the other also to discover the point defect injection picture associated with the silicidation process.

ACKNOWLEDGMENT

Our work on Si has been supported by National Renewable Energy Laboratory under subcontract XD-2-11004-1, and our work on GaAs has been supported by US army Research Office under contract DAAL03-89-K-0119.

REFERENCES

1. H.-M. You, U. Gösele, and T. Y. Tan, J. Appl. Phys. 74, 2461 (1993).

2. T. Y. Tan, H.-M. You, and U. Gösele, Appl. Phys. A56, 249 (1993).

3. P. Mei, H. W. Yoon, T. Venkatesan, S. A. Schwarz, and J. P. Harbison, Appl. Phys. Lett. 50, 1823 (1987).

4. H. Schaber, R. V. Criegern, and I. Weitzel, J. Appl. Phys. 58, 4036 (1985).

5. M. Orlowski and L. Mader (unpublished. Data Cited in ref. 6 below).

6. M. Orlowski, Appl. Phys. Lett. 55, 1762 (1989).

7. W. Jüngling, P. Pichler, S. Selberherr, E. Guerrero, and H. W. Pötzl, IEEE trans. Electron. Devices ED-32, 156 (1985).

8. T. Y. Tan, E. E. Gardner, and W. K. Tice, Appl. Phys. Lett. 30,175 (1977).

9. D. Gilles, E. I. Webber, and S. Hahn, Phys. Rev. Lett. 64, 196 (1990).

10. M. E. Law, Ph.D. thesis, Stanford Electronics Laboratories, Stanford University (January, 1988).

11. C. P. Ho, J. D. Plummer, S. E. Hansen, and R. Dutton, IEEE Trans. Electron. Devices ED-30, 1438 (1983).

12. F. C. Shone, S. E. Hansen, D. B. Kao, K. C. Saraswat, and J. D. Plummer, IEDM '86 Proceedings, 534 (1986).

13. R. G. Taylor, C. A. Salama, P. Ratnam, and A. Naem, IEDM '88 Proceedings, 644 (1988).

13. M. Orlowski, private communications (1993).

14. P. Griffin, private communications (1993).

FIGURE CAPTIONS

Fig. 1 Simulated transient V_{Ga}^{3-} indiffusion result corresponding to the 700°C (3 h) experiment of Mei et al.,[3] shown to a sample depth of 2 μm. The six higher concentration regions, each 2000 Å wide, are the Si doped n-type regions, and their surrounding 1000 Å wide regions are intrinsic. Dashed lines indicate the V_{Ga}^{3-} thermal equilibrium concentration profile in accordance with the n-values in the appropriate regions.

Fig. 2 The experimental data of Schaber et al.[4] on diffusing implanted As from polySi into the Si substrate, fitted using the DSE. Observe the segregation of As at the polySi-Si interface and the fitting. See text for details on the fitting procedure and parameters.

Fig. 3 The experimental data of Orlowski and Mader[5] on implanted P diffusion-segregation in the SiO_2-Si system, fitted using the DSE. Observe the segregation of P from SiO_2 into Si. See text for details on the fitting procedure and parameters.

Fig. 4 Simulated indiffusion-segregation profiles (in normalized concentrations) of a species into a crystal consisting of heterostructures. That shown in Fig. 1 is an especially complicated case of this category of problems.

Fig. 5 The development of the steady state segregation profile from an initially uniform concentration (normalized) as a function of diffusion time in a heterostructure consisting of two regions. Region 1 is from 0 to 1×10^{-5} cm and region 2 from 1×10^{-5} to 2×10^{-5} cm. The species solubilities in region 2 is 0.3 of that in region 1.

Fig. 6 Simulated hypothetical dopant diffusion-segregation profiles due to amorphous Si recrystallization at a rate v. Initial concentration is uniform, of normalized value 1. The initial interface is at x=0.1 μm. Other parameters are shown in the figure. Region 1 is amorphous Si and region 2 is crystalline Si. Recrystallization proceeds from right to left.

Fig. 7 Simulated hypothetical dopant diffusion-segregation profiles due to silicide growth at a rate v. Initial concentration is uniform, of normalized value 1. Initial interface at x=0 μm. Other parameters are shown in the figure. Region 1 is silicide and region 2 is Si. Silicidation proceeds from left to right.

Fig. 8 Simulated results of gettering a fast moving metallic impurity from the Si bulk using a wafer backside liquid Al layer. Details of the simulation are discussed in the text. Note the high gettering efficiency and gettering rate.

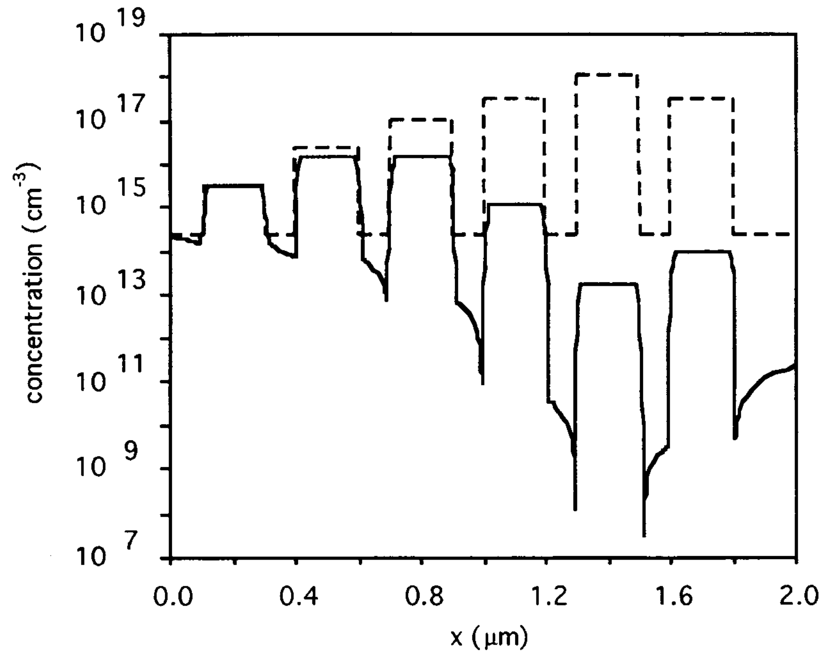

Figure 1

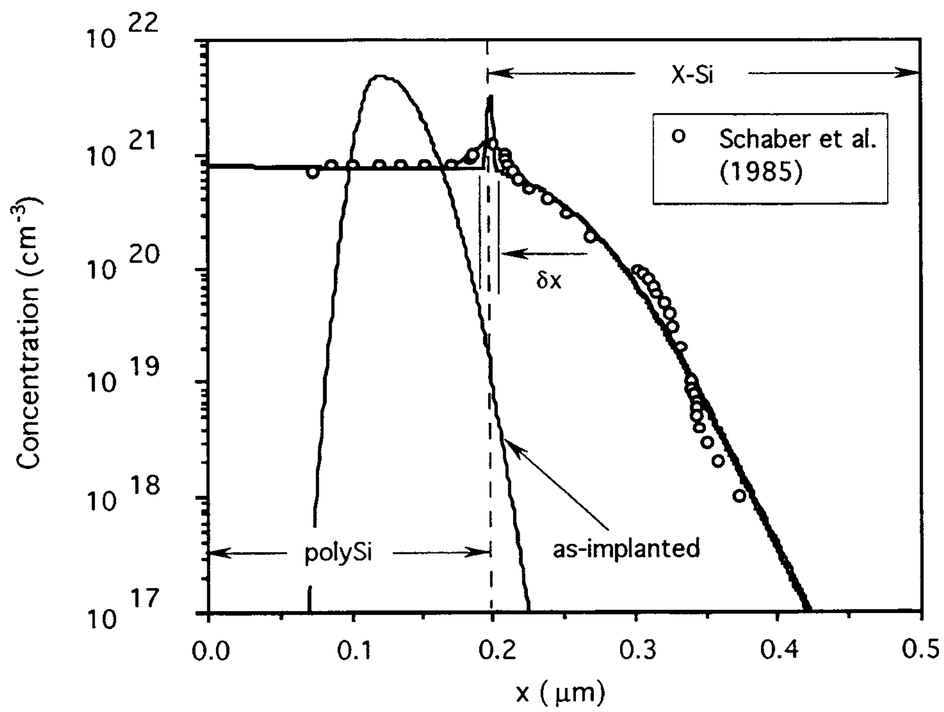

Figure 2

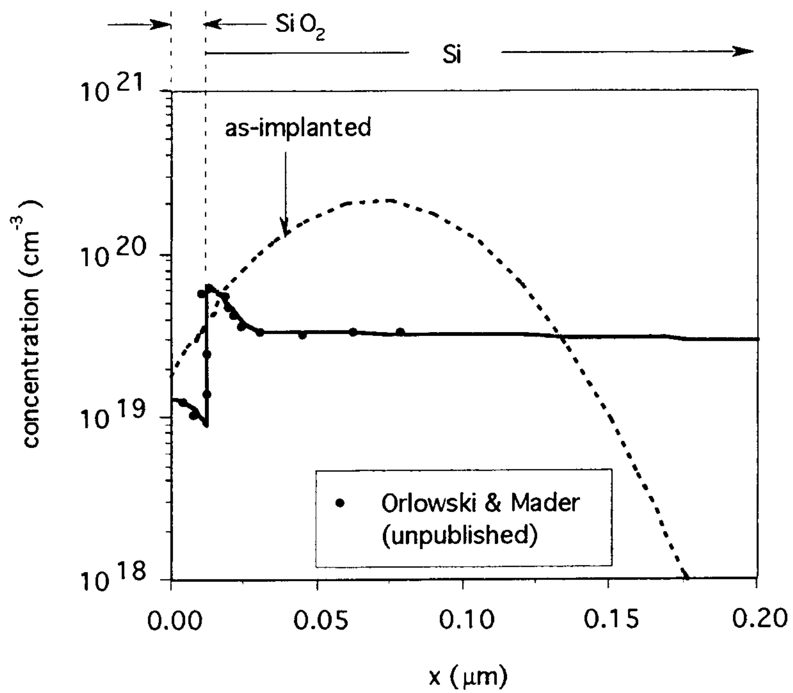

Figure 3

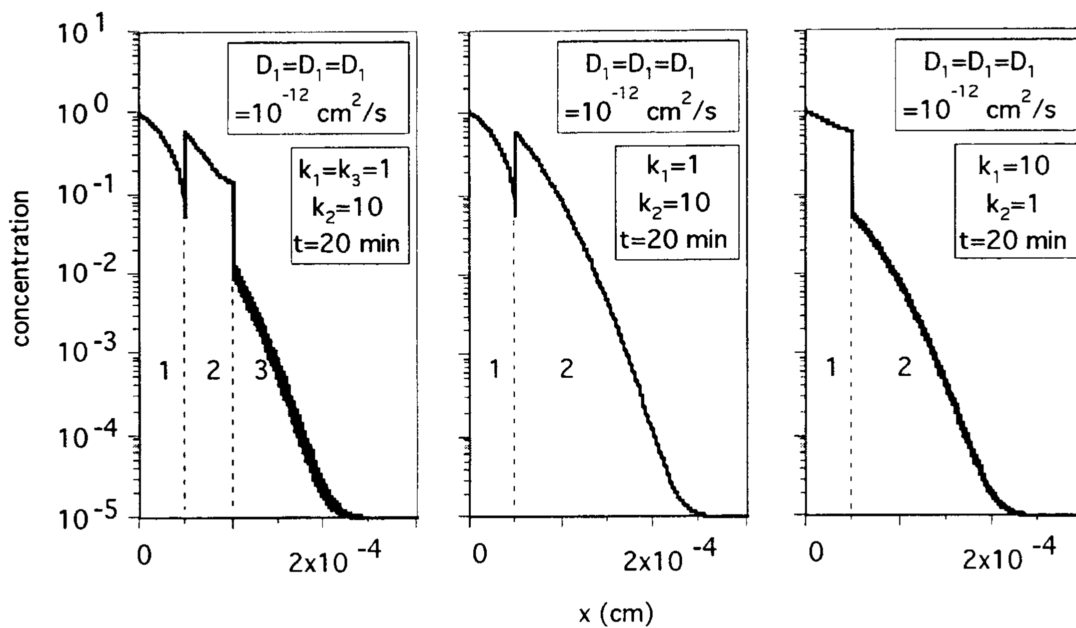

Figure 4

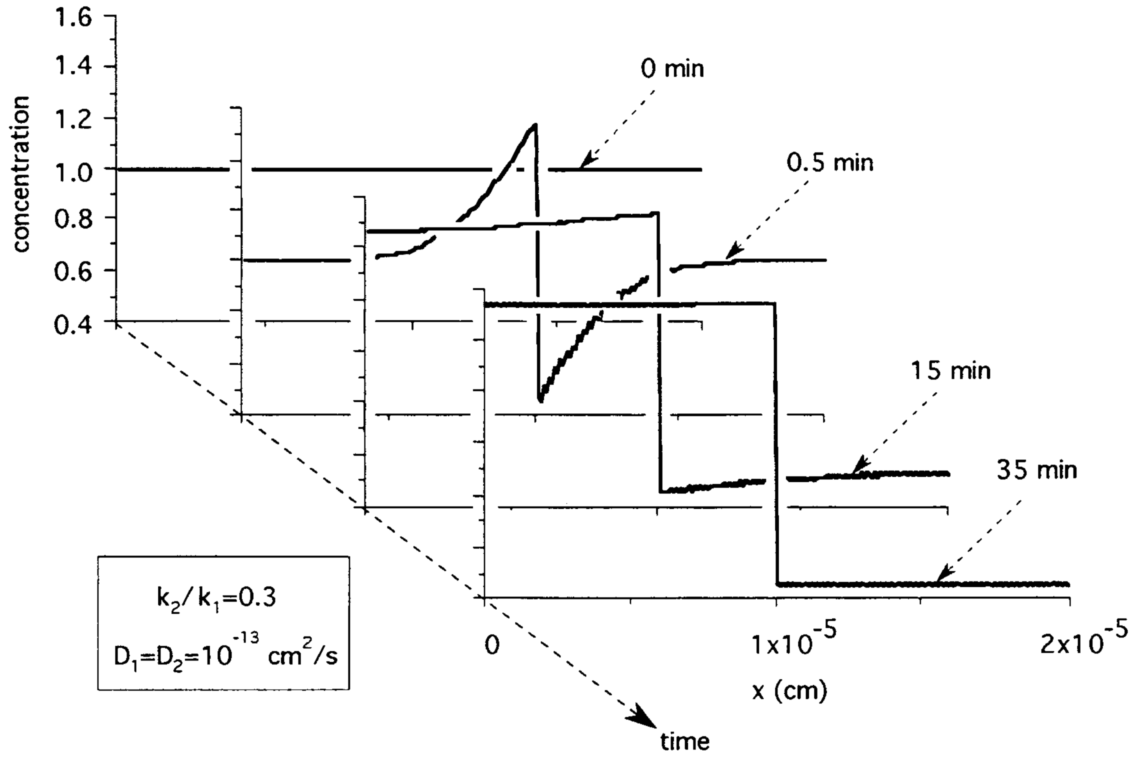

Figure 5

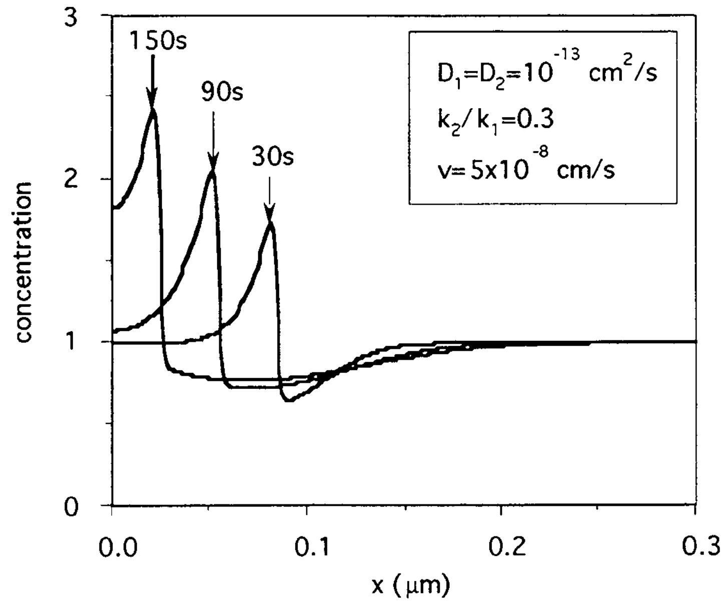

Figure 6

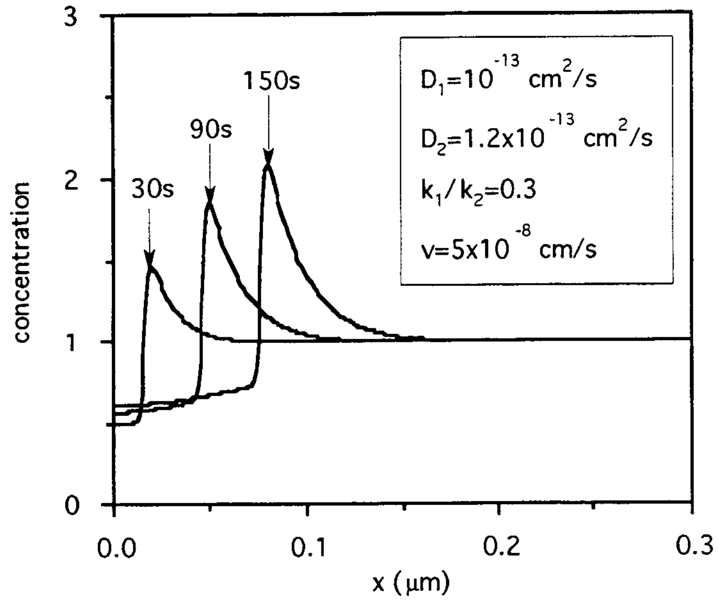

Figure 7

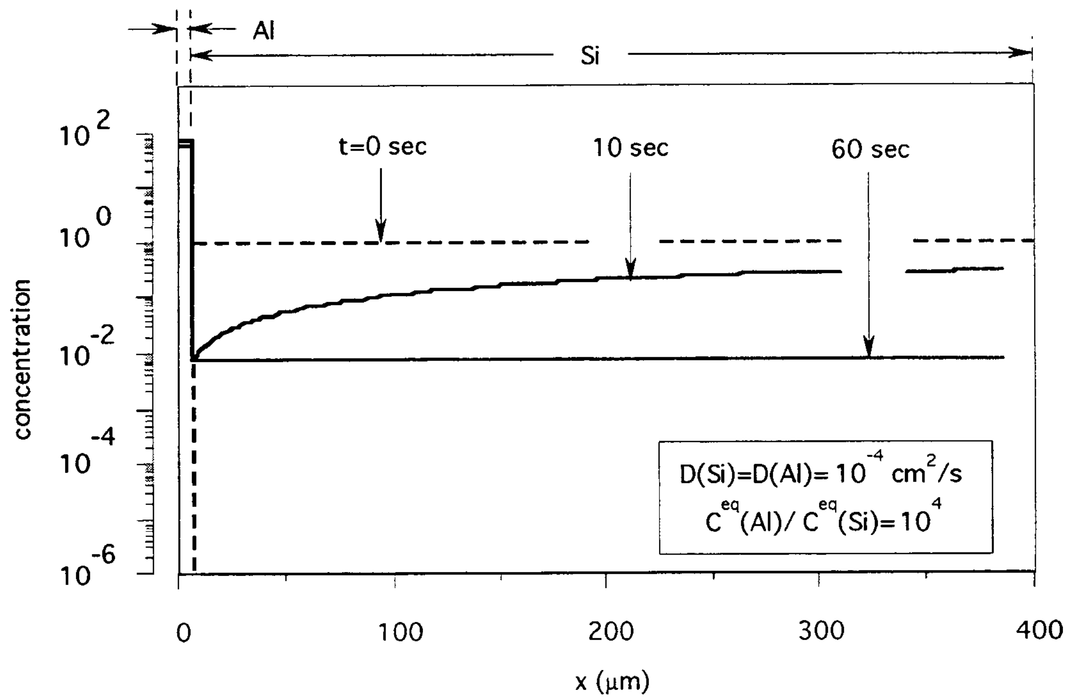

Figure 8

MODIFICATIONS TO THE SOLAREX CASTING PROCESS: EFFECTS ON DEFECTS, IMPURITIES, AND SOLAR CELL PERFORMANCE

By S. Narayanan and T. Tomlinson.
Solarex Corporation, 630 Solarex Court, Frederick, MD 21701 USA
Phone 301 698 4200 / Fax 301 698 4201

ABSTRACT:

Solarex started the commercial production of cast polycrystalline silicon ingots in 1982. At that time about 40% of the ingot was waferable and the average cell efficiency was about 9%. Since then substantial research and developmental efforts have been directed to improve the waferable yield and the electronic quality of the wafers. Many of the improvements achieved by increased control of the casting process have been published. In this paper, the results of another modification, which led to substantial improvement of the wafer quality is discussed.
The modification to the casting station facilitated greater control of the rate of solidification of the molten silicon. The rate of solidification was also varied at certain stages of solidification to improve the throughput and decrease the stress during the casting.

The improved process resulted in substantial increase in the grain sizes of the wafers near the bottom of the ingot and in a significant increase in the yield of high efficiency cells. The effect on the impurity distributions of oxygen and carbon will also be discussed.

INTRODUCTION:

Cast polycrystalline silicon has emerged as a low cost alternative to single crystal silicon as a substrate for solar cells. It has been demonstrated that the performance of the cast polycrystalline solar cell could almost match that of the single crystal silicon solar cell (1). Many companies have developed processes to cast polycrystalline silicon in graphite or ceramics molds. All these processes are based on the directional solidification principle in which the ingot solidifies from the bottom to the top with a certain degree of controlled growth (2,3).

Solarex started the commercial production of cast polycrystalline silicon ingots in 1982. The details of the process improvements and the resultant increase in the yield and the quality of the material are presented in Table 1 (4).

Table 1:

1982	Commercial Production	40% ingot waferable 9% cell efficiencies
1987	Use of high purity ceramics and feed stock (Metallic contamination same as CZ, Large grains)	75% ingot waferable
1991	Optimization of thermal regime	14% increase in the yield of cells > 12.5%
1992	Modification of the casting stations for better control of solidification.	About 80% of cells are above 12.5%

The efficiencies of the solar cells fabricated with Solarex cast polycrystalline silicon wafers are shown in Table 2.

Table 2

Large Area ($130\ cm^2$)	Baseline sequence	13.2%
	Lab sequence	15.1%
Small area ($4\ cm^2$)	Lab sequence	17.2%

Solarex is committed to improving the quality of the substrate by improving the casting process. In this paper, the results of another modification to the casting station, which facilitated greater control of the rate of solidification of the molten silicon, are discussed.

MODIFICATIONS TO THE CASTING PROCESS:

The heater and the insulation package used in the casting stations were modified to facilitate greater control of the solidification rate. This also helped to reduce the premature freezing of the silicon. Multiple solidification rates were used during the casting process to optimize the throughput of the ingots and to reduce the solidification stress.

STRUCTURAL DEFECTS:

This modification to the casting process resulted in a significant increase in the grain size in wafers from the bottom region of the ingot. Figure 1 compares the grain size of the wafers from the bottom region of ingots produced by the old and modified processes. Improvement in the grain size is not as significant for wafers from the top region of the ingot.

(A)

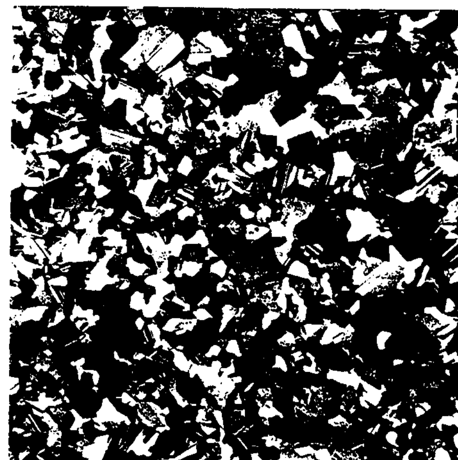

(B)

(C)

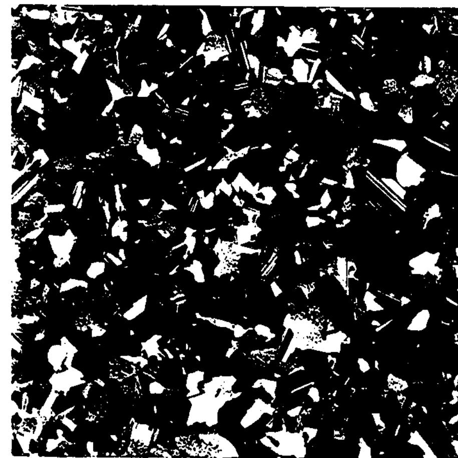

(D)

Figure 1: Comparison of grain size near bottom of ingots. (A) New process 1.6 cm from ingot bottom. (B) Old process 1.6cm. (C) New process 2.4 cm. (D) Old process 2.4 cm. Areas shown are 6 x 6 cm.

IMPURITIES:

Oxygen and carbon are the most prevalent impurities in Solarex cast polycrystalline silicon. The level of metallic impurities in Solarex cast silicon is equivalent or lower than that in single crystal CZ silicon. The low impurity levels in Solarex silicon are achieved by: 1) use of high purity Si feed stock and ceramic crucibles, 2) slower solidification rate of the casting process to take advantage of the segregation coefficients of the impurities.

The oxygen and carbon concentrations of the material obtained by the old and the modified process were measured using FTIR spectroscopy. Figure 2 compares the oxygen and carbon concentration for the two processes. It can be seen from Figure 2 that the modification has resulted in significantly lower oxygen concentration for the material at the bottom region of the ingot.

The concentration of carbon has increased for the material obtained by the modified process. This increase is not detrimental, as cells with high efficiency have been fabricated on material with high carbon content (> 8%) (5).

PERFORMANCE IMPROVEMENT:

The electronic quality of the material from the modified process improved, particularly for the material near the bottom of the ingot. There is a modest improvement in the average solar cell parameters, but there is a significant increase in the distribution of high efficiency cells (>13%) as shown in Table 3.

Table 3.

The increase in the yield of cells >13%:	24%
The increase in the waferable yield: (wafers yielding >12.0% efficient cells)	18%

The improvement in the material quality may be mainly due to the decrease in the amount of silicon prematurely solidified. The stresses generated during the solidification of the ingot are lower due to the decreased solidification rate.

CONCLUSIONS:

There has been a steady improvement of the Solarex casting process since it was first commercialized. The casting process modifications, which have been successfully implemented in all the casting stations, have resulted in a 24% improvement in the yield of high efficiency cells (> 13%).

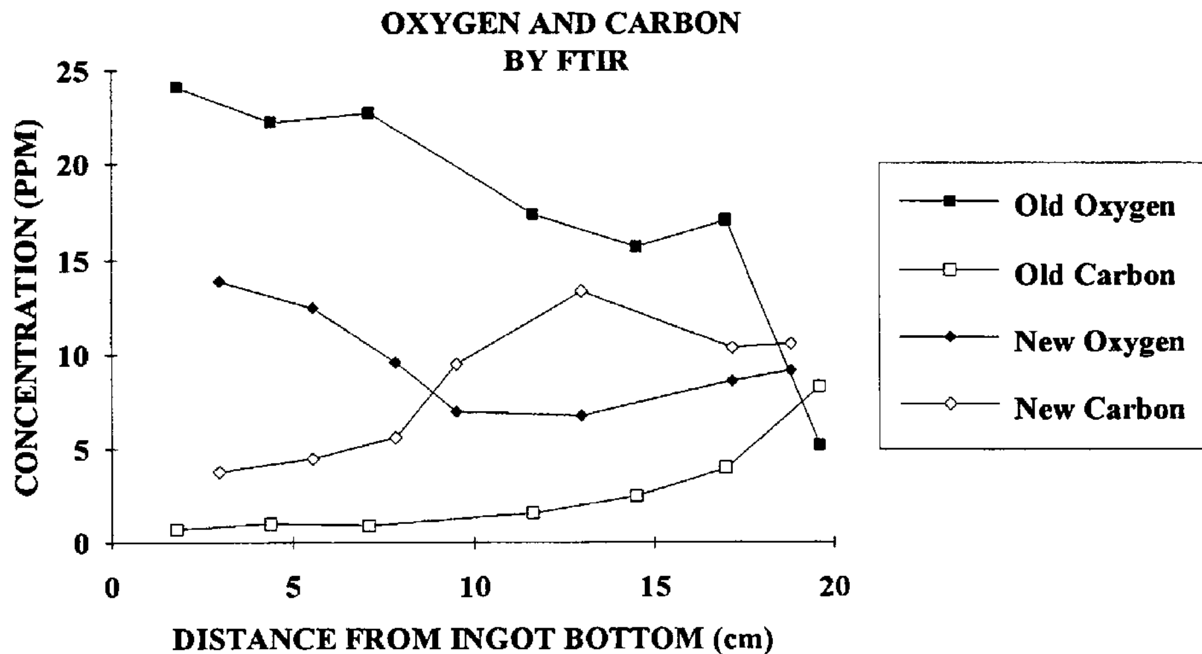

FIGURE 2

ACKNOWLEDGEMENTS:

The authors thank NREL and GIT for performing the FTIR spectroscopy measurements, and James Cliber and other staff at Solarex for their support.

REFERENCES:

1. S. Narayanan, S.R. Wenham, M.A. Green, Proceedings of the 4th PVSEC, Sydney, 1989, page 111.
2. J. Wohlgemuth, R.K. Brenneman, Technical Digest of PVSEC 3, Tokyo, 1987, page 93.
3. R.K.Brenneman, T.A. Tomlinson, Proceedings of the 20th IEEE PVSC, 1988, page 1395.
4. S. Narayanan, J. Terry, R.K. Brenneman, Proceedings of the 10th EC PVSEC, Lisbon, 1991, page 324.
5. W.A. Doolittle, A. Rohatgi, R.K. Brenneman, Proceedings of the 21st IEEE PVSC, 1990, page 681.

THE EFFECT OF RESISTIVITY ON THE MINORITY CARRIER LIFETIME OF CHROMIUM DOPED P-TYPE SILICON

Kamal Mishra
MEMC Electronic Materials, Inc.
St. Peters, MO 63376

The effect of CrB pair dissociation on the minority carrier lifetime in p-type silicon is studied using the surface photovoltage (SPV) and DLTS methods. Experiments were conducted using Cr doped samples ($0.5x10^{12}$-$5x10^{12}$ cm-^{3}) with resistivity ranging from 1 ohmcm to 50 ohmcm. The minority carrier lifetime, increased after the dissociation of CrB by a factor ranging approximately from 2.0 to 10. The resistivity dependence of the minority carrier lifetime in Cr doped samples can be successfully predicted according to the Shockley- Reed- Hall(SRH) model. Lifetime effects of CrB and FeB pair dissociation are compared.

Among fast diffusing metallic impurities in silicon, Fe and Cr are the most effective lifetime killer in p-type silicon. In precipitated form, these metals can cause junction leakage and gate oxide breakdown in sub-micron ULSI technology. Contamination by these impurities may easily occur during various thermal treatments involved in device processing. The identification of metals at a sub-ppb level is possible by techniques such as Deep Level Transient Spectroscopy (DLTS), Electron Paramagnetic Resonance (EPR) and Neutron Activation Analysis(NAA). These techniques are often destructive and require extensive sample preparation. Recently, quantitative identification of Fe in p-type silicon by the surface photovoltage(SPV) technique has emerged as a non-destructive, contactless, fast and sensitive method involving no sample preparation[1-3].

Generally, transition metals such as Fe, Mn and Cr form stable "metal-acceptor" pairs in p-type silicon[4-6]. Since the binding energy estimated from a two point charge coulombic interaction is only 0.5eV, these pairs can be easily dissociated by a low temperature anneal[1,7]. The dissociation behavior of CrB has been previously studied by DLTS[8] in detail. The energy levels at Ec -0.23eV and Ev+0.27 were attributed to Cr_i and CrB related defects. In a preliminary communication, we[9] reported that the minority carrier diffusion lengths of Cr doped p-type samples increased after 200C annealing. In this paper, combined DLTS and SPV measurements

have been carried out to demonstrate that the identification of Cr can be achieved using the minority carrier lifetime measurement. The effect of resistivity on the minority carrier lifetime of Cr doped sample is investigated in detail.

Chromium doped p-type silicon sample were grown by Czochralski method. The resistivity of these samples varied between 1 ohmcm to 50 ohmcm. The concentration of Cr in samples was determined using the DLTS method. For the measurement of the minority carrier lifetime using the SPV method, relatively thick samples (2mm) were used to avoid any thickness limitations offered by the recombination of carriers at the back surface. The oxygen- thermal-donor annihilation was conducted in a clean furnace after cleaning the samples using a HF based process to avoid any contamination. The minority carrier lifetime in these samples was determined using the surface photovoltage (SPV) method. This constant flux method utilizes a very low ($\delta p/p = 10^{-5}$) level of excitation[2]. The instrument uses typically a photon flux below 10^{14} photon/cm^2, and the wavelength varies between 0.8 and 1.02 micron[2]. Schottky barriers of 1.6mm-diameter dots were formed by evaporating Ti. Measurements of electrical properties of deep states were conducted by commercially available digital DLTS system from BIO-RAD, model DL 8010. In this method, the capacitance transient is digitized. The data analysis is based on Deep-Level Transient Fourier Spectroscopy (DLTFS)[10,11]. The dissociation of chromium-boron pairs was achieved by heat treating the samples at 210C for about ten minutes followed by quenching in water. On the other hand for comparison purpose, FeB pairs in selected samples were dissociated by illuminating iron-doped samples using a 250 Watt W-halogen lamp for a period of less than one minute[2].

Earlier Zoth[1] reported a fast and quantitative method of detecting Fe in p-Si using the SPV method. The method is based on the fact that the electron capture coefficient, c_n, for interstitial Fe_i (Ev+0.43eV) is approximately ten times larger than that of FeB pair (Ev +0.1eV). As a result, the minority carrier lifetime in Fe contaminated samples decreases by a factor of ten following the dissociation of FeB pairs. Thus, Fe concentration is determined from the modulation of the minority carrier lifetime by the reversible point defect reaction. In Figure 1a the minority carrier lifetime of Cr doped samples is reported before and after the 210C anneal and quench treatment to dissociate the pairs. Corresponding DLTS spectra for Cr doped sample is reported in Figure 1b. The CrB related peak in the DLTS spectra is seen at 150C. Values of Ev +0.27eV and 2.5x10^{-15}cm^2 for the energy level and the capture-cross-section for holes,

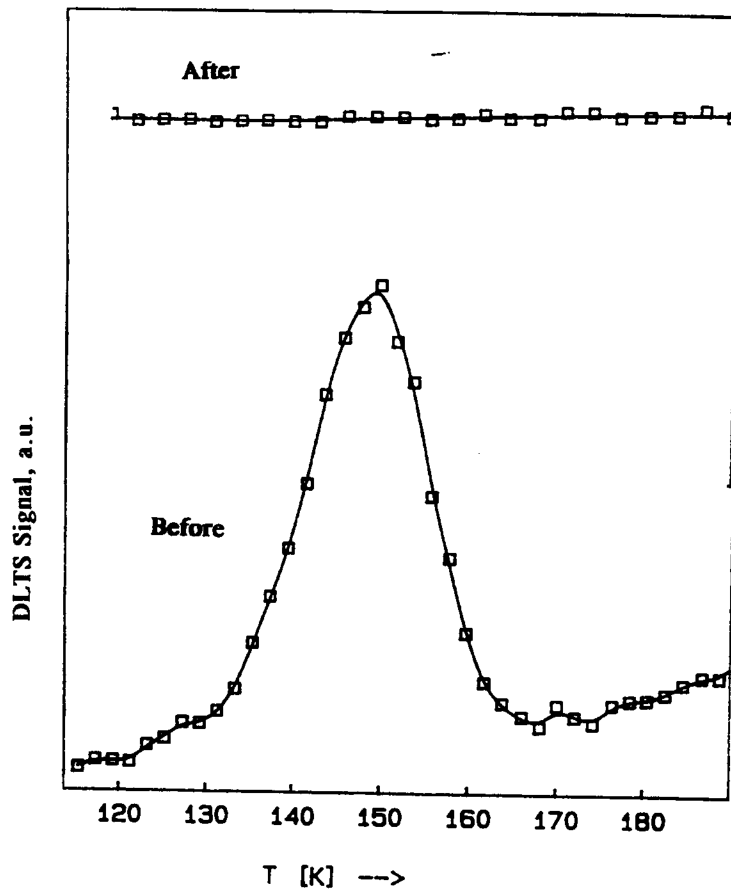

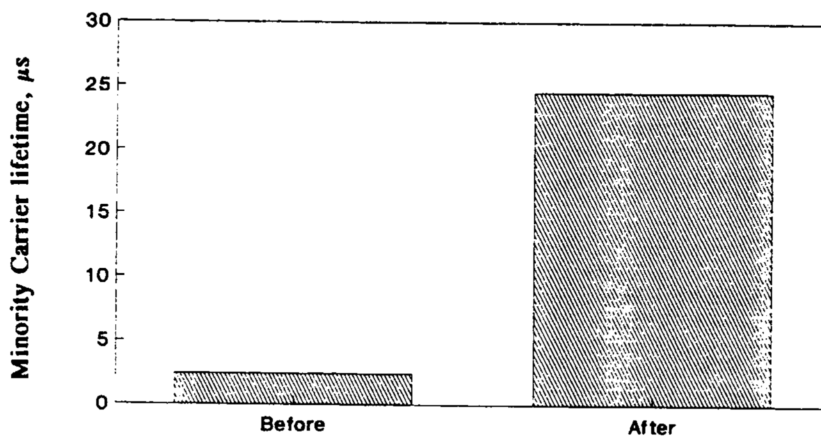

Figure 1. The effect of 200C anneal treatment on the (a) DLTS spectra and corresponding(b) minority carrier lifetime of a Cr doped sample(N_B = 4x10^{14} cm^{-3}, N_{Cr}= 2x10^{12}cm^{-3}).

respectively, determined for the above peak is in good agreement with those reported for CrB in the literature[4]. The peak disappears after the 210C anneal treatment. The energy level of Ec-0.23eV corresponding to the interstitial can be seen in n-type silicon. The data indicate that the minority carrier lifetime in the Cr doped sample increased following the CrB pair dissociation. This behavior is in contrast to that observed in the case of Fe contaminated samples, i.e., an increase in the minority carrier lifetime following the pair dissociation as opposed to the decrease in the minority carrier lifetime in the Fe doped samples following the pair dissociation. It seems that the carrier capture cross-sections for Cr_i and CrB related Shockley- Reed- Hall(SRH) recombination centers differ significantly. The time constant for the pairing process following the thermal dissociation is given by $\tau = 557T/D_{Cr}N_B$ [7] where D_{Cr} is the diffusivity of iron and N_B is the boron concentration. Accordingly, the minority carrier lifetime of Cr doped, 50 ohmcm resistivity, samples continue to decrease with time at room temperature as the pairs are regenerated following the dissociation of pairs(Figure 3). It was noted that the time constant for CrB pair association is approximately thirty times larger than that for the regeneration of FeB pairs[9]. The effect of concentration of Cr related recombination centers, as determined by DLTS, on the inverse of the minority carrier lifetime is presented in Figure 2. A linear relationship shown in the figure indicates that the minority carrier lifetime is indeed dominated only by Cr related recombination center. To determine the effect of resistivity on the minority carrier lifetime of these Cr doped samples, measurements were conducted on samples with resistivity ranging from 1 ohmcm to 50 ohmcm. Minority carrier lifetime measurements were made before and after the 210C anneal treatment to obtain lifetime values dominated by CrB and Cr_i defects respectively. The concentration of Cr in these samples was $0.5x10^{12}$ cm^{-3}. The results are shown in Figure 4. The minority carrier lifetime, in general, decreased with the decrease in the resistivity. Further, the minority carrier lifetime of 50 ohmcm samples increased by a factor of 9-10 following the dissociation of CrB pairs whereas the values increaesd only by a factor of two in samples with resistivity of 1 ohmcm.

The lifetime for p-type silicon under low injection conditions can be modeled to the following Shockley-Read-Hall(SRH) equation[12]:

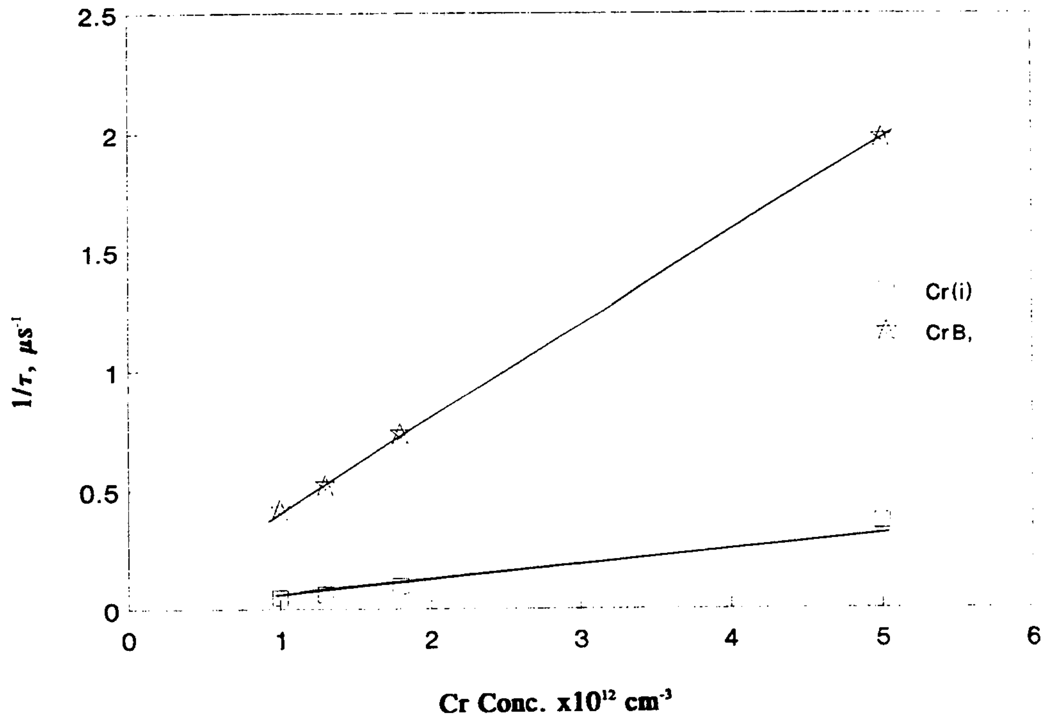

Figure 2. The effect of Cr concentration on the minority carrier lifetime before and after the 200 anneal treatment($N_B=4x10^{14}cm^{-3}$).

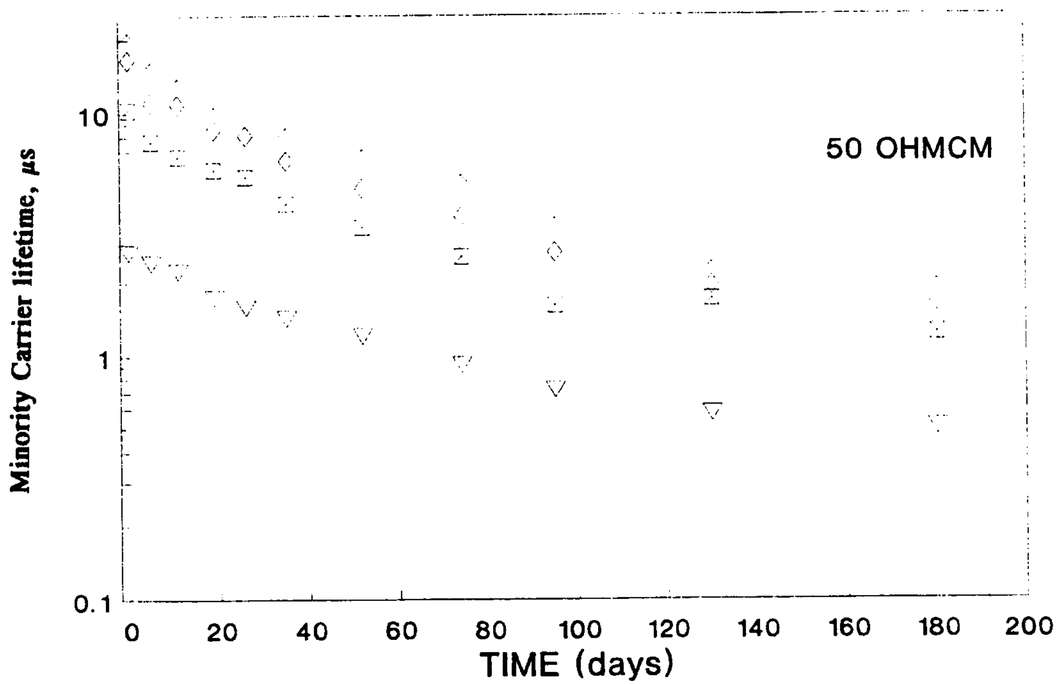

Figure 3. The effect of CrB pair regeneration on the minority carrier diffusion length following the pair dissociation($NB=4x10^{14}cm^{-3}$).

$$\tau = \frac{\tau_{po} \times (n_0 + n_1) + \tau_{no} \times (p_0 + p_1)}{n_0 + p_0} \quad (1)$$

with,

$n_1 = N_C \exp[(E_T - E_C)/kT]$ (2)

$p_1 = N_V \exp[(E_V - E_T)/kT]$ (3)

$\tau_{p0} = 1/(\sigma_p v_{th} N_T)$ (4)

$\tau_{n0} = 1/(\sigma_n v_{th} N_T)$ (5)

where $n_0(p_0)$ is the density of electrons(holes) in equilibrium, v_{th} is the average thermal velocity, $\sigma_n(\sigma_p)$ is the capture cross-section of electrons(holes), N_T is the bulk concentration of recombination centers, $N_C(N_V)$ is the effective density of states in the conduction(valence band), and $E_C(E_V)$ is the conduction(valence) band edge.

In case of CrB ($E_T = E_V + 0.28eV$) and $Cr_i(E_T = E_C - 0.23eV)$ in p-type silicon, Eq. 1 reduces to following Eqs. 6 and 7 respectively:

$\tau_{CrB} = \tau_{n0}(1 + p_1/p_0)$ (6)

$\tau_{Cr} = \tau_{n0} + \tau_{p0}(n_1/p_0)$ (7)

Solid and doted lines in Figure 4 are plotted according to Eqs. 6 and 7 corresponding to the CrB and Cr_i related minority carrier lifetime. The resistivity dependence of the minority carrier lifetime can be successfully explained on the basis of the SRH model. This confirms that the levels, $E_V + 0.27eV$ and $E_C - 0.23eV$, indeed are the recombination centers for CrB and Cr_i , respectively determining the recombination lifetime. A fit of Eqs. 6 and 7 to the exeprimental data yield values of $1.5 \times 10^{-6} cm^{-3} s^{-1}$ and $2.5 \times 10^{-6} cm^{-3} s^{-1}$ for the electron capture coefficients($C_n = \sigma_n v_{th}$) for CrB and the hole capture coefficient for $Cr_i(C_p = \sigma_p v_{th})$ respectively.

It is well established that FeB pairs dissociate under strong illumination due to the recombination-enhanced dissociation[7]. Upon strong illumination at the room temperature, the CrB peak amplitude in the DLTS spectra as well the minority carrier lifetime remain unchanged. It seems that in the case of CrB, the electronic energy released following the electron capture is less efficiently converted into the local vibrational energy. Further more the value of 0.85eV of energy released following the electron capture by CrB defect is smaller than the value of 1 eV liberated following the electron capture by FeB(0.1eV) defect. This facilitates selective

identification of Fe in the presence of Cr.

In summary, it has been shown that the SPV method of determining low injection level lifetime can be used to detect Cr in p-type silicon. The increase in the minority carrier lifetime following the pair dissociation is caused by the fact that the CrB is approximately 2-10 times, depending upon the resistivity, more effective as a recombination center than Cr_i. The increase in the lifetime corresponding to the pair dissociation takes place after thermal dissociative process. Dissociation of CrB, unlike FeB, was not observed in the presence of strong illumination at room temperature.

The author would like to thank Walter Huber, Jerry Moody, Bob Falster and Dale Hill for many helpful discussions during the course of this study.

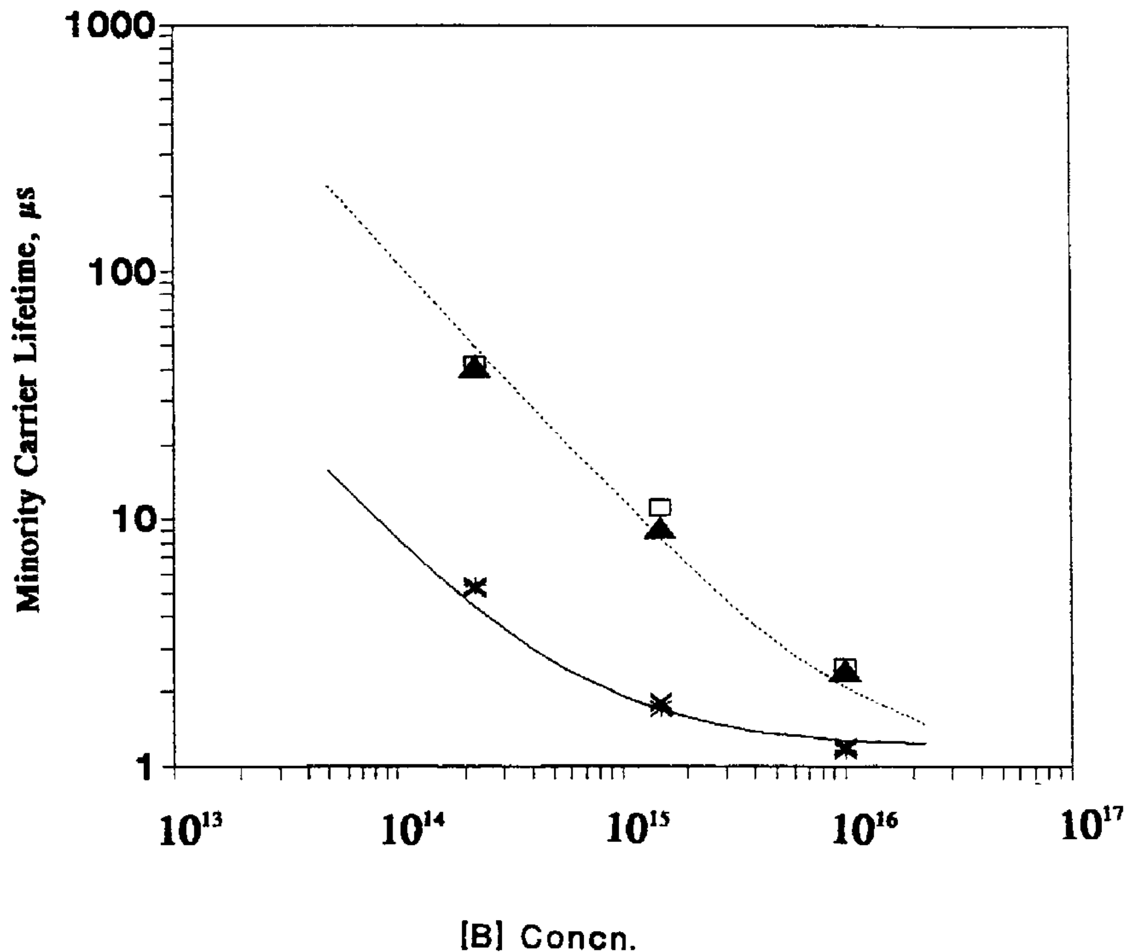

Figure 4. The effect of acceptor concentration on CrB and Cr_i controlled minority carrier lifetime.

REFERENCES:

1. G. Zoth and W. Bergholz, J. Appl. Phys 67,6764(1990).
2. J. Lagowski, P. Edelman, A. M. Kontkiewicz, O. Milic, W. Henley, M. Dexter, L. Jastrezebski, and A. M. Hoff, Appl. Phy. Lett. 63, 3043(1993)
3. J. Lagowski, P.Edelman, M. Dexter, and W. Henley, Semicond. Sci. Technol. 7, A185(1992).
4. H. Conzelmann, K. Graff ad E. R. Weber, Appl. Phys. A, 30, 169 (1983).
5. E. R. Weber, Appl. Phys. A30, 1(1983).
6. H. Lemke, Phys. Status Solodi A 64, 215 (1981).
7. L. C. Kimerling and J.L. Benton, Physica B 116, 297(1983).
8. J. Zhu, J. Diz, D. Barbier and A. Laugier, Mat. Sci. Engg.B4,184(1989).
9. K. Mishra, Electrochem. Soc. Proc. 92-2, extended Abstracts 426, October 1992, Toronto, Canada.
10. S. Weiss, R. Kassing, Solid State Electron. 31, 1733(1988).
11. S. Weiss, R. Beckmann, and R. Kassing, Appl. Phys. A 50, 151(1990).
12. W. Shockley and W. T. Read, Phy. Rev. 87(1952)835.

The Structural, Chemical, and Electrical Properties of He-Implantation-Induced Nanocavities in Silicon

C. H. Seager, S.M. Myers, D. M. Follstaedt, H. J. Stein, and W.R. Wampler
Sandia National Laboratories, Albuquerque, N. M. , 87185

Si implanted with He to doses of about 2×10^{16} cm^{-2} and greater and annealed at high temperatures develops a layer of internal nanocavities near the end of the He range. Above an annealing temperature of 700°C, all the implanted He escapes from these implanted samples, and the resultant internal cavity surfaces can be shown to possess a high density of chemically reactive Si dangling orbitals. These structures, in addition to possessing a variety of interesting electronic properties, have recently been shown to hold great promise as getters for removing undesirable impurities from the silicon matrix. Here we describe some of the structural features of these nanocavities and studies which have been used to accurately determine the binding energy of H and Cu to Si atoms at the cavity walls. Recently, we have also demonstrated that these nanocavities capture large densities of majority carriers in n- and p-type silicon. These electrical measurements have demonstrated that the nanocavity electronic states possess both acceptor and donor levels in the Si forbidden gap. The approximate location of these levels has been determined by a variety of different types of capacitance transient spectroscopy.

I. Introduction

It has been recognized for some time that ion implantation of He into Si produces bubbles, and that subsequent annealing at temperatures above 700°C causes the He to diffuse out of the material leaving voids[1]. The empty cavities form a well-defined layer at a depth of about 0.3 μm as seen in the TEM micrograph in Figure 1. Typical cavity size for this implantation and annealing condition is ~ 20 nm, and distinct facetting of the cavity walls can be seen. The walls of these nanocavities are believed to be pristine surfaces, and several of their properties will be discussed in this paper. The dissociation energy of the Si–H surface bond, which has proved inaccessible to ultra-high-vacuum experiments on external Si surfaces, will be accurately determined[2-4], and the transition-metal solute Cu will also be shown to be strongly trapped by these internal surfaces[5]. These results raise the possibility of using cavities for impurity gettering in Si devices. We will also review some recent measurements of the electrical properties of these structures. These latest studies were intended to complement previous UHV photoemission data on external silicon surfaces. Additionally, we sought to determine the effects of cavity-containing layers on the electrical properties of doped Si to facilitate the exploitation these layers in devices for such purposes as impurity gettering.

II. H and Cu -Cavity Interactions

Extensive experimentation has been done at Sandia Laboratories to determine the binding energy of H at internal nanocavity surfaces[2-4]. Figure 2 illustrates that this binding energy is not directly deducible from UHV desorption of H on external cavity surfaces because, although the final state of such a process involves only H-H and H-Si bond energies, the desorption activation energy depends on the energy of a poorly understood intermediate state. This obstacle can be overcome by two separate types of nanocavity-based measurements. In the first Nuclear Reaction Analysis (NRA) was used

to study the equilibrium amount of bonded H at cavity walls at pressures around 1 atm. In a UHV situation such pressures would produce unavoidable contamination of the external surface. In the nanocavity study, however, the surrounding silicon matrix prevents contamination of the nanocavity walls. This measurement yields a value for the Si-H bond energy, E_B of 2.6 ±0.1 eV. The second study of this type involves monitoring the thermal release of H from the nanocavity walls into solution in the silicon lattice, also using NRA. The rate limiting step in this reaction is the promotion of atomic H from internal chemisorption to solution, and the measured rate yielded $E_B = 2.5 \pm 0.2$ eV in excellent agreement with the gas equilibration studies. As a byproduct of these measurements, we were able to use prior UHV desorption results for the desorption activation energy, $E_D \approx$ 2.5 eV, together with our result for E_B, in the equation given in Figure 2 to deduce that the H_2 adsorption activation energy is about 1.8 eV. We also note that FTIR data obtained in conjunction with these experiments[2,4] confirmed the presence of Si-H bonds on the nanocavity surfaces.

Similar experimental techniques were used to estimate the binding energy of Cu on internal cavity surfaces and to compare this with the heat of solution from precipitates of the Cu_3Si phase[5]. The heat of solution for the silicide was obtained by forming Cu_3Si in a near surface layer of a silicon wafer and then observing the transfer of Cu from the silicide to a different layer containing the stronger cavity sinks during annealing. The central idea of these experiments is that the redistribution rate of the Cu is controlled by its solubility in equilibrium with the silicide and by th Cu diffusion coefficient, and the diffusion coefficient can be taken from the literature. This allows the solubility to be determined from the experimental data. The temperature dependence of the solubility then yields the heat of solution.

The Cu_3Si was formed by Cu ion implantation and annealing, and its presence was verified by transmission diffraction. The cavity sinks were located either on the same side of the wafer, at a distance of 0.6 μm from the silicide, or on the opposite side at a distance

of 250 μm. The shorter of these two diffusion distances facilitated measurements at the relatively low temperature of 450°C, while migration over the greater distance was observed at 600°C. The migration of Cu was observed by Rutherford backscattering analysis (RBS), and the accumulation in the cavity sinks is shown as a function of time in Fig. 3. The lines through the data are theoretical fits yielding the heat of solution. The result is 1.7 eV, in good agreement with the published phase diagram.

The binding energy for Cu in the cavities was determined in a very analogous fashion by observing the redistribution of Cu between two cavity layers, one fully occupied initially and the other initially containing no Cu, that were seperated by ~0.4 μm. Under this condition the redistribution proceeds until the fractional occupancies of trap sites are the same in the two layers, and the redistribution rate is governed by the trap binding energy together with the Cu diffusivity. The areal density of redistributed Cu is plotted in Fig. 4 as a function of time at two temperatures, 650 and 700 °C. The curves through the data represent theoretical fits yielding the trap binding energy, 2.2 ±0.2 eV relative to Cu in solution. Thus, nanocavities provide a sink for Cu that is ~0.5 eV stronger than silicide formation.

III Electrical Properties

We anticipate that the dangling Si orbitals on internal cavity surfaces will possess positive, neutral, and negative charge states corresponding to occupation by 0, 1 or 2 electrons. Such states have been seen on clean external Si surfaces[6], Si/SiO_2 interfaces[7-9], grain boundaries[10], and dislocations[11]. Because such ambipolar localized states tend to capture majority carriers, one might anticipate that the resulting charge accumulations will lead to bandbending in the cavity regions which will repel majority carriers at equilibrium. A schematic of the expected charge trapping is shown for n-type Si in Figure 5. A readily identifiable signature of such structures is the substantial impedance they

offer to majority carrier current flow. We have prepared n- and p-type Si wafers with 300 keV He implants and both ohmic and Schottky barrier contacts to look for charging effects of this type[12].

Figures 6 and 7 show the measured zero-bias conductance versus inverse temperature for ohmically contacted samples of this type. In these measurements we forced current to cross the sub-surface nanocavity layer by applying a small potential difference across the front and back ohmic contacts. We see that there is indeed substantial impedance caused by the nanocavity layers, and at least at high temperatures, a temperature dependence consistent with thermionic emission of majority carriers. The expected dependence for the zero-bias conductance under these situations is given by[13]:

$$G = (A^{*}Te/k^{2})\exp((\phi_{B}+\zeta)/kT) \quad , \qquad (1)$$

where ϕ_B is the electrostatic band bending at the top of the nanocavity-associated electrostatic barrier, ζ is the energy difference between the Fermi level and the conduction band bottom, A^* is the Richardson constant, e is the elecronic charge, T is the absolute temperature, and k is the Boltzmann constant. We believe that the weaker temperature dependence seen below ~270K is due to current crossing occasional low spots in the potential barriers which result from the statistical nature of the cavity distribution. High frequency capacitance measurements on these same samples were interpreted to yield the width of the depleted region around the nanocavities using[13]:

$$C_{hf} = A\,\varepsilon/w \quad , \qquad (2)$$

where A is the sample area, ε is the dielectric constant of silicon (1.06×10^{-12} f/cm), and w is a measure of the depletion width surrounding the nanocavities. Figures 8 and 9 show the values of w deduced from our experimental data using Equation 2. We note that the

depletion region around the cavities is of the order of, but somewhat wider than, the nanocavity layer itself.

In addition to these probes of the equilibrium bandstructure around the nanocavities, we also performed transient capacitance measurements on a number of nanocavity samples with ohmic and Schottky contacts. Figure 10 shows the results for electron emission from the upper dangling bond (doubly occupied) level, and Figure 11 shows emission data for holes excited from both localized state levels. These measurements indicate that the upper dangling bond level lies ~ 0.37 eV below the conduction band minimum, and the lower level is ~ 0.17 above the valence band maximum. Using these energy level positions we have simulated the cavity charging with a simple picture in which we allow at most one electron or hole to occupy each cavity, and many of the experimental features that we see can be understood in a semi-quantitative fashion with this approach[12].

IV. Conclusions

Various studies of the chemical and electronic properties of He-implantation-induced nanocavites have been carried out. These structures are extremely chemically reactive and can bind H and transition metal impurities at temperatures above 600°C. For this reason they may provide an attractive alternative to conventional gettering methods in situations where the additional expense of ion implantation can be tolerated. In addition to their unique chemical properties, nanocavities are strong traps for electronic charge and have a profound influence on the nearby Si bandstructure and electronic transport of majority and minority carriers.

References

1. C. C. Griffioen, J. H. Evans, P. C. De Jong, and A. Van Veen, Nucl. Instrum. Meth. B **27**, 417 (1987).
2. S. M. Myers, D. M. Follstaedt, H. J. Stein, and W. R. Wampler, Phys. Rev. B **47**, 13380 (1993).
3. W. R. Wampler, S. M. Myers, and D. M. Follstaedt, Phys. Rev. B **48**, 4492 (1993).
4. H. J. Stein, S. M. Myers, and D. M. Follstaedt, J. Appl. Phys. **73**, 2755 (1993).
5. S. M. Myers, D. M. Follstaedt, and D. M. Bishop, Proc. 17th Inter. Conf. on Defects in Semiconductors, Gmunden, Austria, July 18-23,1993, in press.
6. F. J. Himpsel, Surf. Sci. Reports **12**, 1, (1990).
7. P. J. Caplan, E. H. Poindexter, B. E. Deal, and R. R. Razouk, J. Appl. Phys. **50**, 5487 (1979).
8. E. H. Poindexter, P. J. Caplan, B. E. Deal, and R.R. Razouk, J. Appl. Phys. **52**, 879 (1981).
9. P. M. Lenahan and P. V. Dressendorfer, Appl. Phys. Lett.**41**, 542 (1982).
10. See for example, C. H. Seager, E. L. Venturini, and W. K. Schubert, J. Appl. Phys. **71**, 5059 (1992).
11. V.V. Kveder, A. E. Koshelev, T. R. Mchedlidze, Y. A. Osipyan, and A. Shalynin, Zh. Espk. Teor. Fiz. **95**, 183 (1989).
12. C. H. Seager, S. M. Myers, R. A. Anderson, W. L. Warren, and D. M. Follstaedt, submitted to the Physical Review.
13. W.E. Taylor, N. H. Odell, and H. Y. Fan, Phys. Rev. **88**, 867 (1952).

Figure Captions

Figure 1. <110> cross-sectional TEM micrograph of a silicon sample which has been implanted with 1×10^{17} He/ cm^2 at 30 keV followed by a 900°C ,1 hr. vacuum anneal. Clear evidence of facetting is seen.

Figure 2. A schematic energy diagram for the reaction path between H chemisorbed on silicon and H_2 in vacuum.

Figure 3. The accumulation of Cu at nanocavities, resulting in dissolution of Cu_3Si, as a function of anneal time. Open circles are for an experiment where the cavities were on the opposite side of the wafer from the silicide layer, while the filled circles are data from an experiment where the silicide was on the same side of the wafer as the nanocavities. Theoretical fits are shown as solid lines.

Figure 4. The areal density of Cu transferred from an initially saturated cavity layer to an initially empty cavity layer as a function of anneal time at two temperatures. Solid lines are theory fits using a Cu-cavity binding energy of 2.2 eV.

Figure 5. A schematic representation of the expected bandbending produced by the trapping of electrons at cavity layers in n-type silicon.

Figure 6. Conductance divided by absolute temperature versus inverse temperature for an ohmically contacted n-type Si sample containing a buried layer of He implantation-produced nanocavities. The sample electrode area was 11.6 mm^2.

Figure 7. Conductance divided by absolute temperature versus inverse temperature for an ohmically contacted p-type Si sample containing a buried layer of He implantation-produced nanocavities. The sample electrode area was 11.6 mm^2.

Figure 8. The depletion layer width deduced from 1 MHz capacitance at zero dc bias for an ohmically contacted n-type Si sample containing a buried layer of He implantation-produced nanocavities. The sample electrode area was 11.6 mm^2.

Figure 9. The depletion layer width deduced from 1 MHz capacitance at zero dc bias for a ohmically contacted p-type Si sample containing a buried layer of He implantation-produced nanocavities. The sample electrode area was 11.6 mm^2.

Figure 10. The measured electron emission rate divided by absolute temperature squared deduced from 1 MHz capacitance transients on n-type ohmically contacted Si samples. Filled circles are for data obtained after +1 to 0 volt transitions; Filled squares are for data obtained after -1 to 0 volt transitions. The origin of the lower energy emission process is uncertain, but it is thought to involve emission from P donors located near or on nanocavity surfaces.

Figure 11. Measured hole emission rates divided by absolute temperature squared for ohmically contacted and Schottky barrier p-type samples. The filled circles are deduced from DLTS measurements on Schottky barrier samples, and the open circles are from capacitance relaxation transients measured after majority carrier injection pulses on ohmically contacted samples.

(001)
Si
0
0.1 μm
0.2
0.3
0.4

H ENERGETICS ON Si SURFACE

$$E_D = 2\,E_B - E_R + E_A$$

E_D = DESORB ACTIVATION E.
E_B = Si-H BOND ENERGY
E_R = H-H BOND ENERGY
E_A = ADSORB ACTIVATION E.

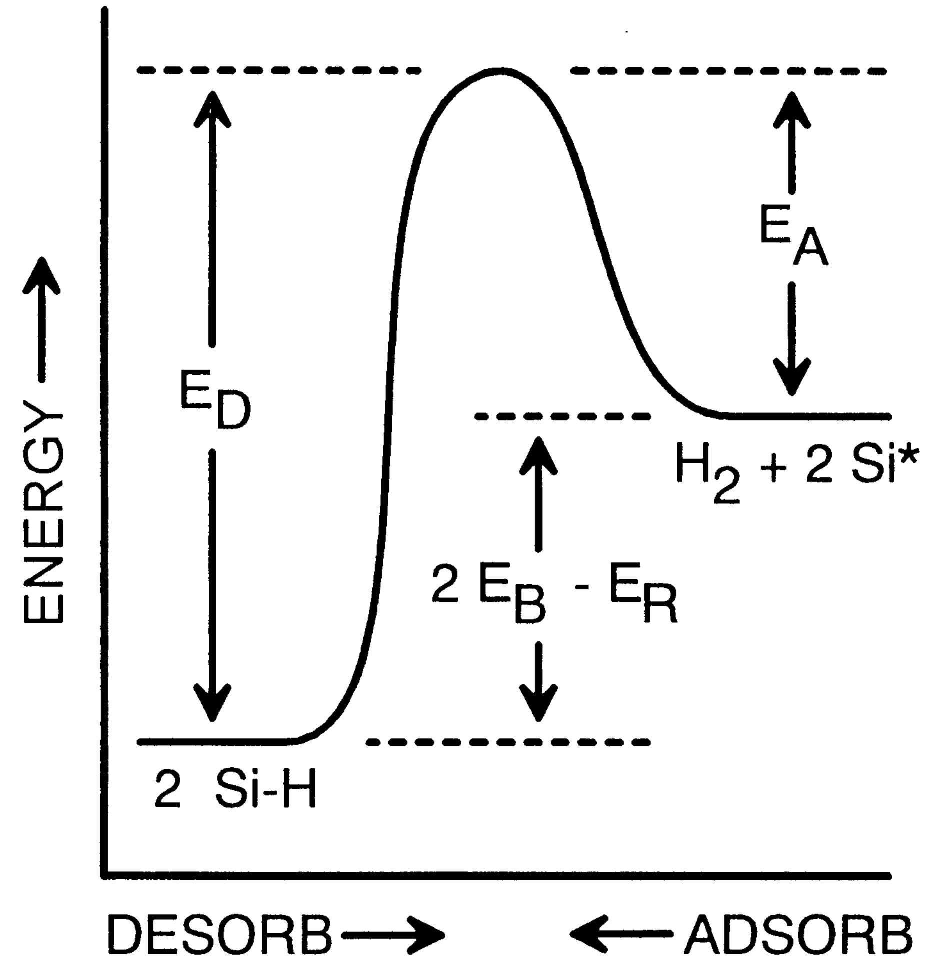

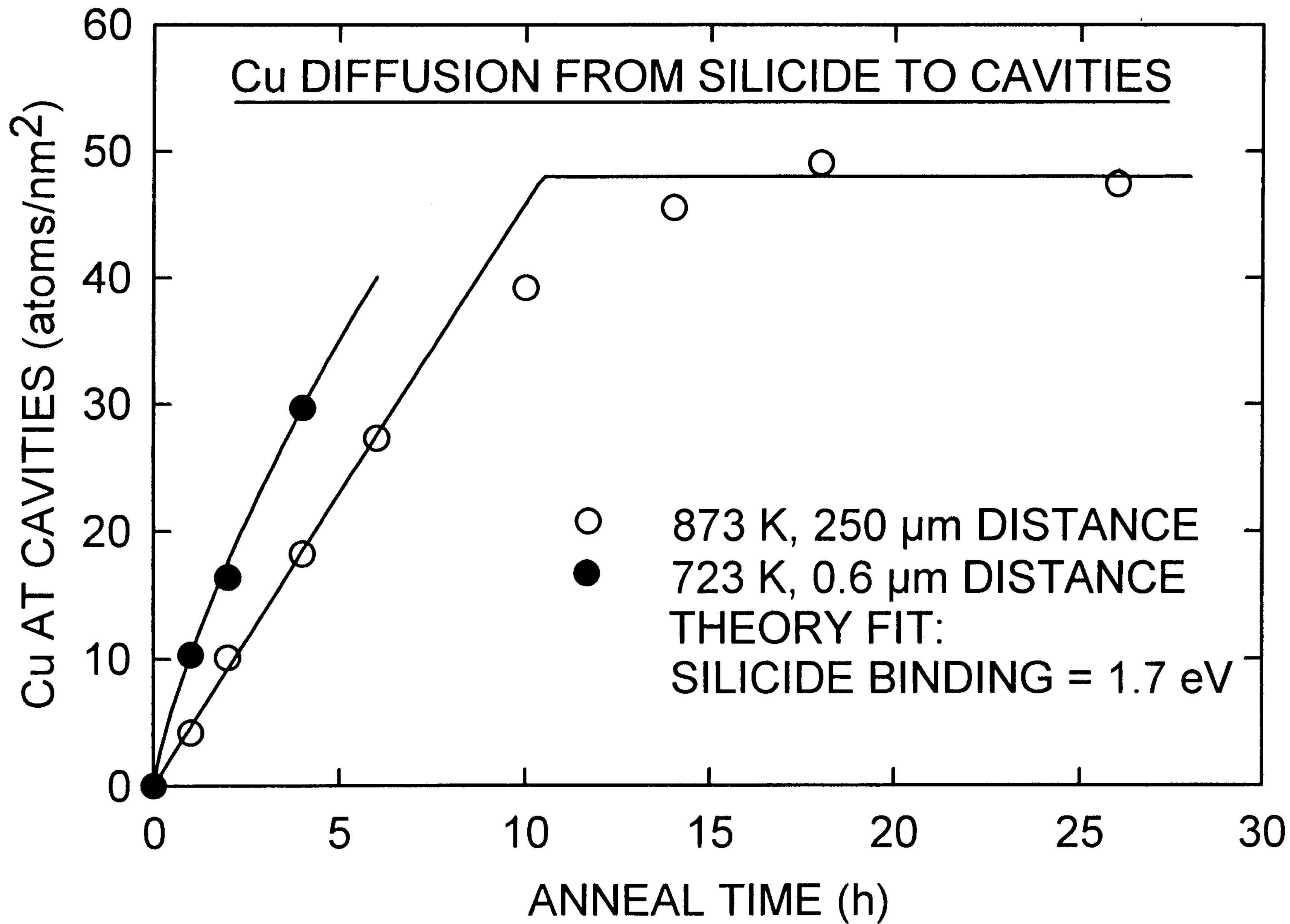
Cu DIFFUSION FROM SILICIDE TO CAVITIES
Cu AT CAVITIES (atoms/nm2)
60
50
40
30
20
10
0
0
5
10
15
20
25
30
ANNEAL TIME (h)
873 K, 250 µm DISTANCE
723 K, 0.6 µm DISTANCE
THEORY FIT:
SILICIDE BINDING = 1.7 eV

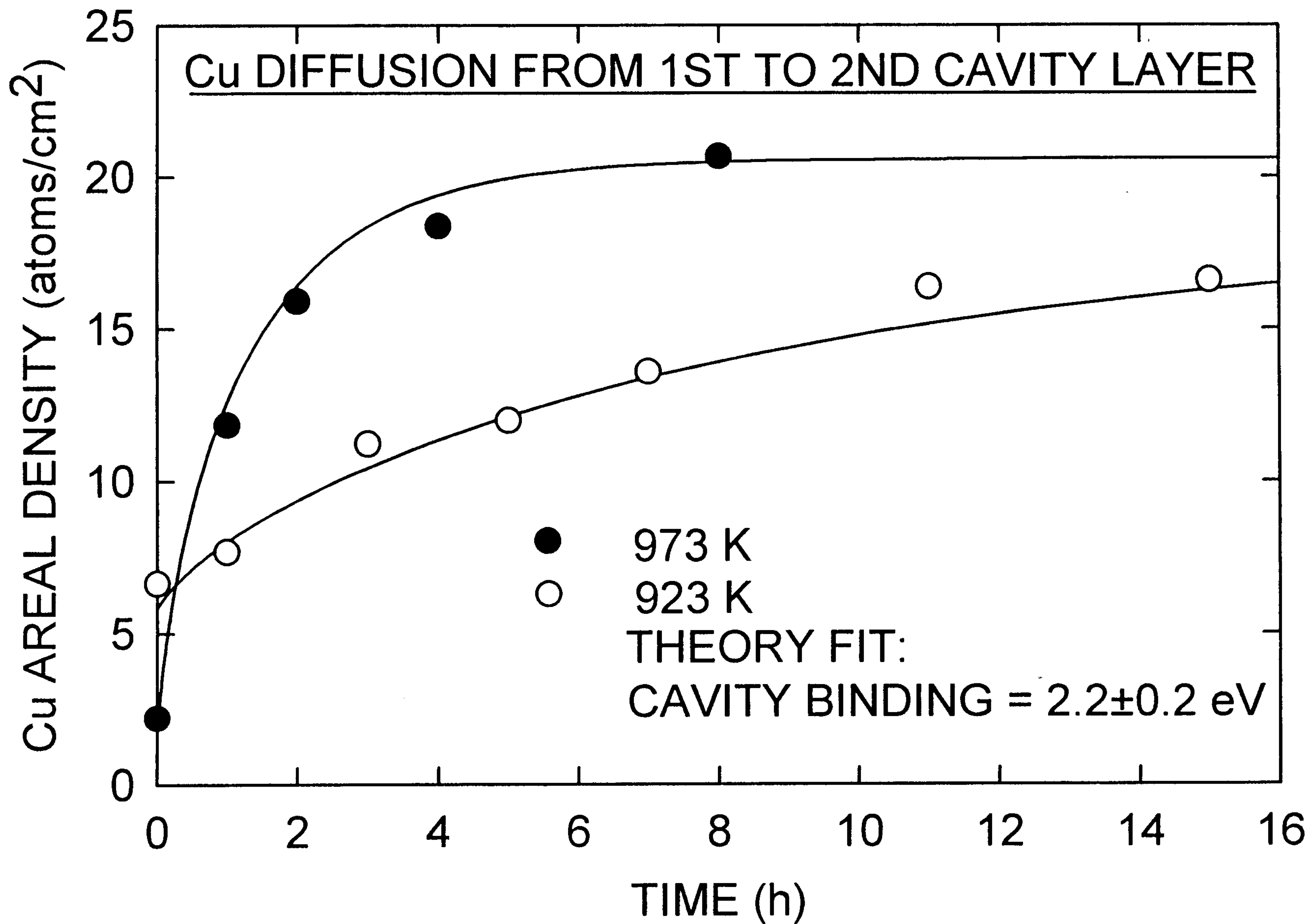

Cu DIFFUSION FROM 1ST TO 2ND CAVITY LAYER
Cu AREAL DENSITY (atoms/cm2)
TIME (h)
973 K
923 K
THEORY FIT:
CAVITY BINDING = 2.2±0.2 eV
0
5
10
15
20
25
0
2
4
6
8
10
12
14
16

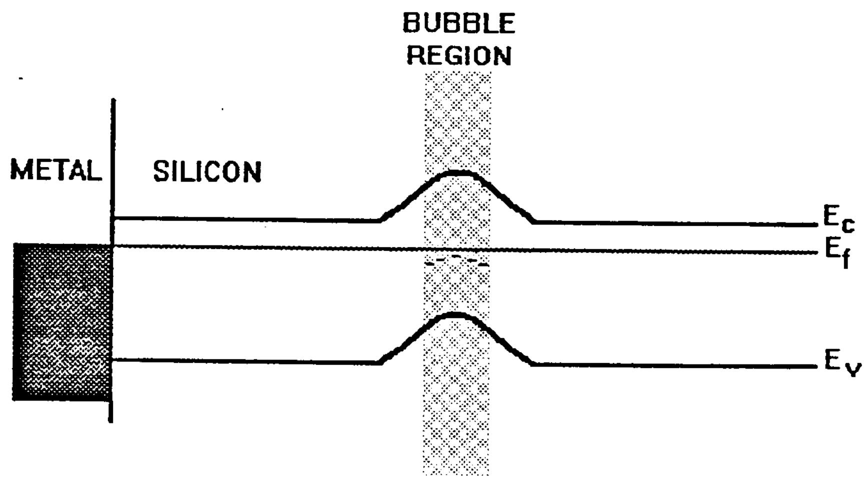
BUBBLE
REGION
METAL
SILICON
E_c
E_f
E_v

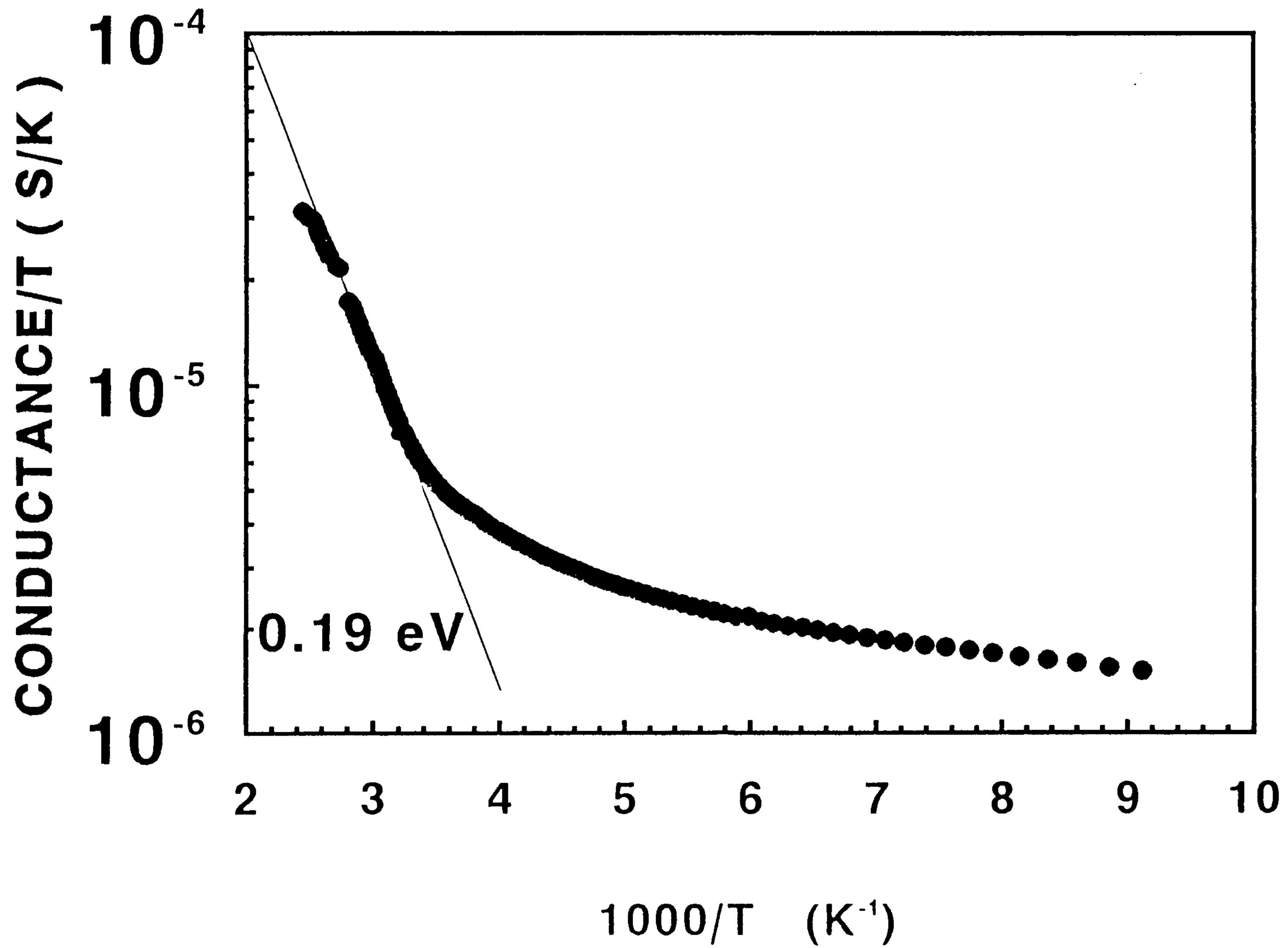

CONDUCTANCE/T (S/K)
10-4
10-5
10-6
0.19 eV
2
3
4
5
6
7
8
9
10
1000/T (K-1)

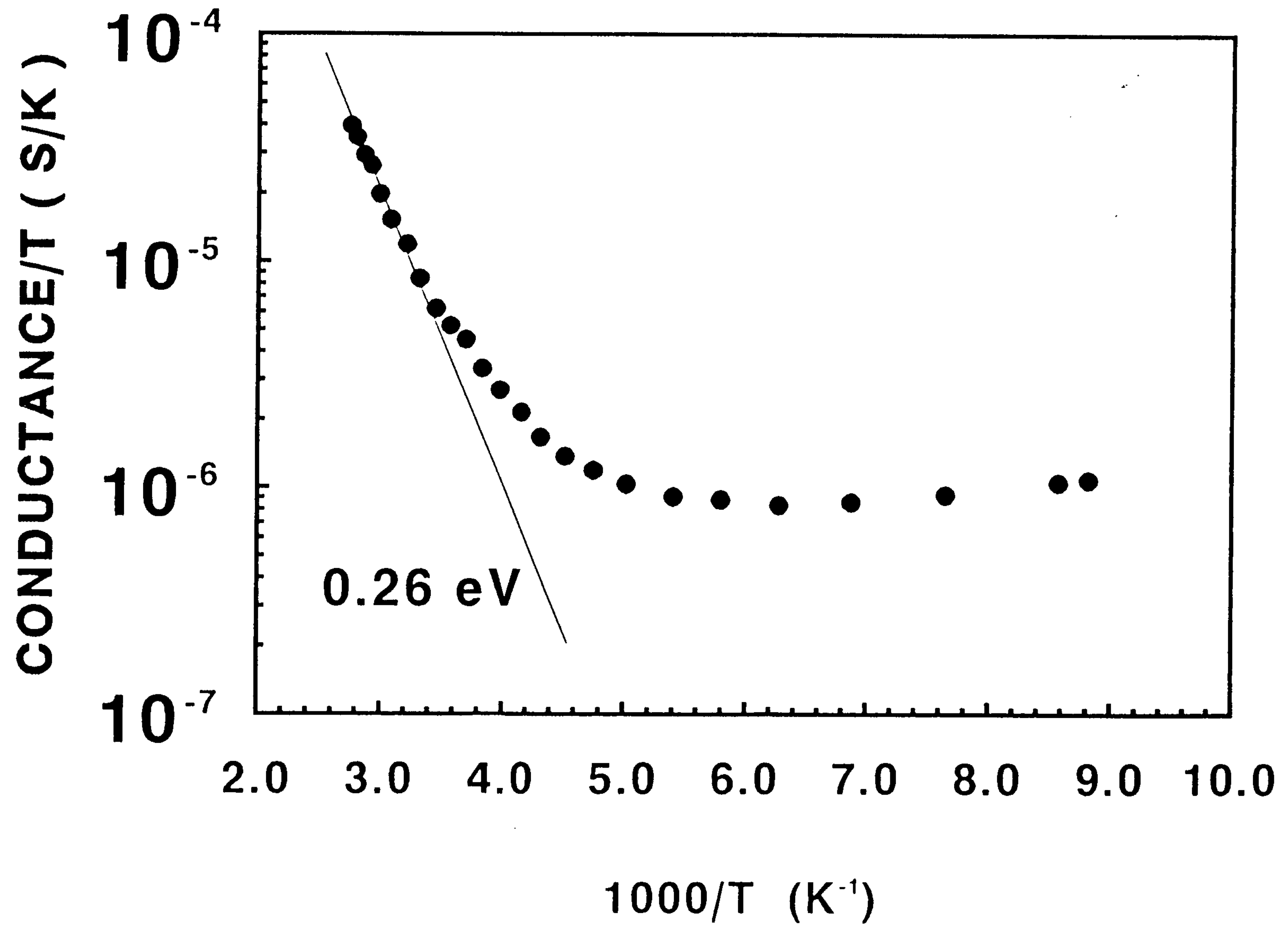
CONDUCTANCE/T (S/K)
10^{-4}
10^{-5}
10^{-6}
10^{-7}
0.26 eV
2.0
3.0
4.0
5.0
6.0
7.0
8.0
9.0
10.0
1000/T (K^{-1})

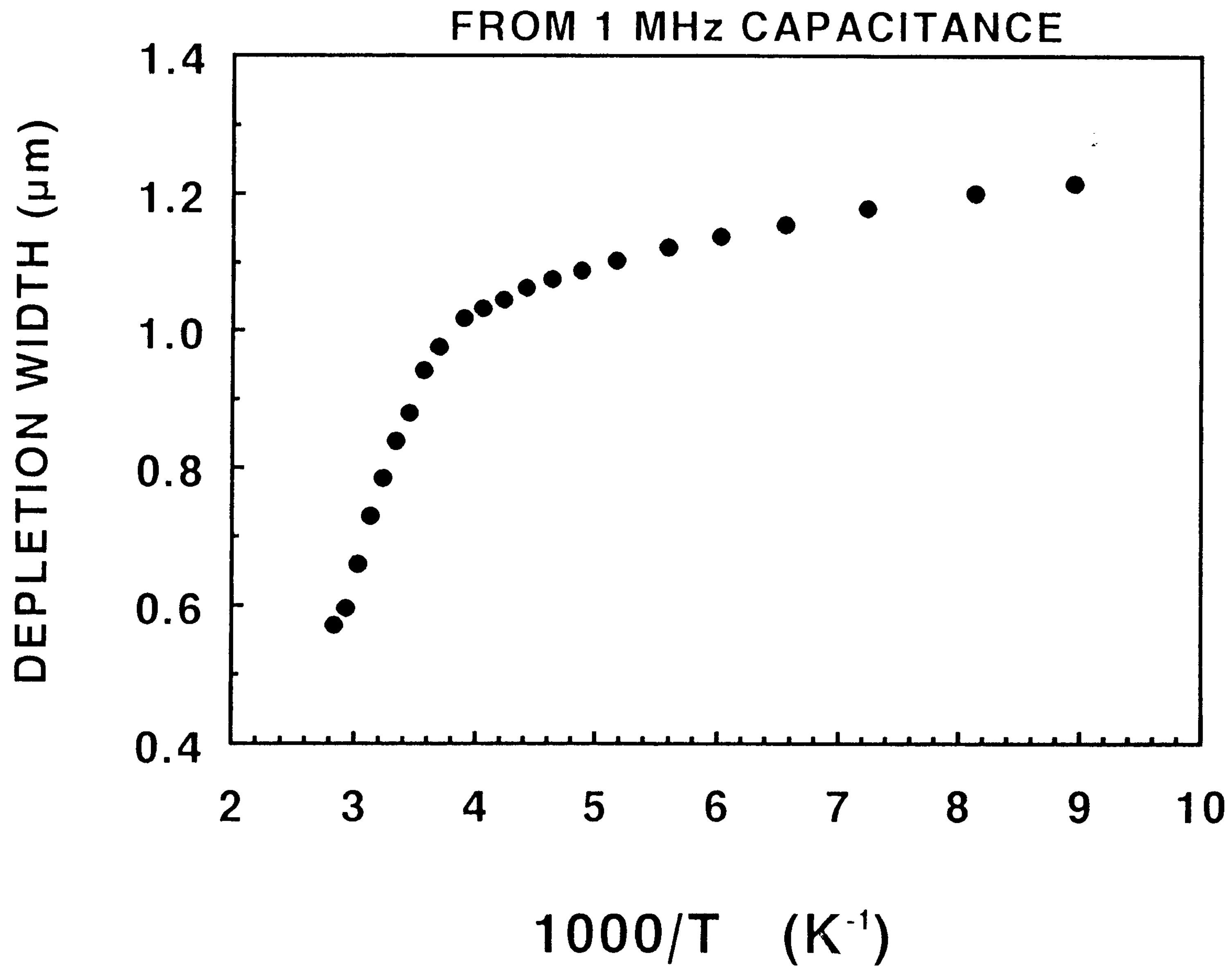
FROM 1 MHz CAPACITANCE
DEPLETION WIDTH (μm)
1.4
1.2
1.0
0.8
0.6
0.4
2
3
4
5
6
7
8
9
10
1000/T (K-1)

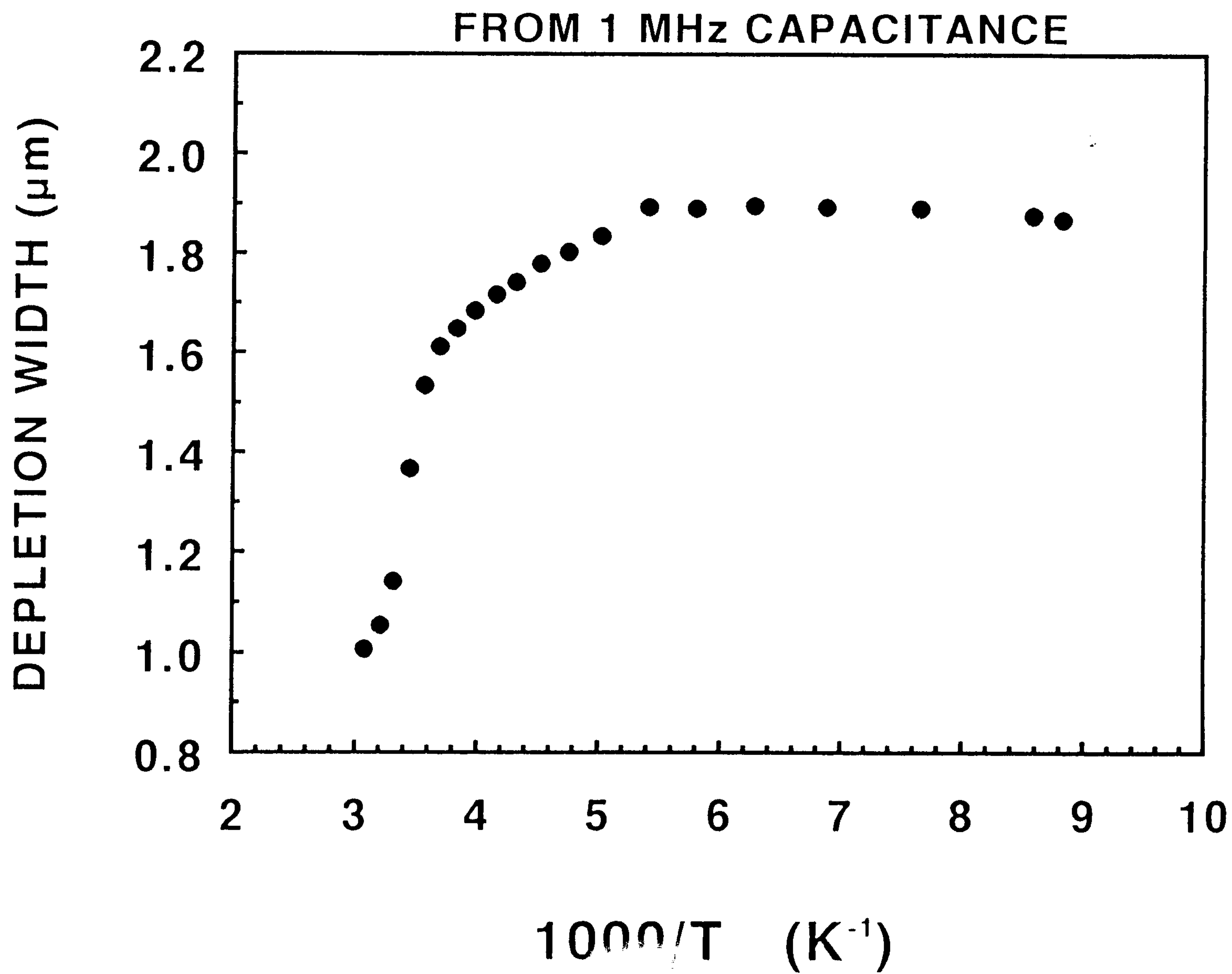
FROM 1 MHz CAPACITANCE
DEPLETION WIDTH (μm)
2.2
2.0
1.8
1.6
1.4
1.2
1.0
0.8
2
3
4
5
6
7
8
9
10
1000/T (K-1)

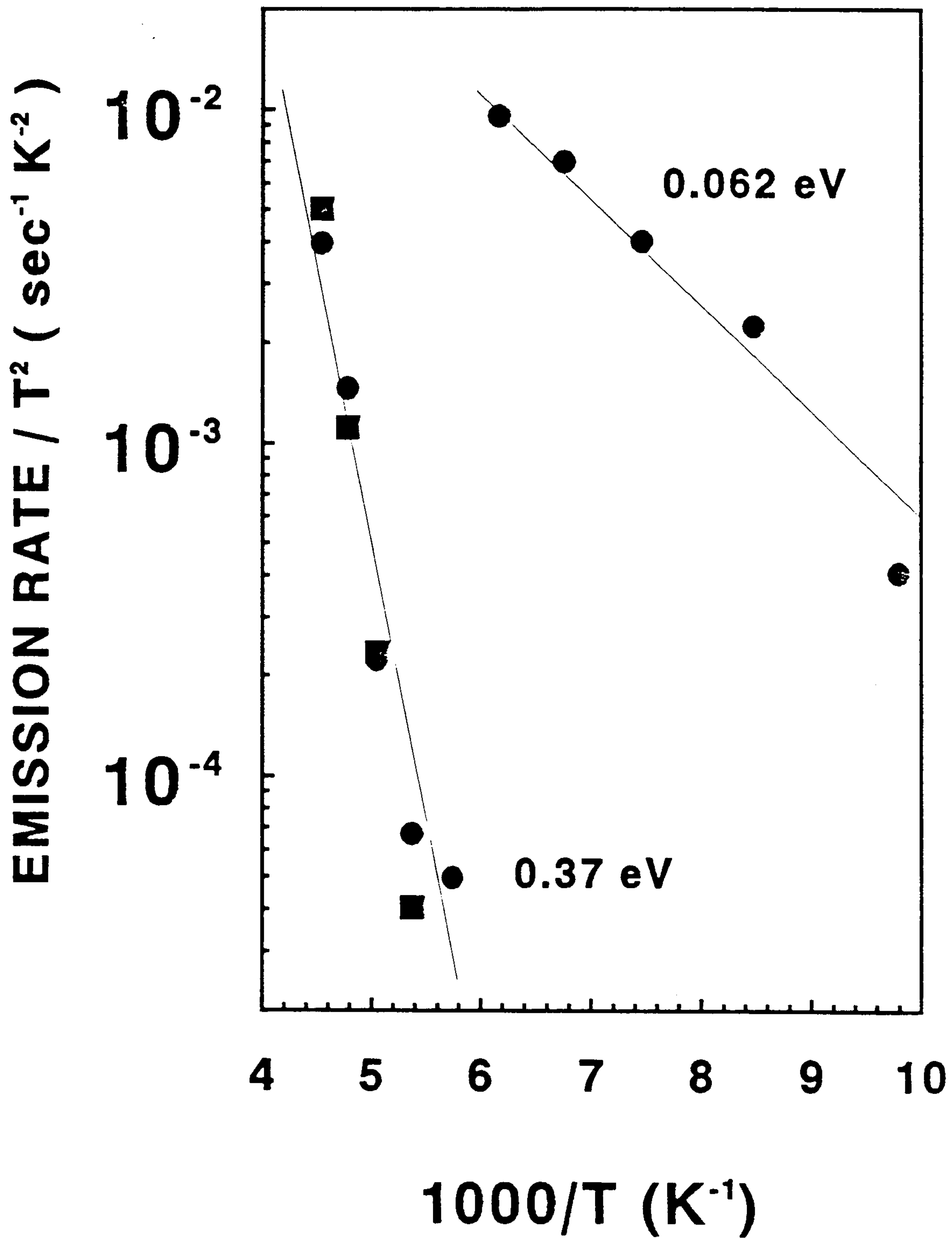
EMISSION RATE / T^2 (sec^{-1} K^{-2})
10^{-2}
10^{-3}
10^{-4}
0.062 eV
0.37 eV
4
5
6
7
8
9
10
1000/T (K^{-1})

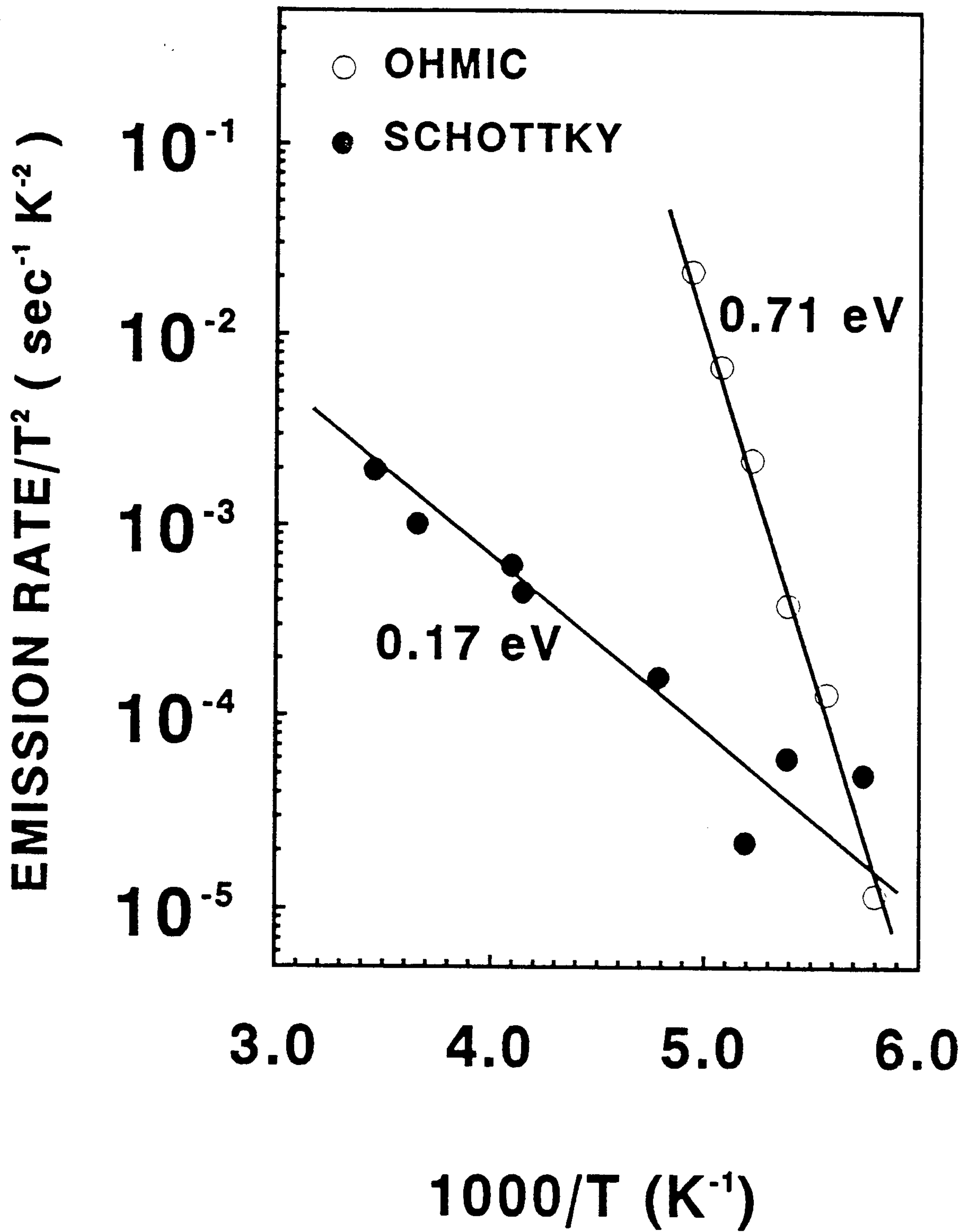
OHMIC
SCHOTTKY
EMISSION RATE/T² (sec⁻¹ K⁻²)
10⁻¹
10⁻²
10⁻³
10⁻⁴
10⁻⁵
0.71 eV
0.17 eV
3.0
4.0
5.0
6.0
1000/T (K⁻¹)

Effects of Aluminum Gettering and Forming Gas Anneal on Multicrystalline Silicon Solar Cells

A. Rohatgi, P. Sana, M. S. Ramanachalam, and W. B. Carter
University Center of Excellence for Photovoltaics Research and Education
Georgia Institute of Technology, Atlanta, Georgia 30332-0250

J. P. Kalejs, and R. O. Bell
Mobil Solar Energy Corporation
4 Suburban Park Drive, Billerica, MA 01821

ABSTRACT

This paper presents a detailed and controlled investigation of various beneficial effects of Al treatment and FGA on multicrystalline silicon solar cells. It was found that Al treatment can getter process-induced as well as grown-in defects and impurities by providing a sink near the Al/Si interface. High stress or dislocation density in the material enhances the gettering efficiency of the Al process. This could either result from direct impurity diffusion through dislocations cores or generation of point defects due to dislocation movement which can aid the impurity diffusion process. Beneficial effect of Al on silicon solar cell performance was found to be material specific. Cast polysilicon cells showed about 1% increase in absolute cell efficiency primarily due to Al gettering induced effective diffusion length enhancement. Finally, the EFG cells showed 5.2% increase in the absolute cell efficiency out of which 1.7% increase resulted from Al gettering, 2.6% from passivation due to forming gas treatment alone, and 1.2% from the passivation or hydrogenation due to Al and forming gas interaction. Exact mechanism for FGA induced passivation is still not fully understood. We believe that forming gas interaction with the n^+ region and/or defects on the front and Al on the back injects atomic hydrogen in the bulk for passivation.

INTRODUCTION

The beneficial effects of aluminum treatment on silicon solar cell performance and minority carrier diffusion length have been reported by a number of investigators [1,2,3]. However, it is not fully understood whether this is the result of gettering, defect passivation, formation of p^+ BSF, light trapping, or some combination of these effects. Aluminum treatment is generally performed by evaporating a thin Al layer on the back followed by a high temperature drive-in. A number of suggestions and speculations have been made in the literature about the mechanism behind the effects of Al. For example it has been suggested that Al treatment passivates grain boundaries and reduces surface recombination velocity [2], it results in possible introduction of hydrogen in the wafer [3], it provides sink for gettering impurities [4] and its gettering efficiency is a function of dislocation density [1], and it can introduce light trapping due to pitting or texturing of the

surface [5]. Al and phosphorus gettering effects are shown to be complimentary making phosphorus-diffused n^+ emitter and Al-diffused p^+ Back Surface Field (BSF) a very promising process scheme for fabricating solar cells on defective silicon materials. In spite of the lack of understanding of the exact mechanism(s) of Al-induced improvements, the aluminum treatment is attractive for low-cost solar cells because it is inexpensive, non-toxic, forms p^+-BSF and is highly compatible with solar cell fabrication. The objective of this paper is four fold: (a) investigate if Al treatment can mitigate the detrimental effects of process-induced defects and contaminants (b) determine if the beneficial effects of Al are enhanced by higher stress or dislocation density in the material (c) investigate the beneficial effects of forming gas and (d) decouple and quantify effects of Al and forming gas anneal such as gettering and passivation.

RESULTS AND DISCUSSIONS

In order to assess the interaction of Al treatment with process-induced contaminants or stress in the material, a controlled investigation was conducted on n-type high- resistivity (500 Ω-cm) high-quality FZ silicon wafers with 2-3 ms bulk lifetime to minimize the interplay of grown-in defects. Al treatment was performed on dislocation free FZ silicon by thermal evaporation of 1-2 μm thick Al on both sides of the wafers, followed by a 1000 °C/3 hr drive in N_2 ambient. It is important to note that only one half of each wafer was covered with Al on both sides while the other half was bare. In order to determine the effect of Al treatment on process-induced contaminants, Al drive-in was performed in a "contaminated" furnace which is routinely used for metal contact sintering and generally gives lifetimes below 0.3 ms due to furnace-induced contaminants. After the 1000 °C heat treatment, remaining Al layer on the surface was etched and the bulk lifetime was measured by an inductively coupled PCD technique, which decouples the emitter saturation current density J_o and true bulk lifetime [6]. Lifetime on the bare half of the wafer (no Al) was determined by the PCD measurements with silicon wafer immersed in HF to minimize or eliminate the surface recombination effects on the measured lifetime [7].

In order to understand the correlation between the stress in the material and the beneficial effects of Al, the above FZ wafers were subjected to four point bend loading process (Figure 1) at 1000 °C for 3 hours in N_2 ambient to create stress and generate dislocations. By varying the load (quartz rods) in the range of 0-40 gms during the heat treatment the stress was varied in the range of 0-10 MPa, which resulted in dislocation density in the range of 0-10^5 cm^{-3}. After introducing the stress, half the wafer was coated with Al on both sides and then subjected to an additional 1000 °C/3 hr. drive in the contaminated furnace. At the end of the loading and Al treatment cycle, PCD lifetimes were measured on both halves of each wafer to determine if gettering efficiency of process-induced contaminants is affected by stress or dislocation density in silicon. It is important to note that at 1000 °C, the yield stress in silicon is 5-7 MPa [8]. The corresponding lifetime data after the 1000 °C/3 hrs heat treatment in Figure 2 shows that the bare half of the wafer, with no Al, had a lifetime of only ~150 μs, which was found to be essentially independent of stress. However the Al coated halves gave a lifetime of 400 μs when the material had no stress, 550 μs with 4 MPa stress, and 2200 μs when the stress was increased

to 8.3 MPa. Thus it appears that the stress or dislocations, especially above the yield stress, enhance the gettering efficiency of Al. This can happen due to direct impurity diffusion through the dislocation cores or generation of point defects (Si vacancy or interstitial) due to nonconservative motion of dislocations which can expedite the impurity diffusion to the sink. It is also important to note that the presence of dislocations alone is not sufficient for lifetime enhancement because, as seen from Figure 2, if Al is not present the lifetime remains below 200 μs even in the stressed samples.

After having established that the Al treatment can getter process-induced contamination and its gettering efficiency is enhanced by stress in the material, we fabricated n^+-p-p^+ solar cells on 0.8 Ω-cm cast poly silicon from Osaka Titanium Corp. and 2.7 Ω-cm EFG sheet material from Mobil Solar to determine if the beneficial effects of Al are material specific. The emitter region was formed by 930 °C/25 min phosphorous diffusion followed by an etch back to increase the sheet resistance from 16 Ω/□ to 80 Ω/□. Then 1 μm thick Al layer was thermally evaporated on the back, followed by a 850 °C/35 min drive-in. First 5 min drive-in was done in O_2 ambient to grow a passivating oxide on the front, before switching to the N_2 ambient. Samples were then slow cooled down to 400 °C and subjected to the first 400 °C/2 hrs. anneal in either forming gas or N_2 ambient to investigate the possible interaction of Al with the forming gas to generate atomic hydrogen for passivation. A Ti-Ag grid was formed on the front by a lift-off process while the back contact was formed by evaporating Ti-Ag contact on top of the Al BSF. In some instances, when there was no Al BSF (Al-sintered cells), a thin Al layer was deposited and a second 400 °C anneal in N_2 or forming gas was performed before the Ti-Ag evaporation on the back. Finally, a 550 Å ZnS/ 1100 Å MgF_2 double layer antireflection coating was deposited on the front. All the cells were characterized by light and dark I-V and spectral response measurements. PC-1D device modelling [9] was performed to understand the Al effects on cast polysilicon cells by ignoring the grain boundary effects.

Consistent with the previous experiments, cells fabricated on one half of each wafer had Al on the back side (Al-diffused cells with BSF) prior to high temperature drive-in while the other half was kept bare (Al-sintered cells with no BSF) during the 850 °C/35 min drive-in.

Figure 3 shows the data for the cast polysilicon cells, with and without the Al process. The IQE data revealed an appreciable increase in the effective diffusion length from 183 to 245 μm and an absolute cell efficiency improvement of ~1% due to the Al process. Model calculations in Table I show that in these 300 μm thick OTC polysilicon cells with 183 μm diffusion length, Al BSF can only produce an efficiency improvement of ~0.1%. Model calculations in Table I also show that the observed 1% increase in cell efficiency in this case results primarily from the enhanced diffusion length due to the Al gettering. As explained by us in reference (5), the effects of reduced back surface reflectance and possible back surface texturing due to Al alloying/pitting cannot be totally ignored in the perceived enhanced diffusion length.

Figure 4 shows the cell data for the Al-diffused and Al-sintered EFG cells. EFG cells showed much higher improvement (1.7%) in absolute cell efficiency due to the Al alloying process. This improvement is supported by a significant increase in quantum efficiency, measured without any light bias. Since the EFG material has lower diffusion

length compared to the cast poly cells, the effect of BSF is expected to be even smaller and, therefore, it is reasonable to conclude that Al gettering significantly improves the bulk diffusion length of the EFG material, Figure 4.

As indicated before, cell fabrication involved a forming gas treatment at 400 °C for 2 hrs, after the 850 °C Al drive-in step. This was done intentionally to enhance the beneficial effect of Al, if the remaining Al or Al/Si alloy layer can generate atomic hydrogen by reacting with the 10% molecular H_2 in the forming gas. Effects like these have been suggested and seen in MOS devices [10,11] where the 400 °C anneal in forming gas significantly lowers the SiO_2/Si interface state density by hydrogen passivation of dangling Si bonds. Similar effects have been speculated for solar cells [3]. The suggested mechanism in the literature involves the interaction of Al with H_2O present in the oxide which generates atomic hydrogen.

In order to decouple and quantify the improvement due to gettering and passivation effects, some additional sintered OTC polycells were fabricated in which the second FGA was replaced by nitrogen anneal in an attempt to turn off the passivation mechanism, if any, due to forming gas/Al interaction. Cell data showed that there was virtually no change in the cell performance. Thus in the case of cast poly cells the beneficial effect can be attributed to Al-induced gettering rather than passivation or BSF. This suggests that either there is no passivation/hydrogenation due to Al/FGA interaction or OTC poly does not respond to hydrogenation.

In order to investigate the issue of Al gettering and FGA passivation further, we fabricated 4 kinds of cells on EFG material, which is known to respond quite favorably to hydrogen passivation. Then we turned off one mechanism at a time to see the effect of passivation and gettering. Figure 5 shows that when all the positive features are incorporated in the process, namely Al diffusion, first FGA and the second FGA/Al interaction for defect passivation, then the highest cell efficiency of ~13.8-14.1% is achieved, which is comparable to good EFG cells made by intentional hydrogen ion implantation. If the Al diffusion is eliminated by fabricating Al sintered cells then a significant drop in IQE and cell efficiency, from 13.8 to 12.4%, is observed. This shows that Al-induced gettering improves EFG cell efficiency by ~1.5%, which is greater than what was observed for cast poly material. This is not surprising since EFG material has more grown-in defects and impurities. Figure 5 shows that if the Al/FGA interaction is turned off by replacing the second FGA by nitrogen anneal in the case of sintered cells, then the IQE drops further and the EFG cell efficiency decreases from 12.4 to 11.2%. This suggests that Al/FGA interaction leads to hydrogenation/passivation in the EFG material. Finally if both the 400 °C FGA anneals are replaced by nitrogen anneals then the EFG cell efficiency drops significantly to 8.6%, which indicates that the first FGA alone does significant defect passivation in the EFG material. Thus unlike the OTC poly, EFG material benefits from both Al gettering and forming gas-induced defect passivation.

CONCLUSIONS

Al treatment can mitigate the adverse effect of process-induced contaminants by providing a gettering sink near the Al/Si interface, possibly due to the pitting/damage of

the alloyed surface. High stress or dislocation density in the material enhances the gettering efficiency of Al process, possibly by accelerating the diffusion of contaminants. This could either result from direct impurity diffusion through dislocations cores or generation of point defects due to dislocation movement, which can aid the impurity diffusion process. Beneficial effect of Al on silicon solar cell performance was found to be material specific. Cast polysilicon cells showed about 1% increase in the absolute cell efficiency, primarily due to Al gettering-induced effective diffusion length enhancement. The EFG cells showed 5.2% increase in the absolute cell efficiency out of which 1.7% increase resulted from Al gettering, 2.6% from passivation due to forming gas treatment alone, and 1.2% from the passivation or hydrogenation due to Al and forming gas interaction. Exact mechanism for Al gettering and FGA induced passivation is still not fully understood and should be investigated to obtain maximum benefit from these treatments.

Table I. PC-1D Model Calculations for OTC Polysilicon Cells

Cell ID	BSF	J_{sc} (mA/cm^2)	V_{oc} (mV)	FF	Efficiency (%)	Diffusion Length (μm)
Al-diffused	Yes	34.3	610	0.755	15.8	245
Al-sintered	No	33.5	602	0.734	14.8	183
Al-BSF	Yes	33.7	603	0.734	14.9	183

REFERENCES

1. S. Martinuzzi, H. Poitevin,M. Zehaf and C. Zurletto, "Improvement of electron diffusion lengths in polycrystalline silicon wafers by Aluminum", Rev. Phys. Appl. **22**, 1987, pp. 645-648.

2. R. Sundaresan, D.E. Burk and G.L. Fossum, "Potential Improvement of Polysilicon Solar cells by Grain Boundary and Intragrain Diffusion of Aluminum", J.Appl. Phys., **55**, 1984, pp.1162-1167.

3. R. Janssens, R. Mertens, and R. Van Overstraeten, "Effects of Grain Boundary Passivation in Polycrystalline Solar Cells", in Proceedings of Sixth, 1981, pp. 1322-1325.

4. R.D. Thompson and K.N. Tu, "Low temperature Gettering of Cu, Ag and Au across a wafer of Si by Al", Appl. Phys. Lett. **5**, 41, 1982.

5. A. Rohatgi, P. Sana, and J. Salami, "Record High Efficiency Solar Cells on Cast Polycrystalline Silicon", in the Proceedings of the Eleventh European Photovoltaic Specialists Conference, PVSEC Montreux, Switzerland, 1992.

6. R.R. King, E.W. Thomas, W.B. Carter and A. Rohatgi, "The Effect of Aluminum and Boron Solid-Source Doping on Recombination in Silicon solar cells", Conference Record of the Twenty Second IEEE Photovoltaic Specialists Conference, (Las Vegas, NV) 1991, pp. 229-235

7. E. Yablonovitch and T. Gmitter, " Auger Recombination in silicon at low carrier

densities", Appl. Phys. Lett. **49**, 1986, pp.587-90.

8. A. Oueldennaoua, R. Allen, A.George and M.Michel, "On the yield point of floating-zone silicon single crystals, II. A quantitative analysis of the dislocation structure at the lower yield point", Phil. Mag. A, **57**, 1988, pp.51-77.

9. P. A. Basore, D. T. Rover, and A. W. Smith, "PC-1D Version 2: Enhanced Numerical Solar Cell Modelling", in Proceedings of the 20th IEEE Photovoltaic Specialists Conf., 1988, pp. 389-396.

10. Reda R. Razouk, and Bruce E. Deal, "Dependence of Interface State Density on Silicon Thermal Oxidation Process variables", Journal of Electrochemical Society, **126**, 9, 1979, pp. 1573-1581.

11. E. H. Nicollian, and J. R. Brews, "MOS (Metal Oxide Semiconductor) Physics and Technology", John Wiley and Sons, 198?.

Figure Captions

Fig.1 A schematic of the four point bend loading and Al diffusion experimental sequence.

Fig.2 Effect of stress and Al diffusion on carrier lifetime in the sequentially processes float-zone silicon samples.

Fig.3 A comparison of the measured IQE and cell data for Al diffused and Al sintered cast polysilicon cells.

Fig.4 A comparison of the measured IQE and cell data for Al diffused and Al sintered EFG silicon cells.

Fig.5 Measured IQE and cell data for EFG cells with and without Al diffusion and with and without forming gas treatment.

Fig.6 Measured IQE and cell data for EFG cells to decouple the effects of Al diffusion and forming gas treatment.

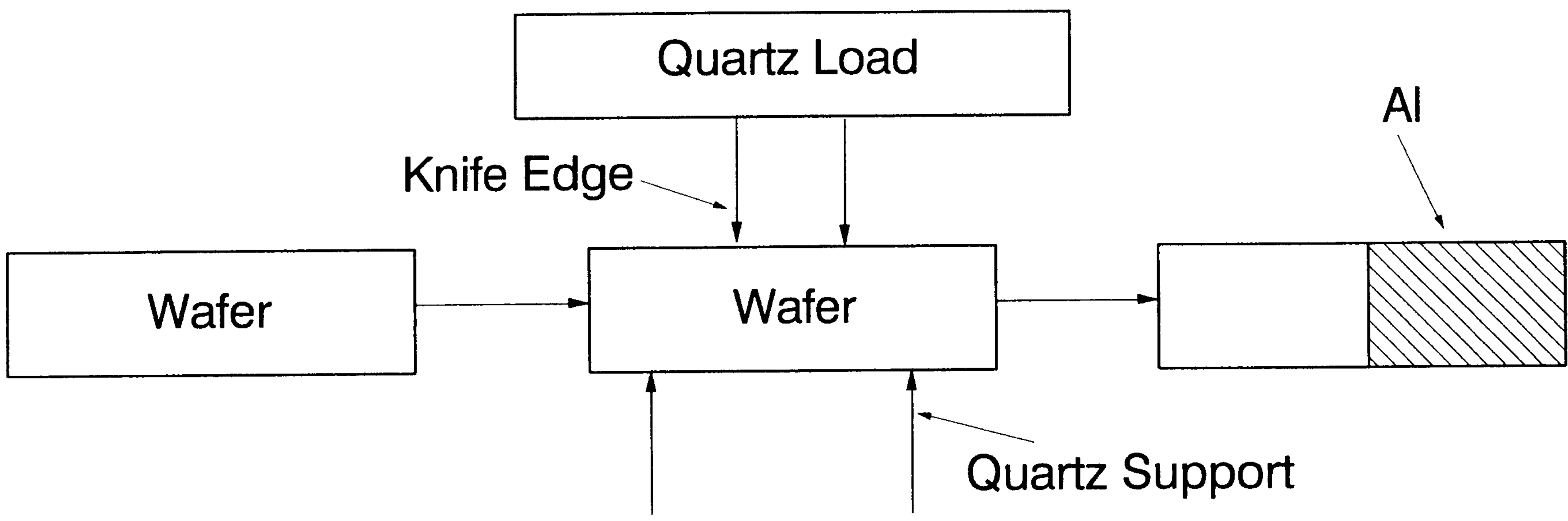

As Cleaned

Four Point Bend Loading
at 1000 C

Al Treatment
at 1000 C

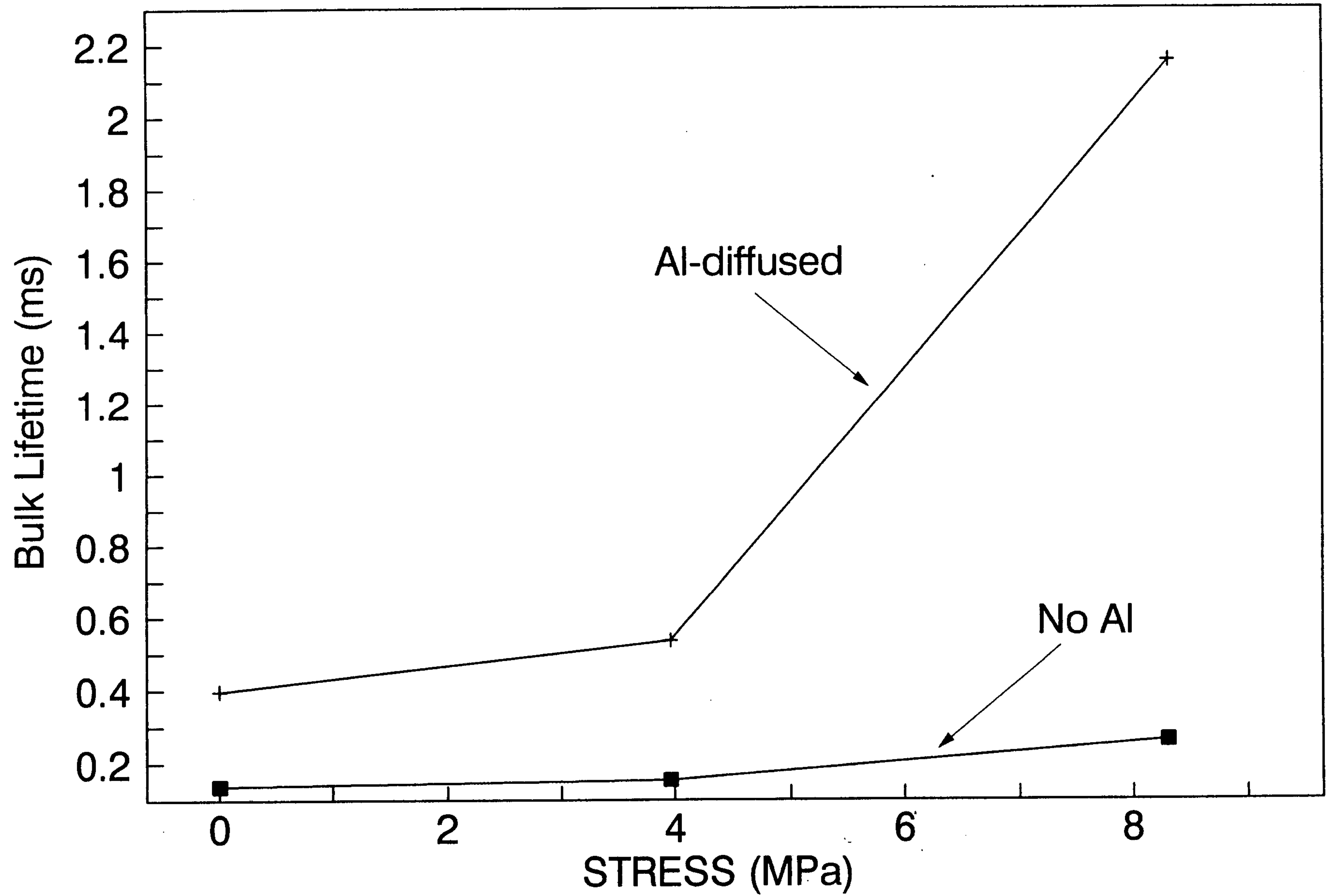
Bulk Lifetime (ms)
2.2
2
1.8
1.6
1.4
1.2
1
0.8
0.6
0.4
0.2
Al-diffused
No Al
0
2
4
6
8
STRESS (MPa)

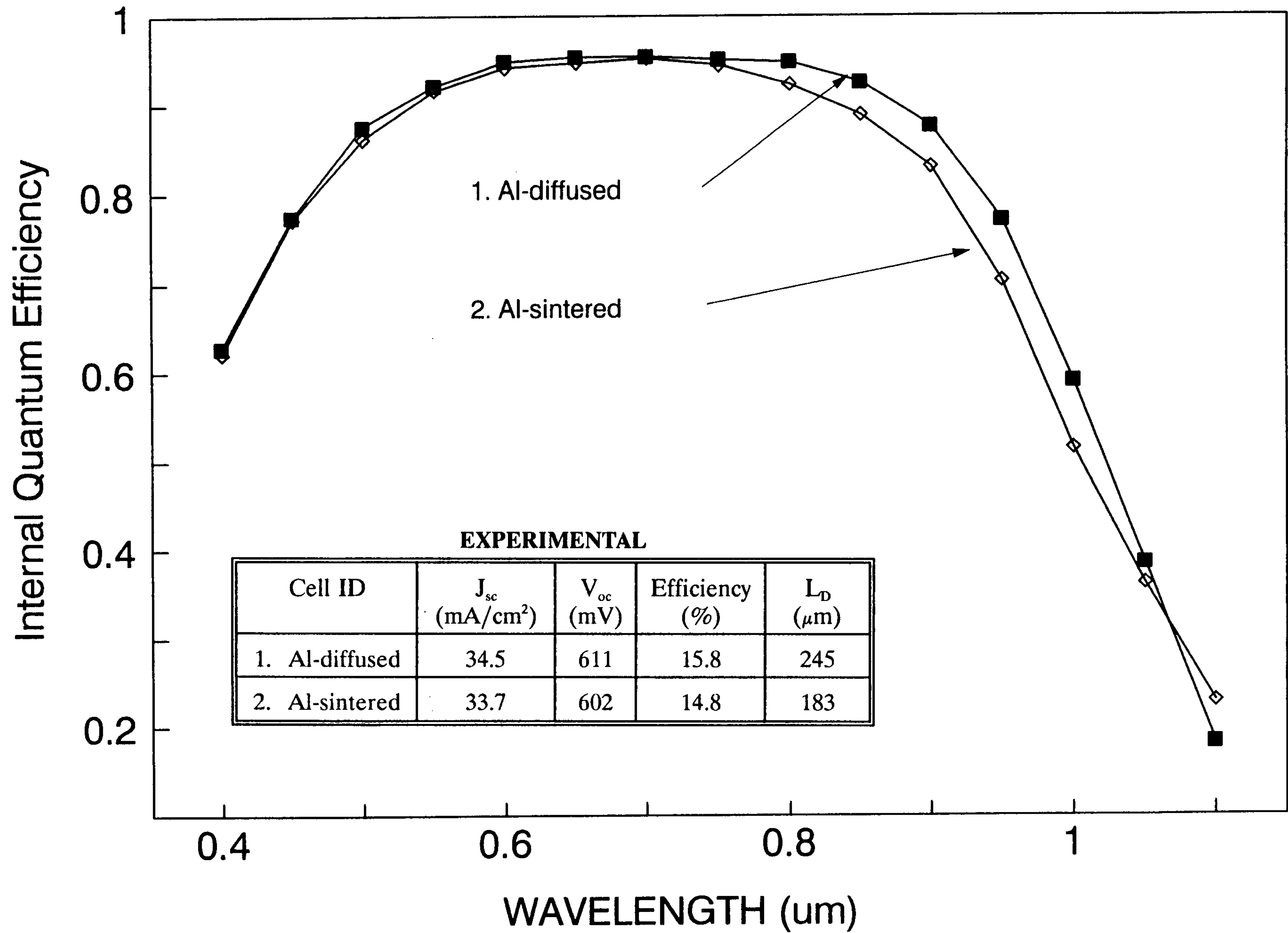

Cell ID	J_{sc} (mA/cm^2)	V_{oc} (mV)	Efficiency (%)	L_D (μm)
1. Al-diffused	34.5	611	15.8	245
2. Al-sintered	33.7	602	14.8	183

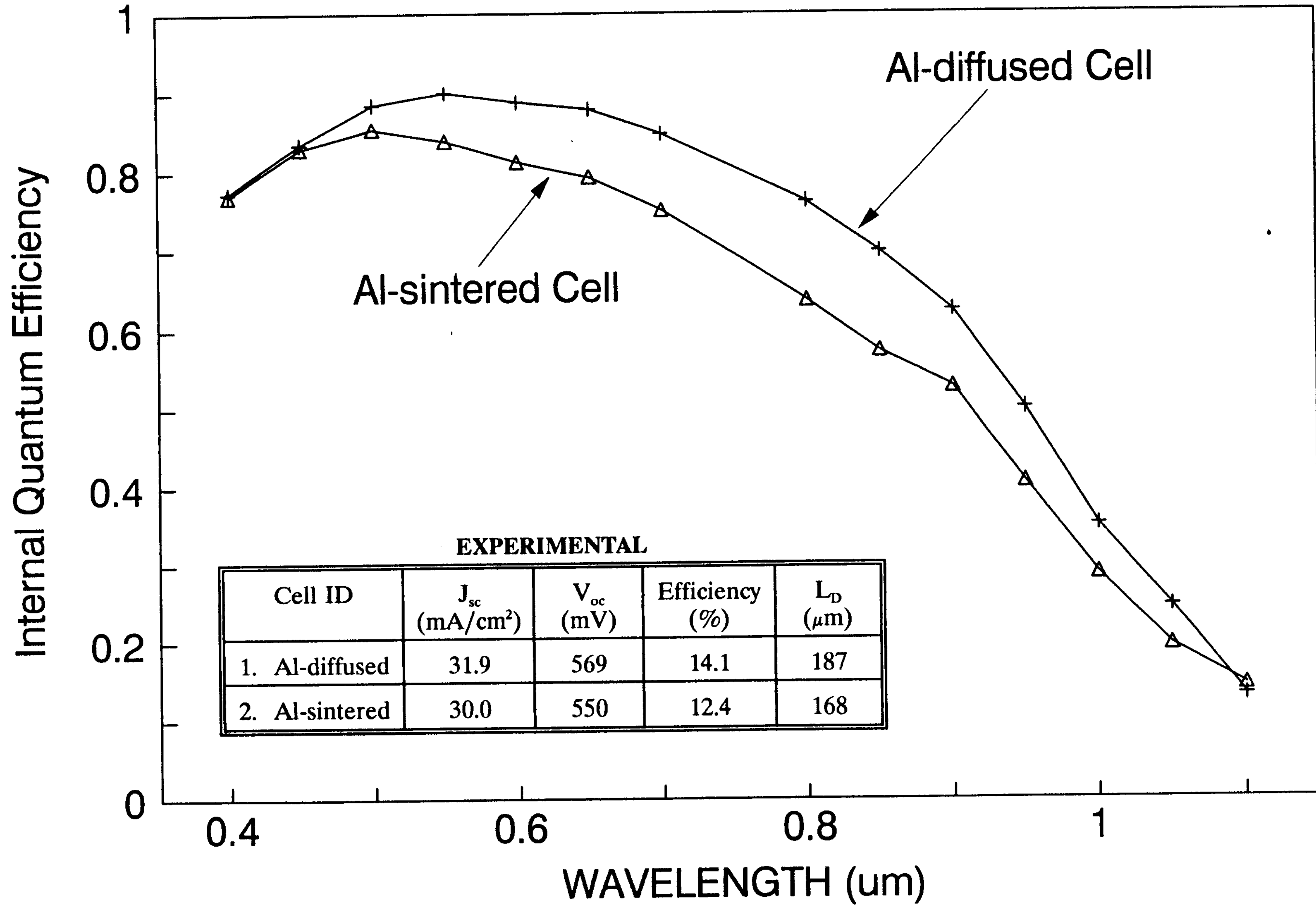

Cell ID	J_{sc} (mA/cm^2)	V_{oc} (mV)	Efficiency (%)	L_D (μm)
1. Al-diffused	31.9	569	14.1	187
2. Al-sintered	30.0	550	12.4	168

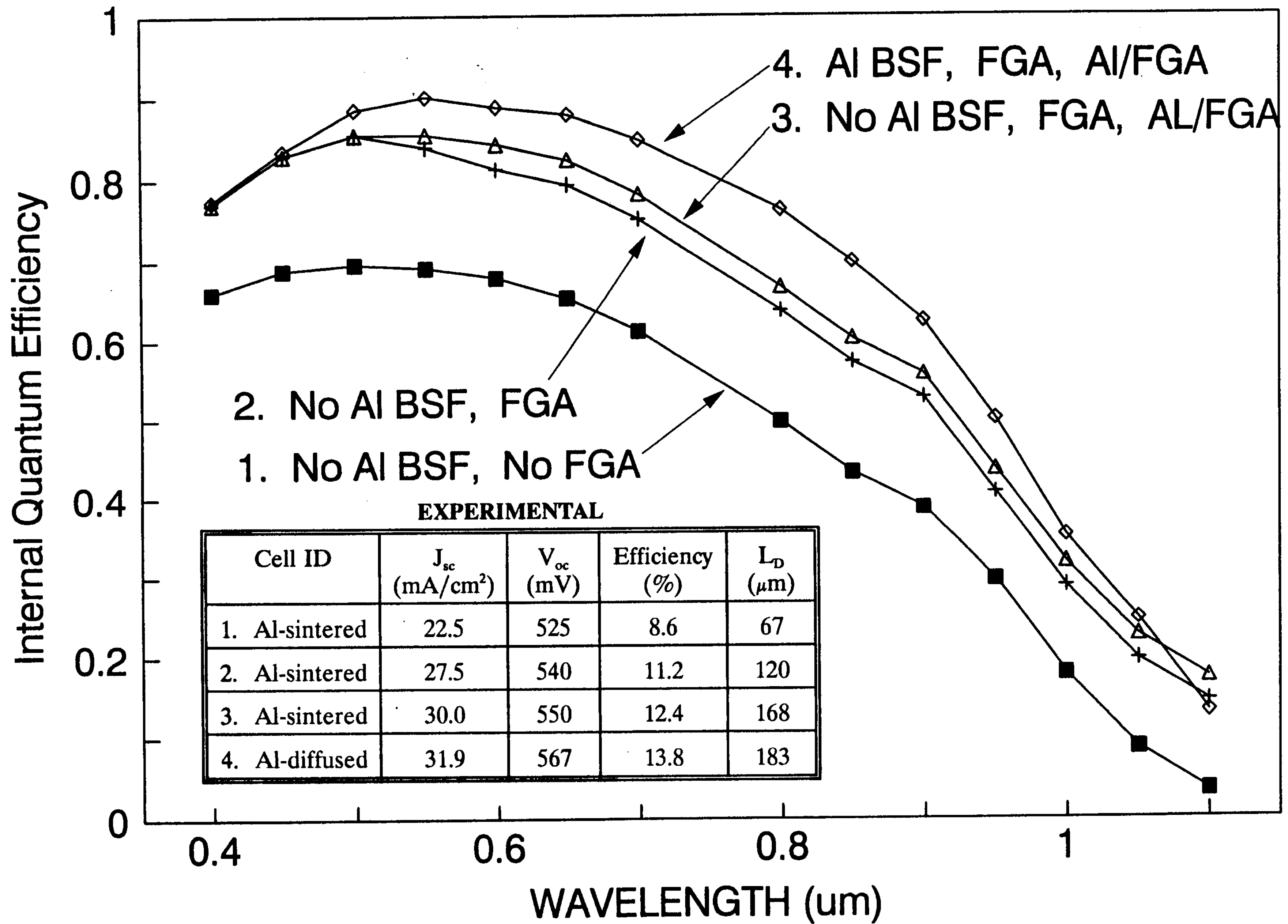

Cell ID	J_{sc} (mA/cm^2)	V_{oc} (mV)	Efficiency (%)	L_D (μm)
1. Al-sintered	22.5	525	8.6	67
2. Al-sintered	27.5	540	11.2	120
3. Al-sintered	30.0	550	12.4	168
4. Al-diffused	31.9	567	13.8	183

HYDROGEN DIFFUSION AND PASSIVATION MECHANISMS

Stefan K. Estreicher
Physics Department – Texas Tech University, Lubbock TX 79409-1051

Talk given at the third NREL workshop on
The Role of Point Defects and Defect Complexes in Silicon Device Processing

Abstract
It is known that hydrogen is able to remove the electrical activity of a wide range of impurities and lattice defects. In the case of photovoltaic devices, the passivation of energy levels which are electron-hole recombination centers is a highly desirable goal. The efficiency of the passivation process and the stability of the passivated centers depend on a number of parameters, such as the charge state of hydrogen, its diffusion properties, the capture radius of hydrogen by a particular center, the temperature, the exposure to light, the dopant concentration, and other factors. While it is possible to control some of these parameters, not enough is understood about others to allow for the optimization of the processes taking place. In particular, there is no consensus regarding the charge states and diffusion mechanisms of hydrogen in silicon. In this talk, I will briefly review the current understanding of hydrogen in Si, with emphasis on recent experimental and theoretical data. I will also discuss the results of our ongoing calculations which suggest the existence of a new mechanism for hydrogen diffusion involving the vacancy-hydrogen pair.

1. Comments on hydrogen passivation

It is well known[1] that hydrogen has the ability to remove the electrical activity associated with a wide range of shallow- and deep-level impurities and defects in many semiconductors. These include shallow acceptors and donors, some transition metal impurities, as well as dangling bonds at localized (*e.g.*, vacancies or divacancies) or extended (*e.g.*, dislocations or grain boundaries) defects. Passivation normally results from the formation of a covalent bond between hydrogen and a weak or stretched host atom bond. This allows an unfavorable configuration to relax, thus shifting offending energy levels from the gap into a band.

The shallow dopant-hydrogen pairs begin to dissociate at rather low temperatures (100 ℃ to 150 ℃). The dissociation temperature is often lowered and the dissociation rate enhanced by exposure to band-gap light. However, many deep centers tend to remain passivated up to higher temperatures (typically 400 ℃). The passivation of deep centers and their good thermal stability are desirable properties for photovoltaic applications since the presence of energy levels deep in the gap dramatically decreases the lifetime of charge carriers. The efficiency of a passivation process depends on a variety of factors, the two most important ones being the capture radius and the diffusivity.

The *capture radius* R_c of hydrogen by an electrically active center is the dominant factor in situations where interactions between charged species are involved. A Coulombic R_c is of the order of 50 Å, as compared to only 5 Å or so when either H or the defect to be passivated are electrically neutral. A Coulombic capture radius is believed to be responsible for the very high efficiency of shallow acceptor passivation in Si: $B^- + H^+ - \{H, B\}^0$. On the other hand, it is quite possible that it is a Coulomb *repulsion* that prevents the passivation of other impurities. The example that comes to mind is interstitial Ti. At the tetrahedral interstitial (T) site, its equilibrium charge state is +1 in intrinsic and p-type material. The interaction of Ti^+ with H^+ results in a long-ranged

repulsion between the two species. The charge state of H could also be -1, but it is not clear whether this species is long-lived in Si. Other factors influencing R_c include the strain field caused by the defect or its dipole moment. For example, the behavior of H appears to be strongly affected by concentrations of interstitial O in Si of the order of $10^{18}\ cm^{-3}$, as evidenced by qualitative differences in the behavior of positive muons in CZ vs. FZ material (see *e.g.*, Figs. 45 and 72 in Ref. 2).

The *diffusivity* of H is another important factor in any passivation process, since H must reach the centers to be passivated as quickly as possible. The difficulty here is that there is not just one diffusivity $D(T) = D_0 e^{-E_a/kT}$ but several, depending on the state of hydrogen which is diffusing and on the trapping of that state at impurities and defects. One could be dealing with H^0 (at the T or bond-centered (BC) sites), with H^+ (at the BC site), or even H^- (at the T site). Further, the H_2^* complex (see below) has been predicted to be mobile as well, while H_2 should not be mobile, but might break up into mobile species via the capture of an electron or hole. Further, as will be discussed below, pairs such as $\{V, H\}$ or $\{I, H\}$ (where V is a vacancy and I a self-interstitial) could be rapidly diffusing entities as well. Thus, there are about half-a-dozen forms of H able to contribute to a net diffusivity, each with its own prefactor D_0, activation energy E_a, and trapping characteristics. How much of each species is present in a given sample depends on many factors and perhaps on the history of the sample. This is a possible reason why plots of the measured diffusivity of hydrogen vs. the inverse temperature often differ so much from one author to the next. At very high temperatures, when no trapping of H occurs, a single diffusivity is measured,[3] with activation energy $E_a \simeq 0.5\,eV$. It probably corresponds to H^0 hopping from T site to T site.

Thus, the efficiency of a passivation process depends in a non-trivial way on the temperature, the Fermi level, the exposure to light, the concentrations of charge carriers, hydrogen, vacancies, etc. Experimental and theoretical information on the various species of hydrogen and their diffusion properties is a pre-requisite to the optimization of the passivation processes. This paper deals with a summary of the current understanding of the states of hydrogen in silicon.

2. The "old" muon spin rotation data and the AA9 center

Positive muons have been used since the mid 1970's to study the behavior of a hydrogen analog in semiconductors.[2] The muon is much lighter than the proton ($m_\mu \simeq m_p/9$), which affects its diffusion characteristics. However, the reduced masses of hydrogen and muonium and their electrostatic interactions are virtually identical. Spin polarized muons are injected into a sample where they thermalize in a few ns. The muon decays in about $2.2\,\mu s$ into a positron and two neutrinos, and the positron is emitted preferentially in the direction of the spin of the muon. Thus, by monitoring the time and angular dependence of the decay positron, one can directly measure hyperfine (hf) parameters and local fields. In semiconductors, three distinct muonium-related centers are formed at low temperatures and in high-resistivity material.

The most stable one is neutral muonium at the BC site. It was first denoted Mu^*, but since its theoretical[4] and experimental[5] identification, it was relabeled "Mu^0_{BC}". Its hf tensor is highly anisotropic, which is only possible if it is *localized* (non-diffusing). Indeed, any hopping between adjacent BC sites would average out the hf interactions, leading to a loss of anisotropy. Mu^0_{BC} is a true $Si - Mu - Si$ bridged bond (3-center, 2-electron bond). The odd electron resides in a non-bonding orbital localized primarily on the two nearest neighbors (NNs) to the muon.

The second signal, originally labeled Mu, is also paramagnetic but with an isotropic hf tensor. It corresponds to neutral interstitial muonium at the T site or hopping rapidly between sites of lower symmetry in a way that produces a hf tensor with T_d symmetry. This species is now labeled "Mu^0_T". A thermally-induced Mu^0_T — Mu^0_{BC} transition proves that the BC site is more stable

than the T site. The latter site is substantially populated because there is a large barrier separating the two configurations: A relaxation of a $Si - Si$ bond of some 35% is needed for the BC site to become a minimum of the energy.

Finally, "μ^+" is the name originally assigned to the third signal, which is not paramagnetic, and *a priori* could be $(Mu_T)^{+/-}$, $(Mu_{BC})^{+/-}$, $\{\mu^+, B^-\}$, $\{Mu, B\}$, $\{Mu, C\}$, or a number of similar complexes in which the electrons are paired. A $Mu^0_{BC} \rightarrow \mu^+$ transition occurs around $120\,°K$ and is interpreted as the ionization of the BC species, since its odd electron is weakly bound (see above). However, recent studies indicate that the nature of μ^+ may be quite different in *p*- and *n*-type material (see §5).

μSR studies were the only source of experimental information on isolated hydrogen-like species in semiconductors until a hydrogen-related EPR signal labeled AA9 was reported[6] in 1987. Its hf tensor coincides[7] very closely with that of Mu^0_{BC}. This center was produced at low temperatures in proton implanted samples (with energies in the MeV range) after strong illumination. Recently, this experiment has been repeated,[8] the assignment to H^0_{BC} confirmed, and the annealing behavior fits that of Mu^0_{BC}. The ionization energy of H^0_{BC} (or Mu^0_{BC}) is about $0.2\,eV$.

3. The theoretical story

The first breakthrough occurred with the identification[4,9] of bond-centered hydrogen in Si. The theoretical predictions[10] regarding isolated hydrogen can be grouped into two categories.

First came the calculations based on Hartree-Fock theory, which usually approximate the host crystal with hydrogen-saturated molecular clusters. Cluster sizes range from 5 to 44 atoms. The picture emerging from these calculations is the following.[11] Neutral interstitial hydrogen is metastable in silicon. The stable state is at the BC site and the metastable state at or near the T site. The latter species diffuses with the activation energy $E_a \simeq 0.5\,eV$, while the former cannot hop directly from BC to BC site. Instead, it hops to a T site, diffuses along $< 111 >$ directions from T to T site, until it eventually self-traps at another BC site. H^+ is the ionized version of H^0_{BC}. Since H^+ and H^0_{BC} differ only by an electron in a non-bonding orbital, and since H^0_{BC} does not diffuse directly from BC to BC site, the diffusion of H^+ was predicted to occur via T site, as a neutral species: H^+ hops out of a BC site toward a T site and captures an electron in the process. It then diffuses as H^0 until it self-traps at another BC site where it ionizes spontaneously. The presence of an electric field (external or caused by the presence of ionized acceptors in the material) promotes the hopping out of a BC site along field lines.

In 1988 and 1989, two first-principles local-density-functional calculations were published,[12,13] and provided a different picture for the behavior of hydrogen in Si. These calculations used periodic supercells to represent the host crystal, with cell sizes ranging from 8 to 64 atoms.

These two calculations disagree with each other and with earlier Hartree-Fock results about neutral interstitial hydrogen. One group[12] finds H^0 to be only stable at the BC site, the other[13] finds H^0 to be stable at the T site and metastable at the BC site. However, both calculations predict that hydrogen should exhibit *negative-U behavior* in Si, in the sense that the reaction $2H^0 \rightarrow H^+ + H^-$ is exothermic. This implies that only H^+ (at the BC site) and H^- (at the T site) are stable. The positive species is predicted[12] to diffuse directly from BC to BC site with an activation energy of $0.20\,eV$, and the negative species from T site to T site with $E_a = 0.25\,eV$.

This new picture implies that μSR observes mostly metastable states since about 90% of incoming muons form paramagnetic centers at low temperatures. This is not impossible since only one muon is present in the sample at any given time. However, it also implies that H^0_{BC} is highly mobile, which conflicts with the observed anisotropy of the hf tensor of both the Mu^* and the AA9 centers. On the other hand, it provides a simple explanation for the high efficiency of acceptor passivation

($H^+ + B^- - \{H,B\}^0$) and explains donor passivation ($H^- + P^+ - \{H,P\}^0$), although the latter reaction should lead to a much greater passivation efficiency than is actually observed. At present, there is debate among theorists and experimentalists about the existence and stability of H^-. However, it is now clear that the properties of interstitial hydrogen vary with the Fermi level.

4. Hydrogen dimers: Theory and experiment

Early theoretical studies[14] have predicted that the molecular form of hydrogen (H_2) should be the most stable state of hydrogen in Si. The first predictions were made long before all the low energy states of H were known (in particular the BC configuration and the H_2^* complex), and were therefore incomplete. Most theorists now agree that the molecule is very near the T site, an almost free rotator (somewhat more stable in a $< 111 >$ orientation), with a barrier for diffusion of the order of $2\,eV$. It is often assumed that H_2 accounts for the "invisible" hydrogen that always seems to be present in the crystal.

Recently, the observation[15] by EPR of a center that looks very much like H_2^+ or H_2^- has been reported. The spectrum is consistent with two hydrogen atoms symmetrically located on either side of the hexagonal interstitial (H) site, which all theorists find to be a saddle point of the energy for H_2^0. A number of details are still missing.

A second type of dimer was independently predicted by Jones,[16] Chadi,[17] and Deák.[18] It consists of a bond-centered/anti-bonding pair known as H_2^* (or $H_{BC}H_{AB}$). The predicted[17] activation energy of H_2^* is $0.8\,eV$. Various groups have calculated the relative energies of H_2 and H_2^*, and most authors find the two species to be quite close in energy. A recent calculation[19] suggests that the two species should be nearly energetically degenerate, their formation probabilities depending mostly on which precursors are present in the crystal. H_2 is the likely result of the interaction of two H_T^0's, and H_2^* that of H_{BC}^0 with H_T^0. In intrinsic and p-type material, the BC species dominates, at least up to room temperature. In n-type material, the situation is far less clear, but the BC site is probably less stable. This would favor H_2 species in n-type Si.

The H_2^* complex has now been observed by IR spectroscopy (including D substitutions and uniaxial stress experiments). The vibrational modes have been measured and calculated.[20] There is no experimental information regarding the diffusion properties of H_2^*.

5. The "new" muon spin rotation data

Recent developments in RF-μSR technology[21] allow the monitoring of the intensity of the various μSR species as a function of temperature in variously doped material. Of greatest interest is the identification of "μ^+", since many different species (including H^+ and H^-) could contribute to this signal (see Sec. 2). Preliminary data are now in press.[21] The key results are reproduced in Fig. 1.

The intensity if the μ^+ species was monitored in B-doped (left column) and P-doped (right column) Si with concentrations ranging from $10^{12}\,cm^{-3}$ (top row) to $10^{15}\,cm^{-3}$ (bottom row). The experimental data (open circles) were fitted (solid line) to dynamic models assuming a variety of possible transitions. The Topsil data are now well understood: Below $120\,°K$, only a few percent of incoming muons form μ^+ (the rest forms either Mu_{BC}^0 or Mu_T^0). In the range $120\,°K$-$150\,°K$, the abrupt increase in the intensity of the signal can only be explained by a direct ionization process. It is the ionization of Mu_{BC}^0. The $Mu_{BC}(+/0)$ energy level is therefore predicted to be $0.22 \pm 0.01\,eV$ below the conduction band edge. This number is close to the ionization energy obtained for the AA9 center.[20]

Above $150\,°K$, the more gradual increase in the intensity of μ^+ cannot be explained by a direct ionization process, such as a $Mu_T^0 - (Mu_T^+)$ transition. Instead, it is explained by a site change followed by a quick ionization: This is the $Mu_T^0 - Mu_{BC}^0$ transition (with barrier height $0.39 \pm$

$0.04\,eV$) immediately followed by the ionization of the BC species. This agrees with the theoretical prediction that the electron is strongly bound to H_T^0.

The fall off of μ^+ intensity above $400\,^\circ K$ is due to a rapid charge exchange process. This is associated with a BC$\rightarrow$T reverse site change, where the charge state is 0. This is consistent with a theoretical prediction that the stability of the BC site decreases while that of the T site increases with temperature.[22]

In B-doped material, the behavior is very similar and the fit (solid line) remains good. Two new features are present. First, the low-temperature intensity of μ^+ increases with the dopant concentration (this is not fully understood, but could be caused *e.g.*, by $\{Mu, B\}$ pair formation). Second, a step around $50\,^\circ K$ is visible. It can be fitted to a hole capture process at the BC site: $Mu_{BC}^0 + h^+ \rightarrow Mu_{BC}^+$.

In P-doped material, the situation is not clear yet. The experimental data are not fitted well with the model developed for intrinsic and p-type Si, and the BC site appears to be playing a lesser role. The model currently considered includes the ionization of Mu_T^0, *i.e.*, Mu_T^{-1}.

6. Emerging picture

The experimental and theoretical data discussed above lead to the following behavior for H in crystalline Si. Note that the *qualitative* discussion below is a risky attempt on my part to characterize the behavior hydrogen by piecing together the information currently available. This discussion ignores the depletion region data, although I believe that many of them would fit in this picture.

a) At low temperatures (below liquid nitrogen), almost all of interstitial H is in the neutral charge state, a fraction at (or very near) T sites as H_T^0 and the rest at BC sites as H_{BC}^0. The former interstitial is mobile with $E_a \simeq 0.5\,eV$, the latter can only diffuse by hopping first to a T site. Both H_2 and H_2^* species can form if the concentration of hydrogen is high enough. It is not clear what happens in highly doped material, even below the temperature at which dopants ionize.

b) As the temperature is increased (up to $100\,^\circ C$ or so), the dopants ionize, the Fermi level shifts, and the situation becomes different in p- and n-type material.

(i) In p-type material, the two transitions $H_{BC}^0 \rightarrow H_{BC}^+$ and $H_T^0 \rightarrow H_{BC}^0 \rightarrow H_{BC}^+$ take place, which substantially increases the concentration of H^+. This species probably diffuses via the neutral H_T^0 state, but tends to be kicked out of the BC site along electric field lines. Many hydrogen-acceptor pairs form. Both H_2 and H_2^* dimers should be present.

(ii) In n-type material, the BC site appears to be less stable. A substantial fraction of interstitial H is at T sites, possibly in the form of H^- which could have a short lifetime ($\simeq \mu s$? Long lifetimes for H^- would lead to easy and complete passivation of shallow donors). Hydrogen-donor pairs form, and the dominant dimer should be H_2 (since H_2^* requires the presence of an H_{BC}^0 precursor).

c) Above $200\,^\circ C$, the BC site becomes unstable, even in high-resistivity material. Rapid charge-exchange mechanisms take place and hydrogen spends just a fraction of its time in the $+1$ and -1 states. Most pairs and other complexes break up (the more solid $Si-H$ bonds would remain stable a little longer).

7. A new diffusion mechanism for hydrogen?

Analyses of secondary-ion mass spectrometry (SIMS) data led J.W. Corbett *et al.*[23] to speculate that hydrogen-vacancy complexes are mobile. Recent hydrogenation studies by Sopori[24] in vacancy-rich Si also suggest that a enhanced hydrogen diffusion results from the presence of large concentrations of vacancies. While it is now established that $\{V, H_n\}$ complexes (with $n = 1, \ldots, 4$) do form in Si,[25] nothing is known about the diffusion properties of these species.

We have studied[26] vacancies, vacancy-hydrogen complexes, and their diffusion properties. Although many calculations are still under way, our results show that the $\{V, H_1\}$ pair is indeed mobile, while the $\{V, H_{n>1}\}$ complexes are not. The key results are summarized below.

The neutral vacancy distorts slightly outward from tetrahedral to tetragonal symmetry in order to replace the four dangling bonds by two long bonds between pairs of Si atoms. These bonds are 3.76 Å long but show a substantial amount of covalent overlap. Neutral interstitial hydrogen interacts with these bonds, and one to four H interstitial can fit inside the vacancy. Only $\{V, H_4\}$ is electrically inactive. The gain in energy upon capture of hydrogen decreases somewhat with the number of H's already inside the vacancy but is of the order of 3 eV per H atom.

The vacancy diffuses readily in Si. The calculated barrier for diffusion varies with the amount of electron correlation included in the calculation and the number of host atoms allowed to relax. At the saddle point, a Si atom is exactly half-way between two lattice sites and forms six stretched bonds with its six NNs. Our best number, obtained at the *ab-initio* Hartree-Fock level with split-valence polarized basis sets followed by second-order Møller-Plesset corrections in electron correlation is 1.1 eV, roughly double the experimental number. This was obtained in a small cluster, in which only NNs could be relaxed.

We identified already one possible diffusion mechanism for the $\{V, H_1\}$ pair in Si, and are studying another. The diffusion path we have identified is a three-step process. First, one of the Si atoms nearest to the vacancy moves toward the vacancy along a slightly curves path that keeps it away from the H atom sticking inside V. This atoms moves easily because the presence of H stabilizes the saddle point configuration which does not involve six stretched bonds but only five shorter ones, since H saturates the sixth one. Second, H is forced to move from the Si atom to which it is attached toward the Si atom moving into the vacancy. Finally, the new $\{Si, H\}$ pair rotates as the Si atom sets inside the vacancy, ending up with a configuration identical to the initial one but with $\{V, H\}$ one step further. This three-step process involves a barrier which has two (or three) "bumps" rather than just one (as for the vacancy alone). The first bump is small and corresponds to the first step, the second bump is higher, but involves a very short displacement of H. More details about these results will be published elsewhere.

Acknowledgements

This work was supported by the contract XAI-3-13155-01-105439 from NREL and the grant D-1126 from the R.A. Welch Foundation.

References

[1] For recent reviews, see S.J. Pearton, J.W. Corbett, and M.J. Stavola, "*Hydrogen in Crystalline Semiconductors*" (Springer-Verlag, Berlin, 1992), and S.M. Myers, M.I. Baskes, H.K. Birnbaum, J.W. Corbett, G.G. DeLeo, S.K. Estreicher, E.E. Haller, P. Jena, N.M. Johnson, R. Kirchheim, S.J. Pearton, and M. Stavola, Rev. Mod. Phys. **64**, 559 (1992).

[2] B.D. Patterson, Rev. Mod. Phys. **60**, 69 (1988).

[3] A. Van Wieringen and N. Warmoltz, Physica **22**, 849 (1956).

[4] T.L. Estle, S.K. Estreicher, and D.S. Marynick, Hyp. Int. **32**, 637 (1986); S.K. Estreicher, Phys. Rev. B **32**, 9122 (1987).

[5] R.F. Kiefl, M. Celio, T.L. Estle, S.R. Kreitzman, G.M. Luke, T.M. Riseman, and E.J. Ansaldo, Phys. Rev. Lett. **60**, 224 (1988).

[6] Yu.V. Gorelkinskii and N.N. Nevinnyi, Sov. Phys. Tech. Lett. **13**, 45 (1987).

[7] T.L. Estle, R.F. Kiefl, J.W. Schneider, and C. Schwab, MRS Proc. **163**, 407 (1990).

[8] B. Bech Nielsen, K. Bonde Nielsen, and J. Byberg, Proc. 17th Int. Conf. Defects Semic. (Trans Tech, Switzerland, 1994).

[9] S.F.J. Cox and M.C.R. Symons, Chem. Phys. Lett. **126**, 516 (1986).

[10] For a review of the theoretical techniqes, see S.K. Estreicher, MRS Proc. **242**, 643 (1992).

[11] See e.g., C.H. Chu and S.K. Estreicher, Phys. Rev. B **42**, 9486 (1990).

[12] C.G. Van de Walle, Y. Bar-Yam, and S.T. Pantelides, Phys. Rev. Lett. **60**, 2761 (1988) and C.G. Van de Walle, P.J.H. Denteneer, Y. Bar-Yam, and S.T. Pantelides, Phys. Rev. B **39**, 10791 (1989).

[13] K.J. Chang and D.J. Chadi, Phys. Rev. B **40**, 11644 (1989).

[14] See *e.g.*, J.W. Corbett, S.N. Sahu, T.S. Shi, and L.C. Snyder, Phys. Lett. **93 A**, 303 (1983) and A. Mainwood and A.M. Stoneham, J. Phys. C **17**, 2513 (1984).

[15] P. Stallinga, T. Gregorkiewicz, C.A.J. Ammerlaan, and Yu.V. Gorelkinskii, Phys. Rev. Lett. **71**, 117 (1993).

[16] P. Briddon, R. Jones, and G.M.S. Lister, J. Phys. C **21**, L1027 (1988) and R. Jones, Physica B **170**, 181 (1991).

[17] K.J. Chang and D.J. Chadi, Phys. Rev. Lett. **62**, 937 (1989).

[18] P. Deák and L.C. Snyder, Radiation Effects and Defects in Semiconductors **111-112**, 77 (1989).

[19] Dj.M. Maric, M.A. Roberson, and S.K. Estreicher, Proc. 17th Int. Conf. Defects Semic. (Trans Tech, Switzerland, 1994).

[20] B. Bech Nielsen, J.D. Holbech, R. Jones, P. Sitch, and S. Öberg, Proc. 17th Int. Conf. Defects Semic. (Trans Tech, Switzerland, 1994), and J.D. Holbech, B. Bech Nielsen, R. Jones, P. Sitch, and S. Öberg, submitted to Phys. Rev. Lett.

[21] K.H. Chow, B. Hitti, S.R. Kreitzman, T.L. Estle, J.W. Schneider, R.L. Lichti, and R.F. Kiefl, Proc. 17th Int. Conf. Defects Semic. (Trans Tech, Switzerland, 1994).

[22] S.K. Estreicher and Dj.M. Maric, Phys. Rev. Lett. **70**, 3963 (1993).

[23] J.W. Corbett, J.L. Lindström, and S.J. Pearton, MRS Proc. **104**, 229 (1988).

[24] B.L. Sopori, MRS Proc. **262**, 407 (1992) and Mat. Sci. Forum **83-87**, 1531 (1992), B.L. Sopori, K. Jones, and X.J. Deng, Appl. Phys. Lett. **61**, 2560 (1992).

[25] See *e.g.*, L.M. Xie, M.W. Qi, and J.M. Chen, J. Phys. Cond. Mat. **3**, 8519 (1991).

[26] M.A. Roberson, S.K. Estreicher, L. Korpás, and J.W. Corbett, Proc. 17th Int. Conf. Defects Semic. (Trans Tech, Switzerland, 1994).

FIGURE 1: RF-μSR data in Si for the non-paramagnetic state "μ^+" (open circles) in doped samples with B (left column) and P (right column) concentrations of $< 10^{12} cm^{-3}$ (top) to $10^{15} cm^{-3}$ (bottom). The Mu_T^0 (Mu_{BC}^0) intensities are denoted with a dashed (dotted) line, and are not discussed here. Solid lines (left column) are the results of a dynamical model with parameters fit to the Topsil data. No fit is available in n-type Si. The figure is reproduced with permission from Ref. 21.

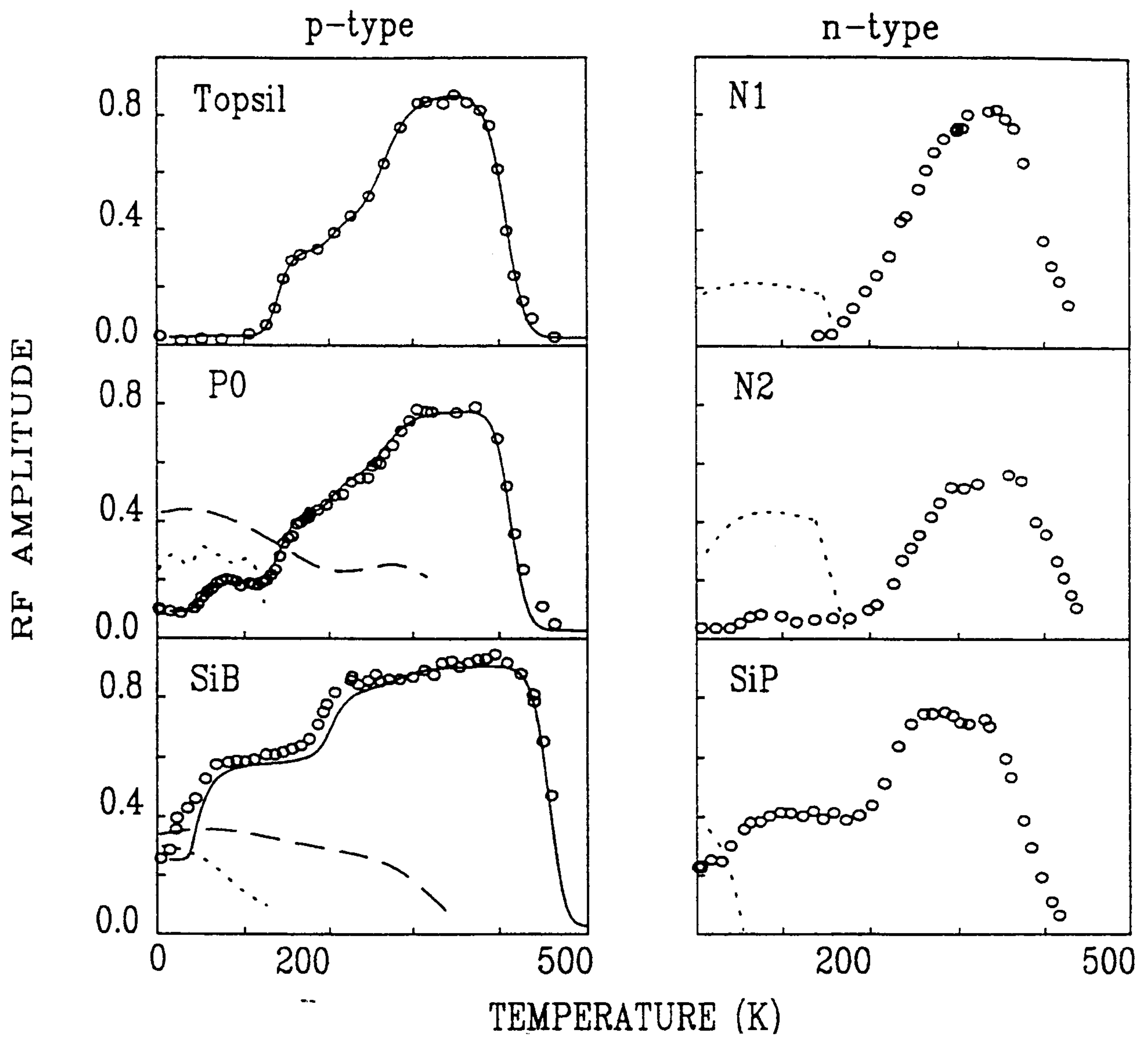

Estreicher. fig. 1

Status and Fabrication of High-Efficiency Single-Crystal Si Solar Cells

R. A. Sinton

Abstract

Recent pilot production of large-area solar cells with one-sun efficiencies exceeding 20% has consolidated process design for good process control. Previously, high-efficiency had been reported primarily for small-area or one-of-a-kind devices. A comparison of record cells and currently-accepted theoretical efficiency limits indicates how future gains may be achieved. In addition, this discussion illustrates some basic properties of silicon material to serve as goals or limits to the properties of lower-cost silicon solar cells. The device physics of very-high efficiency makes stringent demands on surface passivation, dopant-diffused region quality, and device design. A listing of the fabrication process steps successfully used to date on float-zone material to achieve these parameters gives an idea of the allowable process design flexibility. These process steps with FZ silicon are quite different than those used on multicrystalline silicon or even CZ silicon.

High-Efficiency Cells

The demonstrated experimental efficiency for one-sun silicon solar cells first exceeded 20% in 1985[1,2], and has has continued to increase to 23% at present. Initially, these cells were very small, laboratory test devices. Recently, pilot production of cells with efficiencies over 20% has begun in order to address very-high-value markets such as solar race cars. These cells are 35-46 cm^2 and carry a sales price of $500-$800/Watt [5]. They are quite similar to their laboratory predecessors, and are fundamentally limited by the same physics. The large cells lag in efficiency only by 1.5%, probably due to edge losses from saw cuts and the series resistance associated with larger cells.

A scale of solar cell achievements in the context of the theoretical limits is shown in Fig. 1. The upper limit is generally accepted to be determined by the balance of light absorption with the Auger recombination. This limit is 28-29%. If the best demonstrated surface passivations are substituted for ideal surfaces, then the efficiency limit drops to about 25%. The best cell to date is 23.1%[6]. The best large-area cells out of pilot production are 21.3-21.6%[3,4].

The requirements for very high efficiency in silicon are quite well established and can be seen in all examples of high-efficiency cells. Two of these are shown in Fig. 2., the PERL cell from University of New South Wales and the Backside-contact solar cell from Stanford University[7]

The critical common elements are:

1) Light n^+ diffusion with oxidation for front-surface passivation

2) Minimal optimized area of metal-semiconductor contacts
3) Textured surface for reflection control and light-trapping
4) Reflective back surface
5) Minimization of grid-shadow
6) High-lifetime float-zone substrate

The modeled dependence of the efficiency on a critical materials and processing parameter, the substrate lifetime, is shown in Fig. 3. Using achieved experimental parameters for the surface passivations, the efficiency vs. substrate lifetime is shown for a modeled backside contact cell at one-sun and at concentration. This result is modeled for a nominally undoped substrate. At one sun, a substrate lifetime of 100 μs reduces the efficiency down to 18% from the 23% available on a 10 ms substrate. For a concentrator cell, the effect is less severe. A cell capable of 27% would only be 25% on a 100 μs substrate. The efficiency saturation for high lifetimes indicates the region where the characteristic is determined by the surface passivation, the dopant-diffused regions, and the Auger recombination mechanism.

The dependence on lifetime would be less for a PERL cell, due to the junction at the front and the doped substrate.

The difficulties in increasing the short-circuit current of cells is illustrated by the quantum efficiency plot for a recent backside-contact one-sun cell, Fig. 4[4]. The total reflection is less than 5% over the range from 400-1000 nm. The internal quantum efficiency is 100% over this same range. An analysis of the spectral response indicates that the backside mirror is 93% reflective and the light is trapped effectively, with an equivalent of 30 cell-thickness passes for IR light. Despite these rather ideal characteristics, the cell had a current of 39 mA/cm^2, about 4 mA below the theoretical limit for Lambertian light trapping[8]. Part of this difference is simply a limitation of pyramidal texture as a light-trapping scheme.

Solar Cell Front-Surface Passivation Stability

One aspect of surface passivation is of special current interest. In 1988, it was found that the highest quality oxidations used as surface passivations on the record cells were not stable under concentrated UV light. Subsequent cells were more heavily phosphorus doped to achieve stability at the expense of having a beginning-of-life performance penalty. More recently, high-performance passivations have been reported that can recover the previous efficiency and are stable. The results of an experiment with a passivation matrix exposed to concentrated light is shown in Fig. ~~4~~ 5 [9].

Another example of a passivation stability problem was recently reported by Green et al. [10] It was found that UV light degraded the junction-isolation regions around the edge of cells, drastically diminishing the cell performance. Both of these examples indicate that in cells requiring the highest degree of passivation, the potential for UV degradation must be addressed in the cell and process design.

Fabrication Techniques for Very High Efficiency Silicon Solar Cells.

The fabrication of the highest efficiency solar cells on float zone or magnetic Czochralski silicon is quite different from other solar cell fabrication processes. In this particular case, the substrate material as supplied has ideal characteristics, and can only be harmed by the process sequences. Gettering steps that would increase the diffusion length in multi-crystalline silicon material with a 50 µm diffusion length might very well decrease the mm-scale diffusion length in float-zone, or have no effect at all. Fabrication process decisions are made on the basis of two goals:

1) To minimize process complexity to lessen the wafer handing and chance of killing the substrate lifetime.

2) To use processes that yield ideal dopant-diffused regions and surface passivations, and are proven to preserve high-lifetime in substrates.

The first consideration is achieved by complete integration of available tools to result in the shortest possible process runsheet. The tools are qualified by the second consideration. A list of the fabrication processes is discussed below, based upon published process fabrication data from groups reporting cells with efficiencies exceeding 21% at one sun (4,7-11).

Processes Compatible With Very High Efficiencies on Float-Zone Substrates.

Substrate texture:

-NaOH, KOH, Nitric:HF, Nitric: NH_4OH etching.
-Laser texture.

The process of etching to achieve surface texture for <100> silicon is non-controversial. In general, a alkaline anisotropic etch followed by an isotropic etch gives good results in subsequent processing. The success of laser texture is perhaps more surprising. It is postulated that this process may result in less dislocations than the etching process[10].

Dopant Diffusion:

-Drive-in from Phosphorus-doped oxide
-Drive-in from Boron-doped oxide
-$POCl_3$
-BBr_3
-Phosphorus solid-source
-Diffusion from deposited Al
-Use of p-type wafers (PERC cells)

This is a long and versatile list of available options . Others may be added in the near future. Good results have been reported for spin-on dopants used in conjunction with an Optical Rapid Thermal Process[12]. Ion implantation remains a possibility, although this author has not been able to maintain high lifetime after ion-implantation from several difference vendor sources.

Oxidation:

Dry oxidation sequences at temperatures up to 1120 C have been reported that maintain the highest possible substrate quality. A key requirement is that the furnace be cleaned with TCA gettering or equivalent. Forming gas or Al anneals are generally used after oxidation to obtain the best possible surface passivations.

Metalization:

A number of metalization have been used on very-high-efficiency solar cells. These include:

- Evaporated Al
- Evaporated Ti/Pd/Ag with plated Ag
- Sputtered Al
- Ni-Cu, Ni-Ag, and Ni-Au plating

Conclusions

The last few years have seen relatively modest efficiency increases in record cells. A consolidation of results has been seen with large-area cells, more fabrication process options, and commercial availability of 20% cells. Some obstacles to reliable cells, such as the stability of high quality surface passivations, have been overcome. Improvements towards 25% can be foreseen in laboratory one-sun cells. An important pursuit is to continue expanding process options in order to decrease the cost of high efficiency and continue incorporating the knowledge gained into lower-cost solar cells.

Acknowledgements

The author would like to thank Pierre Verlinden and R. M. Swanson of SunPower corporation for collaboration on parts of the work reported here.

References

[1] P. Verlinden, F. Van de Wiele, G. Stehelin, J. P. David, "Optimized Interdigitated Back Contact Solar Cell for High Concentrated Sunlight", Proc. 18th IEEE Photovoltaic Specialist Conference, Las Vegas, NV, 1985, pp. 55-60.

[2] M. A. Green, A. W. Blakers, S. R. Wenham, S. Narayanan, M. R. Willison, M. Taouk, T. Szpitalak "Improvements in Solar Cell Efficiency", Proc. 18th IEEE Photovoltaic Specialist Conference, Las Vegas, NV, 1985, pp. 39-42.

[3] M. A. Green, S. R. Wenham, J. Zhao, "Progress in High Efficiency Silicon Cell and Module Research", 23rd IEEE Photovoltaic Specialist Conference, Louisville, KY., May 1993.

[4] R. A. Sinton, P. J. Verlinden, R. A. Crane, R. M. Swanson, C. Tilford, J. Perkins, and K. Garrison, "Large-Area 21% Efficient Si Solar Cells", 23rd IEEE Photovoltaic Specialist Conference, Louisville, KY., May 1993.

[5] Unisearch Limited (Kensington, NSW, Australia) price sheet distributed at the 23rd IEEE Photovoltaic Specialist Conference, May 1993, Louisville Ky. and R. M. Swanson, SunPower Corp, Sunnyvale CA, personal communication May 1993.

[6] Martin. A. Green and Keith Emery, "Solar Cell Efficiency Tables, (Version 2)", Progress in Photovoltaics: Research and Applications Vol I, 225-227, 1993.

[7] R. A. Sinton and R. M. Swanson, "Simplified Backside-Contact Solar Cells", Trans. Elec. Dev., **Vol. 37, No. 2**, February 1990.

[8] Green, M. A., *High Efficiency Silicon Solar Cells,* Trans Tech Publications, Switzerland,1987.

[9] P. J. Verlinden, R. M. Swanson, R. A. Sinton, R. A. Crane, C. Tilford, J. Perkins, and K. Garrison, "High-Efficiency, Point-Contact Silicon Solar Cells for Fresnel Lens Concentrator Modules", 23rd IEEE Photovoltaic Specialist Conference, Louisville, KY., May 1993.

[10] M. A. Green, J. Zhao, A. Wang, X. Dai, A. Milne, S. Cai, A. Aberle, S. R. Wenham, "Silicon Concentrator Solar Cell Research", Contractor Report # Sand93-7049, Sandia National Laboratories, June 1993.

[11] M. A. Green, J. Zhao, A. Wang, A. W. Blakers, W. Dai, C. M. Chong, S. R. Wenham, F. Zhang, F. Yun, J. Zolper, S. Narayanan, A. B. Sproul "One Sun Silicon Cell Research", Contractor Report # Sand93-7037, Sandia National Laboratories, March 1991.

[12] R. Schindler, I Reis, B. Wagner, A. Eyer, H. Lautenschlager, C. Schetter, W. Warta, "Rapid Optical Thermal Processing of Silicon Solar Cells", 23rd IEEE Photovoltaic Specialist Conference, Louisville, KY., May 1993.

Figure captions:

Fig. 1. Experimental results for silicon solar cells in the context of efficiency limits. The range 21-30% is shown expanded on the right.

Fig. 2. A comparison of cross sections of high efficiency cells. On the top is the PERL cell from UNSW[3,6,11], On the bottom is a backside-contact cell from Stanford University[7].

Fig. 3. The modeled efficiency of optimized backside-contact cells vs. substrate lifetime. These cells utilize a nominally undoped substrate operating under high-level-injection conditions. Other parameters based upon demonstrated devices.

Fig. 4. The spectral response measurements for a 35 cm^2 21.3% efficient backside contact solar cell.

Fig. 5 The degradation in power output for cells with 4 different high-quality passivations as a function of days under 500X sunlight in a Fresnel module. The control cell was not exposed. Some noise in the data is due to lens cleanliness and variations in the spectral content of the sunlight.

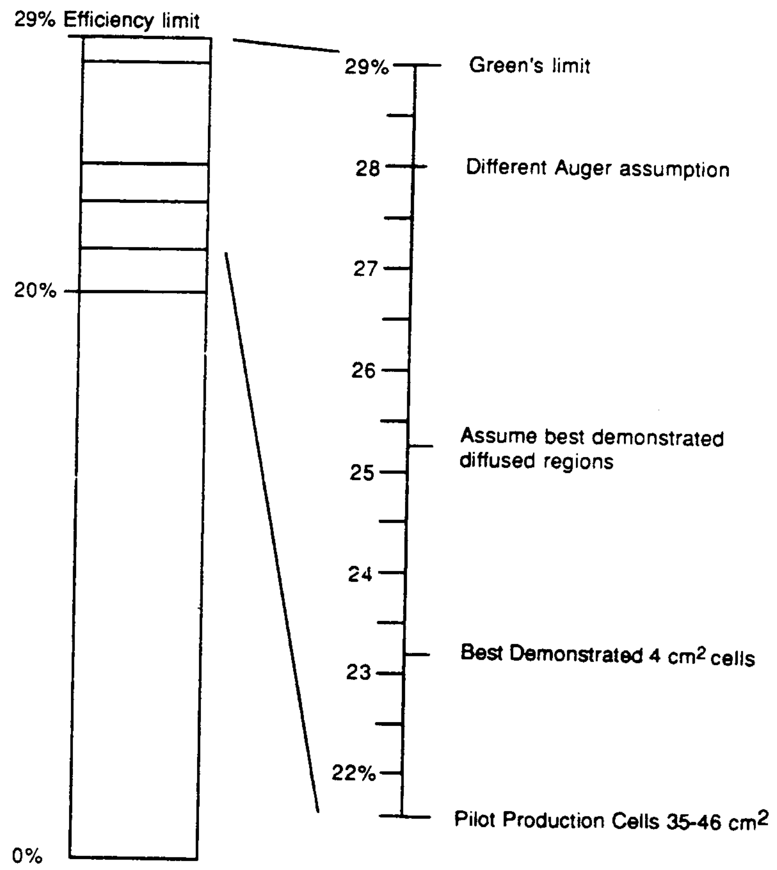
One-sun Cells
29% Efficiency limit
20%
0%
29%
28
27
26
25
24
23
22%
Green's limit
Different Auger assumption
Assume best demonstrated
diffused regions
Best Demonstrated 4 cm2 cells
Pilot Production Cells 35-46 cm2

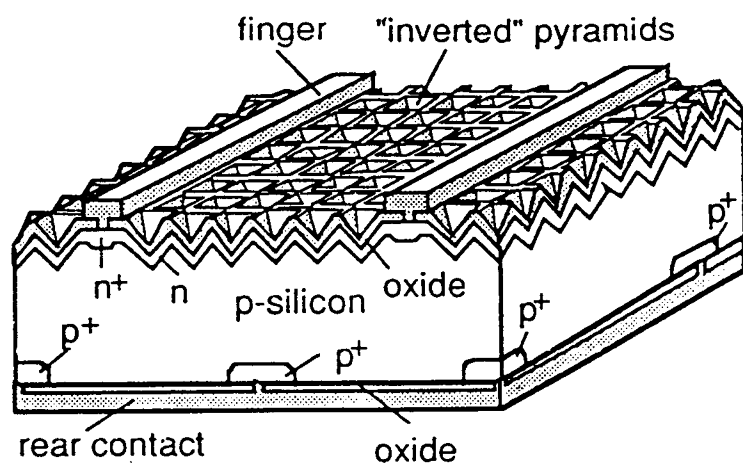
finger
"inverted" pyramids
n^+
n
p-silicon
oxide
p^+
p^+
p^+
p^+
rear contact
oxide

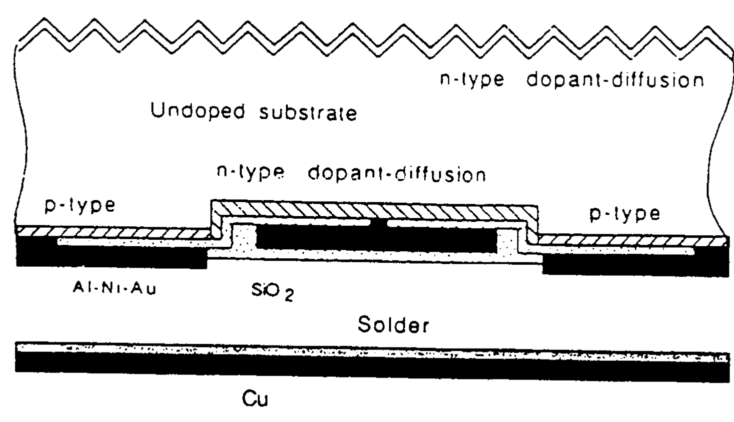
n-type dopant-diffusion
Undoped substrate
n-type dopant-diffusion
p-type
p-type
Al-Ni-Au
SiO_2
Solder
Cu

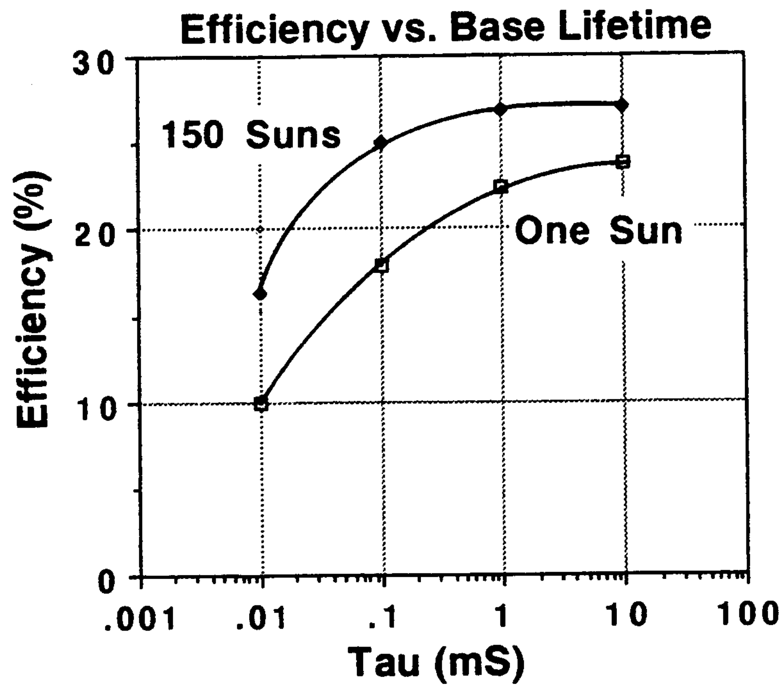
Efficiency vs. Base Lifetime
30
20
10
0
Efficiency (%)
150 Suns
One Sun
.001
.01
.1
1
10
100
Tau (mS)

Optical/Spectral Response Measurements*

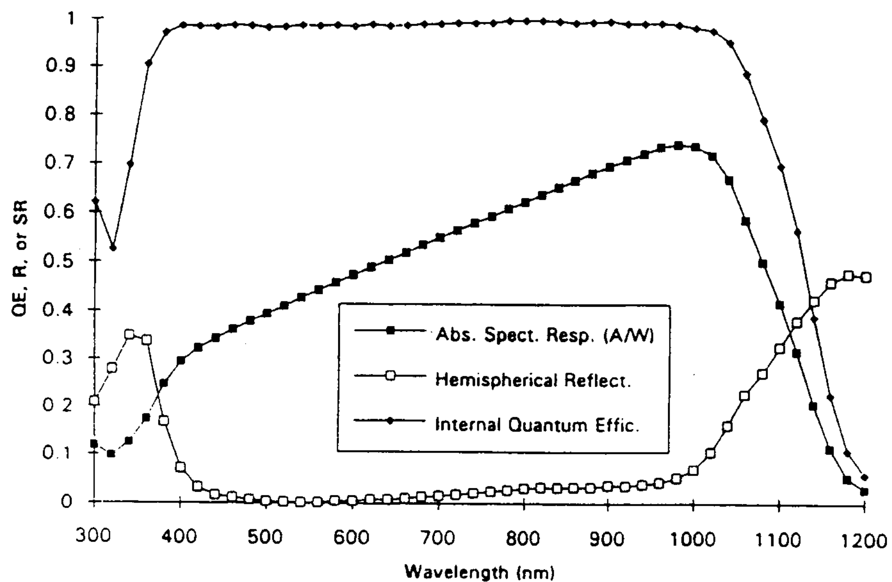

*James Gee, Sandia National Laboratories, Sept. 1992.

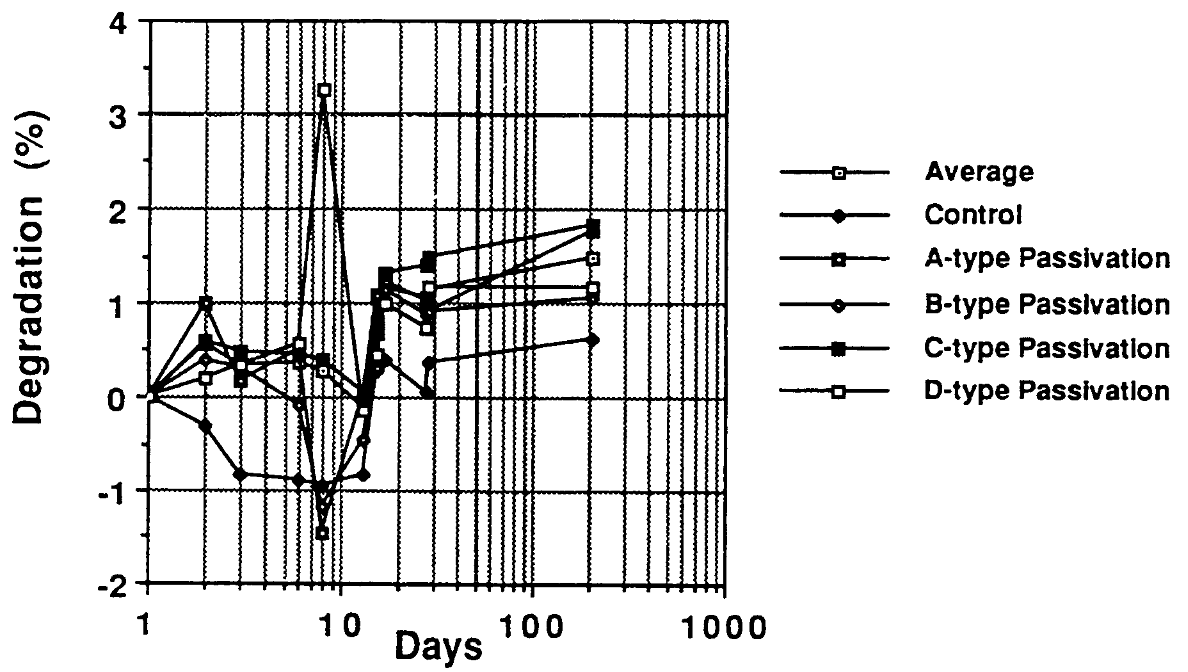

4
3
2
1
0
-1
-2
Degradation (%)
1
10
100
1000
Days
Average
Control
A-type Passivation
B-type Passivation
C-type Passivation
D-type Passivation

REPORT DOCUMENTATION PAGE

Form Approved
OMB NO. 0704-0188

Public reporting burden for this collection of information is estimated to average 1 hour per response, including the time for reviewing instructions, searching existing data sources, gathering and maintaining the data needed, and completing and reviewing the collection of information. Send comments regarding this burden estimate or any other aspect of this collection of information, including suggestions for reducing this burden, to Washington Headquarters Services, Directorate for Information Operations and Reports, 1215 Jefferson Davis Highway, Suite 1204, Arlington, VA 22202-4302, and to the Office of Management and Budget, Paperwork Reduction Project (0704-0188), Washington, DC 20503.

1. AGENCY USE ONLY (Leave blank)	2. REPORT DATE	3. REPORT TYPE AND DATES COVERED
	August 1994	Workshop Summary Report, August 16-18, 1993

4. TITLE AND SUBTITLE

The Role of Point Defects and Defect Complexes in Silicon Device Processing

5. FUNDING NUMBERS

C:

TA: PV421101

6. AUTHOR(S)

B. Sopori, T. Tan

7. PERFORMING ORGANIZATION NAME(S) AND ADDRESS(ES)

8. PERFORMING ORGANIZATION REPORT NUMBER

9. SPONSORING/MONITORING AGENCY NAME(S) AND ADDRESS(ES)

National Renewable Energy Laboratory
1617 Cole Blvd.
Golden, CO 80401-3393

10. SPONSORING/MONITORING AGENCY REPORT NUMBER

TP-413-7061

DE94011873

11 SUPPLEMENTARY NOTES

NREL Technical Monitor: B. Sopori

12a. DISTRIBUTION/AVAILABILITY STATEMENT

12b. DISTRIBUTION CODE

UC-1263

13. ABSTRACT *(Maximum 200 words)*

This report is the summary of the third workshop on the role of point defects and defect complexes in silicon device processing. The workshop was organized: (1) to discuss recent progress in the material quality produced by photovoltaic Si manufacturers, (2) to foster the understanding of point defect issues in Si device processing, (3) to review the effects of inhomogeneities on large-area solar cell performance, (4) to discuss how to improve Si solar cell processing, and (5) to develop a new understanding of gettering, defect passivation, and defect annihilation.

14. SUBJECT TERMS

silicon ; devices ; processing ; defects ; photovoltaics ; solar cells

15. NUMBER OF PAGES
122

16. PRICE CODE
A06

17. SECURITY CLASSIFICATION OF REPORT	18. SECURITY CLASSIFICATION OF THIS PAGE	19. SECURITY CLASSIFICATION OF ABSTRACT	20. LIMITATION OF ABSTRACT
Unclassified	Unclassified	Unclassified	UL